UNIVERSITY OF OKLAHOMA

GRADUATE COLLEGE

OSTEOCHONDRAL TISSUE ENGINEERING FOR THE

TEMPOROMANDIBULAR JOINT MANDIBULAR CONDYLE

A DISSERTATION

SUBMITTED TO THE GRADUATE FACULTY

in partial fulfillment of the requirements for the

Degree of

DOCTOR OF PHILOSOPHY

By

DAVID S. NEDRELOW
Norman, Oklahoma
2024

OSTEOCHONDRAL TISSUE ENGINEERING FOR THE
TEMPOROMANDIBULAR JOINT MANDIBULAR CONDYLE

A DISSERTATION APPROVED FOR THE
STEPHENSON SCHOOL OF BIOMEDICAL ENGINEERING

BY THE COMMITTEE CONSISTING OF

Dr. Michael Detamore, Chair

Dr. Valerie Watts

Dr. Javier Jo

Dr. Yingtao Liu

Dr. Fabio Ritto

Acknowledgments

Table of Contents

List of Figures

List of Tables

Abstract

An important goal for tissue engineering and regenerative medicine remains to to direct tissues regeneration with implantable scaffolds. Temporomandibular joint (TMJ) mandibular condyle tissue regeneration may require large scale scaffolds due to dramatic tissue loss. Unfortunately, there is a paucity of research on large-scale anatomically shaped scaffolds for osteochondral tissue regeneration. In the current dissertation, a human sized goat TMJ mandibular condylar prosthesis was developed with different phases for cartilage and bone regeneration. To regenerate cartilage, an acellular hydrogel was comprised of a light-cured pentenoate-modified hyaluronan (PHA) and devitalized cartilage matrix (DVC) based hydrogel. The hydrogel exhibited signs of potential chondrogenicity with upregulation of cartilage-specific genes (i.e., aggrecan and SOX-9) during *in vitro* cell culture with human bone marrow mesenchymal stem cells. An Ogden model was employed to improve the stiffness characterization of the cartilage-matrix hydrogel. In contrast with linear mechanical data, the hydrogel stiffness behavior was nonlinear. The nonlinear Ogden model fit exhibited a good fit of the nonlinear cartilage-matrix hydrogel mechanical data to failure (R^2=0.998 ± 0.001). For the bone substrate, we developed an in-house custom filament for use with commercially available 3D-printers. A goat-sized anatomically shaped 3D-printed osteochondral scaffold was digitally designed, fabricated, and implanted for 6 months in a small animal TMJ study. The study demonstrated that cartilage-like structures could be regenerated on the condyle surface and that bone formation was possible, though precise spatial control of bone formation remains an important challenge for further investigation. In addition, the integration of a hydrogel

chondral phase with a stiff osteal phase presented a challenging. The current thesis thus aimed to enhance furthermore aimed to develop a biomechanically interlocking structure to enhance the interface strength, and furthermore enhance the bioactive properties of 3D-printed PCL-based bone scaffolds. For the biomechanically interlocking interface structure, an hourglass tube shape was introduced. Interface biomechanics of the hourglass tube structure were investigated with both empirical experiments, and a computer model that simulated the experiment conditions. The hourglass tube computer model exhibited a shift in stress favoring compressive stresses. Empirically, the hourglass tube exhibited 54% higher ultimate interface shear stress, 49% higher nominal strain at failure, and 2.15-fold higher energy to failure than the crosshatch substrate's 33 kPa, 19%, and 3.9 kJ $\cdot$ m^3, respectively. To promote controlled bone growth, a series of potentially osteoinductive biomaterials, i.e., demineralized bone matrix (DBM), and devitalized tendon (DVT) were successfully incorporated into a PCL-based 3D-printing filament at concentrations of up to 50% w/w and 3D-printed to form scaffolds. 3D-printed PCL functionalized with 37.5% w/w HAp and 12.5% w/w DBM exhibited enhanced osteogenic gene expression for RUNX2 and OCN. Overall, the current dissertation demonstrated signs of functional TMJ restoration with an acellular prosthesis; therefore, the significance of the current dissertation was the development of a functional biomaterial scaffold that was 3D-printable and translatable to temporomandibular joint restoration.

Chapter 1: Introduction

1.1 The Temporomandibular Joint Mandibular Condyle's role in Temporomandibular Pain and Osteoarthritis

Temporomandibular joint (TMJ) pain is the most common cause of nondental orofacial pain [1]. TMJ pain can intensely impact common, daily activities such as eating, speaking, or laughing, particularly for young, pre-menopausal women [2], [3]. Even with high quality treatment, TMJ disorder symptoms can progress to chronic centralized pain in 15% of cases, making TMJ disorders the second most common musculoskeletal pain condition [4], [5]. Osteoarthritis can lead to severe cartilage degradation of the TMJ mandibular condyle that extends deep into subchondral bone [6]. Trauma can additionally damage the articulating surface of the condyle [7]. Condylar hyperplasia can cause joint impingement due to alterations in the condyle's anatomic shape [8].

1.2 Temporomandibular Joint Anatomy, Structure, and Function

The TMJ is a ginglymoarthrodial joint formed by the glenoid fossa of the temporal bone and the mandibular condyle [9], with an articular disc that is positioned between the mandibular condyle and glenoid fossa. The disc separates the joint into two synovial cavities, and supports translational movement primarily in the anteroposterior direction [10], [11], [12]. Although the mandibular condyle's microstructure is analogous to the knee in that it is layered and comprised of subchondral bone and cartilage, there are distinguishing characteristics [13]. For example, through immunostaining for collagen

types I and II, it can clearly be shown that mandibular condylar cartilage has more collagen I than hyalin cartilage [13], [14]. TMJ mandibular cartilage is comprised of four histological zones demarcate the structure of mandibular condylar cartilage across its 0.4-0.5 mm thickness: (1) The most superficial *fibrous zone* consists primarily of collagen I sheets arranged parallel to the surface. Additionally, there are (2) *proliferative* and (3) *mature zones* where most of the mandibular condylar cartilage's mesenchymal cells and chondrocyte precursors can be found. (4) The deep *hypertrophic zone*, in contrast with the zones above, is largely composed of chondrocytes and collagen type II, the latter of which can additionally be found in the mature zone [15]. Two TMJs function together in mastication along with contacting teeth in the maxilla and mandible. All functions related to jaw movement are mediated by the TMJ making it centrally important to daily activities such as speaking and eating.

1.3 Prior Temporomandibular Joint Regenerative Scaffolds and Their Limitations

Tissue engineering may provide patients with an alternative to metal-based implants for several conditions such as condylar trauma [16], [17], TMJ pathologies in skeletally immature patients [18], [19], hyperplasia [20], or metal hypersensitivities [7], [21], [22]. Research efforts to develop a regenerative scaffold for the TMJ mandibular condyle can be organized into two main categories: (1) Acellular scaffolds that induce a favorable host response to regenerate tissue using bioactive signals embedded in the material, and (2) cellular scaffolds comprised of living cells cultured *in vitro* prior to implantation in the patient. Although a recent example of a cellular TMJ mandibular

condylar scaffold demonstrated key evidence of organized osteochondral tissue regeneration on the microscale [23], cellular scaffolds are currently burdened with translational challenges such as additional fabrication time. Acellular TMJ scaffolds offer an attractive strategy from a translational standpoint [24], [25], [26], [27], [28] [29], [30], but are currently limited by the quality of osteochondral tissue regeneration. Furthermore, examples of both acellular and cellular TMJ scaffolds have successfully grown bone tissue; however, neither have achieved the desired shape and location of the new bone [23], [30].

The objectives of my thesis were, firstly, to fabricate an acellular scaffold to induce osteochondral tissue regeneration, secondly, to characterize the scaffold biomaterials with both *in vitro* and *in vivo* experiments and determine their utility as an implantable scaffold for TMJ mandibular condyle regeneration, and thirdly, to design an interlocking geometry that enhances the interface strength of the osteochondral scaffold. Finally, additional functionalization of 3D-printed scaffolds was investigated that aimed to enhance bone regeneration.

1.4 Specific Aims

The following research aims were designed to advance tissue engineering for an acellular TMJ mandibular condylar scaffold:

- **Aim 1**: Develop a novel cartilage-matrix based hydrogel, characterize its nonlinear mechanical performance, and evaluate its chondrogenic potential.

- **Aim 2**: Evaluate a biphasic mandibular condyle prosthesis in vivo with a goat temporomandibular joint mandibular condyle model.

- **Aim 3**: Generate an interlocking microarchitecture to enhance interface strength of osteochondral scaffolds. Further evaluate interlocking feature for stiffness and porosity as an anisotropic scaffold architecture.

- **Aim 4:** Fabricate a 3D-printed polycaprolactone-demineralized bone matrix composite scaffold to support osteogenesis.

The research completed has resulted in five studies that are organized as chapters in my thesis.

3D-Printing the Osteochondral Interface: Recent Advances and Design Considerations (Chapter 2)

Chapter 2 provides a background review**.** A critical review of the literature was performed to organize potential strategies for anatomically accurate 3D-printed osteochondral scaffolds with a strengthened interface. The reviewed studies presented in this chapter are focused on enhancing interface shear performance in osteochondral scaffolds. Additionally, studies were selected that leveraged 3D-printing to fabricate anatomically accurate scaffolds for osteochondral regeneration. Testing methodologies were studied to determine a suitable interface shear test that could offer reproducible results.

The Ogden model for hydrogels in tissue engineering: Modulus determination with compression to failure (Chapter 3) [31]

Chapter 3 addresses **aim 1**. The characterization of nonlinear mechanics in tissue engineered hydrogels depends largely on the model selected, particularly when the hydrogels can support large strains. However, previous studies that characterized tissue engineering hydrogels often utilized a linear compressive elastic modulus model with a user-selected strain range. The first chapter of my thesis characterizes a composite

cartilage-matrix hydrogel for chondroinductivity and applies an Ogden model fit to the nonlinear stress/strain behavior of the hydrogel under compression.

Regenerative Engineering of a Biphasic Patient-Fitted Temporomandibular Joint Condylar Prosthesis (Chapter 4) [32]

Chapter 4 addresses **aim 2.** Having determined that the cartilage-matrix hydrogel's mechanics and *in vitro* characterization of chondroinductivity could potentially support chondrogenesis *in vivo*, the cartilage matrix hydrogel was infilled into a patient-fitted 3D-printed TMJ condylar scaffold. The biphasic scaffold exhibited an osteal phase comprised of polycaprolactone and 20% w/v hydroxyapatite 3D-printed from custom filament made in-house. To characterize both the chondroinductive and osteoinductive potential of the biomaterials, the biphasic condylar scaffold was implanted in a human sized TMJ condyle defect in six goats for six months. Then, the tissues were resected and analyzed with microCT and immunohistochemistry to characterize potential osteochondral tissue regeneration in the scaffold.

Interface Performance Enhancement in 3D-Printed Biphasic Scaffolds with Interlocking Hourglass Geometry (Chapter 5)

Chapter 5 addresses **aim 3**. Chapter 2 concluded with the idea that an interlocking geometry was a promising approach for enhancing the mechanical performance of biphasic scaffolds. It was not clear, however, what design parameters could be used to explore the effects on interface strength. A fully parameterized hourglass interface design was thus developed and evaluated *in silico* with a computational model. The simulation applied a shear load to a hydrogel that infilled the hourglass feature consistent with a previously reported interface shear test [33]. The hourglass feature was additionally used to design an infill architecture for the scaffolds and evaluated for compressive behavior.

3D-Printed Polycaprolactone Scaffolds Functionalized with Multimaterial

Hydroxyapatite, Devitalized Tendon, or Demineralized Bone Matrix (Chapter 6)

Chapter 6 addresses **aim 4**. Stimulation of stable bone growth with a tissue engineered scaffold is central to successfully restoring the TMJ mandibular condyle. In this chapter, we develop a 3D-printed polycaprolactone (PCL) functionalized with high concentrations of potentially bioactive components, (1) hydroxyapatite (HAp), and (2) demineralized bone matrix (DBM) to induce bone formation. Controlling the ratios of each component in a multimaterial PCL-HAp-DBM scaffold allows us to explore formulae that stimulate a favorable response from human bone marrow mesenchymal stem cells (hBMSCs). Osteogenic expression from the cells *in vitro* suggests that the scaffold material is a candidate for further characterization *in vivo*. Furthermore, the mechanical properties and 3D-printability are additionally important to the successful translation of the scaffold to *in vivo* studies. The results presented here are focused on the *in vitro* fabrication methods of 3D-printed PCL-based composites, and the osteogenic effects from different ratios of HAp and DBM in the 3D-printed PCL. Further work is still needed to characterize the PCL-HAp-DBM scaffold's degradation properties to ensure continued function in the joint. However, the research presented in this thesis provides a solid foundation for further *in vivo* characterization.

Chapter 7 is the conclusion to the dissertation, where the major findings of all four aims, limitations of the studies, and recommendations for future research are discussed.

Chapter 2: 3D-Printing the Osteochondral Interface: Recent Advances and Design Considerations[1]

2.1 Abstract

There is a clinical need for osteochondral scaffolds with complex geometries for restoring articulating joint surfaces. To address that need, 3D-printing has enabled scaffolds to be created with anatomically shaped geometries and interconnected internal architectures, going beyond simple plug-shaped scaffolds that are limited to small, cylindrical, focal defects. A key challenge for restoring articulating joint surfaces with 3D-printed constructs is the mechanical loading environment, particularly to withstand delamination or mechanical failure. Although the mechanical performance of interfacial scaffolds is essential, interface strength testing has rarely been emphasized in prior studies with stratified scaffolds. In the pioneering studies where interface strength was assessed, varying methods were employed, which has made direct comparisons difficult. Therefore, the current review focused on 3D-printed scaffolds for osteochondral applications with an emphasis on interface integration and biomechanical evaluation. This 3D-printing focus included both multiphasic cylindrical scaffolds and anatomically shaped scaffolds. Combinations of different 3D-printing methods (e.g., fused deposition modeling, stereolithography, bioprinting with pneumatic extrusion of cell-laden hydrogels) have been employed in a handful of studies to integrate osteo- and chondro-inductive regions into a single scaffold.

---

[1]Submitted to: *Journal of Biomedical Materials Research Part A*

Most 3D-printed multiphasic structures utilized either an interdigitating or a mechanical interlocking design to strengthen the construct interface and to prevent delamination during function. The most effective approach to combine phases may be to infill a robust 3D-printed osteal polymer with an interlocking chondral phase hydrogel. Mechanical interlocking is therefore recommended for scaling up multiphasic scaffold applications to larger anatomically shaped joint surface regeneration. For evaluation of layer integration, the interface shear test is recommended to avoid artifacts or variability that may be associated with alternative approaches that require adhesives or mechanical grips. The 3D printing literature with interfacial scaffolds provides a compelling foundation for continued work toward successful regeneration of injured or diseased osteochondral tissues in load-bearing joints such as the knee, hip, or temporomandibular joint.

2.2 Introduction

Osteoarthritis affects approximately 10.5% of the US population, with large aggregate medical costs reaching up to $460 billion [34]. Treatment options for osteoarthritis span a range that includes palliative maintenance, articular injections (e.g., corticosteroids, viscosupplements), surgical grafting and total joint replacement [35]. Surgical interventions include autografts derived from the patient, allografts from cadaveric sources, or biomaterials that provide a regenerative scaffold to promote healing in the defect site. Due to shifting population demographics, the number of people who rely on implantable biomaterials comprised of metal or polymer composites for total joint replacement is expected to increase by up to 85% from the year 2018 to 2030 [36], [37]. To meet upcoming clinical demands, 3D-printed tissue engineered scaffolds are being

developed to regenerate osteochondral tissues with translational potential for total joint replacement [23], [38], [39].

Osteochondral tissues present a tissue engineering challenge due to two different tissue layers that must be regenerated as an integrated osteochondral unit [40]. Cartilage and subchondral bone tissues have vastly different architectural, chemical, and mechanical properties [41]. For example, articular cartilage is avascular, whereas bone has an extensive vascular network to provide nourishment. Multiphasic osteochondral scaffolds comprised of regions with specialized structures have been designed with the goal to induce region-specific osteal or chondral tissue regeneration [40], [42], [43]. Osteochondral tissues present an additional design challenge to prevent interface delamination, i.e., the scaffold must integrate the different tissue layers such that the layers remain intact post-implantation. Dormer *et al.*[38] provided context on the progression of interfacial tissue engineering from biphasic, triphasic, and multiphasic scaffolds to a continuous gradient interface structure, thereby emphasizing a complex structure for the interface itself. However, 3D-printing of gradient structures is generally limited to one single 3D-printing method, e.g., from one polymer to another by melt-based extrusion [44], or from one hydrogel to another by syringe-based extrusion [45], [46]. For osteochondral applications that rely on different 3D printing methods such as melt-based extrusion of a polyester for the bone region and syringe-based extrusion for a hydrogel for the cartilage region, multiphasic scaffolds will be more relevant than true gradient approaches.

Owing to 3D-printing's unique capabilities for creating spatially complex architectures, 3D-printing offers outstanding translational potential for creating osteochondral scaffolds. 3D-printing provides an efficient alternative treatment for

9

osteochondral defects with integrated, anatomically-shaped 3D-printed scaffolds, representing a major logistical advantage over cell-based therapies, which may require weeks of preparation [47], [48]. Research interest in 3D-printed osteochondral scaffolds has recently boomed from fewer than 5 citations in 2010 to over 1,800 citations in 2022 according to a recent review from Ege and Hasirci [49]. At least nine clinical trials or randomized controlled trials to date have been published that employed 3D-printing for osteochondral tissue engineering [50]. 3D-printed implants with complex porous architectures and integrated solid components such as an acetabular shell with a porous coating or lattice structures for spinal cages have been approved by the FDA for clinical use [51], [52].

3D-printed materials are assembled layer-by-layer with high dimensional control over geometric architecture, porosity, and choice of biomaterial deposited. 3D-printing is thus well suited for fabricating stratified structures such as osteochondral tissue [53]. There are various methods of 3D-printing available for translational use, each designed with a layer-by-layer additive manufacturing strategy [47], [54], [55], [56], [57], [58]. Extrusion-based fused deposition modeling (FDM) 3D-printers have widespread use for hobbyist, commercial, and biomedical applications [58], [59], [60], [61]. Other examples of 3D-printing methods include stereolithography and bioprinting with a pneumatic extrusion head. Biodegradable polymers are common to 3D-printing, although composites, ceramics, or even metals have additionally been 3D-printed with extrusion-based systems [62]. Additionally, synthetic polymers have incorporated bioactive signals for controlled release to direct cell fate for regional cartilage or bone regeneration [63], [64], [65], [66], [67]. For example, a poly(propylene fumarate)-based 3D-printing filament incorporated a bioactive

10

recombinant bone morphogenetic protein (BMP)-2 growth factor [68]. Although 3D-printing resolutions vary with different techniques, some articles have suggested that cell-laden materials have inherently higher resolutions than non-cellular extruded materials due to the cell membrane's mechanical limitations to shear stresses generated during the bioprinting process [47], [55].

Enhancing the biomechanical performance of the osteochondral scaffold interface is a growing area of interest for 3D-printing [69]. The interface between the chondral and osteal phases is inherently prone to stress concentrations, which may result in mechanical failure [41], [53], [70], [71], [72], [73], [74], [75]. As a valuable resource for lessons gleaned for application in 3D printing, there are multiple examples of non-3D-printed interface reinforcement strategies, which are outlined in **Table 1** [24], [76], [77], [78], [79], [80], [81], [82], [83]. Briefly, there are four primary different integration strategies: (1) Chemical bonding, where two different types of materials are chemically bonded to each other, often through specific linkage chemistry [84], [85], [86]. (2) Solvent bonding, where each dissolved polymer entangles with the other in a liquid solvent phase, and then the solvent is vaporized, leaving a solid interface layer where the two polymers exhibit molecular entanglement with each other [87]. (3) Tissue culture with cells seeded to allow matrix ingrowth across the materials [88], [89], [90], [91], [92], [93], [94], [95]. (4) Mechanical interlocking such that internal architectures of each material are designed to have interlocking geometries [96], [97]. Although previous reviews have emphasized the importance of the interface for osteochondral scaffolds, few reviews have specifically focused on 3D-printed multiphasic scaffolds with robust interface integration [69].

The current review therefore provides an overview of advances to multiphasic osteochondral scaffolds brought about by 3D-printing technology with an emphasis on the interface. Previous studies and reviews have provided backgrounds on the topics of multiphasic scaffolds, interfacial 3D-printing, or anatomically shaped 3D-printing [41], [63], [65], [67], [71], [72], [98], [99], [100]. However, a review that encompasses all three of these topics has not been published in the literature. To fill this gap, the current review includes coverage of all three topics (**Fig. 1**) [41], [63], [65], [67], [71], [72], [98], [99], [100].

The interface region of multiphasic scaffolds presents a major challenge with mechanical failure when implanted in load-bearing locations [49], [51], [69], [101], [102], [103]. Choe *et al.*[69] in particular provided a valuable review of biomechanical aspects of interfacial osteochondral scaffolds fabricated by 3D-printing. Although that review provided valuable insights regarding interfacial tissue engineering and 3D-printing, the methods employed for interface testing methodologies were not emphasized. The current review therefore will provide a summary of studies that performed quantitative characterizations of 3D-printed osteochondral interface integration. For context to aid in the interpretation of those quantitative analyses, a brief overview of general mechanical tests that exist for interface evaluation will be provided in the current review.

The following section of the current review emphasizes the interface of 3D-printed osteochondral scaffolds. Examples of interface integration are provided in addition to quantitative characterizations of interface strength. The next section of the current review describes 3D-printed osteochondral scaffolds with an anatomically accurate shape.

2.3 Interface Integration in 3D-Printed Osteochondral Scaffolds

In this section, we review how mechanical interlocking geometries have been employed to enhance interface integration in 3D-printed osteochondral scaffolds. Furthermore, we critically evaluate how interface biomechanical properties have been quantified (**Table 2**). 3D-printed osteochondral constructs comprised of more than one phase require integration between phases to maintain function in the joint environment. In a previous review, interface adhesion mechanisms for multiphasic osteochondral constructs were described (e.g., chemical bonding, acid-base, or weak boundary layer) [69]. To improve adhesion mechanisms, that review suggested increasing the interface contact surface area by leveraging complex 3D-printed geometries. Therefore, 3D printing strategies that incorporate interdigitation or other interlocking geometries to increase the surface area at the interface may enhance mechanical integration between phases [53], [63], [65], [69], [71], [104], [105], [106]. Another review described the biomechanical behavior of 3D-printed interfaces [42], where unfortunately, as noted by the authors, testing methodologies have varied across studies, making it difficult to make direct comparisons.

Based on the literature to date, there are specific interface shear testing methods available for evaluating interface strength (**Fig. 2**) [33], [74], [107], [108], [109]. The interface shear test, for example, applies a force to the side of the chondral phase with a platen, while the osteal phase remains fixed in position. In contrast, the single lap test does not apply a force to the side, but instead relies on adhering tabs to the opposing surfaces and then pulling those tabs in opposite directions. In contrast with an interface shear test, the lap test requires the sample to be gripped or glued, which may introduce artifacts in the results. Another option that does not include a force to the side or surface adhesion is the peel test, which grips the edge of the chondral phase and applies a force in the direction

normal to the anchored osteal phase. Generally, we recommend the interface shear test to reduce variability or artifacts potentially caused by glues, and as a more physiologically relevant test than the peel test. Glues are employed in the single lap test to attach samples to loading grips, and which may alter the specimen's material properties.

Interface shear test results may differ based on whether a surface-constraining platen is present or not, as a constraining platen may increase the apparent interface performance. For example, the interface fracture toughness in one study was 1 to 4 times higher with the constrained upper surface[74] compared to another study that employed an interface shear test without a constraining platen [75].

3D-printing provides control over internal architectures. That control enables mechanical integration of the chondral and osteal phases in a unified scaffold. This integration may enhance interface strength, thereby overcoming a major biomechanical challenge [69]. For example, an interlocking "lock-key" interface feature that spanned a scaffold's two structural phases was explored to enhance strength and prevent delamination [73], [110]. The two phases, both comprised of polylactic acid (PLA), were defined by different architectures. Specifically, for the 'cartilage' phase, a crosshatch pattern was employed. For the 'bone' phase, a ring pattern was utilized [110]. To evaluate shear strength between these two layers, a biomechanical interface shear test was performed. This interface shear test employed a wedge that was placed along the interface line of the scaffolds (**Fig. 2**). The shear strength with interlocking was 1.8 times higher than the shear strength of scaffolds without the 3D-printed interlocking feature. In contrast to that example, where both phases were comprised of PLA, another approach examined the

interface strength between a hydrogel and a much stiffer substrate, with a common theme of enhancing interface strength with a 3D-printed interlocking structure [69].

Specifically, Zhang *et al.*[33] 3D-printed an interlocking osteochondral scaffold comprised of a polyethylene glycol (PEG) hydrogel cured layer-by-layer within a β-tricalcium phosphate (β-TCP) substrate. The pore area percentage at the interface was controlled by spacing out 0.4 mm-diameter pores at specified lengths, which resulted in pore void-space areas ranging from 0% (i.e., no pores) to 60%. To evaluate integration, a modified interface shear test (**Fig. 2A**) was employed with a platen that applied a shear load by pressing against the side of the hydrogel, with an L-shaped extension that rested on the top surface as a constraining platen. The interdigitating interface enhanced the shear strength nearly 3-fold compared to a non-porous surface. The interface shear strength reached that maximum when the pore percentage areas were at 30%. However, above 30%, the strength did not change with higher pore area percentages up to 60%. The high interface strength (i.e., 340 kPa) obtained with a combination of hydrogel and ceramic materials with disparate properties suggested that mechanical interlocking has the potential to enhance the strength of 3D-printed osteochondral scaffolds under joint loading.

In another example of an interface-enhancing architecture, a crosshatch pattern was constructed with three distinct interface patterns, each with different strut spacings. In contrast with the aforementioned study where the pore spacing affected interface strength, the crosshatch patterns exhibited negligible differences in interface shear strength compared to a control group with a smooth surface [107]. Investigation of the print pattern was limited to a crosshatch design with alternating 0˚ and 90˚ strut orientations. The crosshatch interface designs were limited to a sub-mm scale that was one printed layer in

height. Interlocking geometries with a pore area percentage over 30% demonstrated enhanced interface shear strength compared to a smooth surface. A larger interface feature greater than one printed layer may warrant further investigation. To enhance interface strength, interlocking geometries may require additional complexity to fully utilize 3D-printing for enhanced multiphasic scaffold interface integration [33], [73], [89], [107], [108], [110].

In a unique scaffold fabrication approach from Brown *et al.*[89], neocartilage made from juvenile ovine articular chondrocytes and cultured in a 3D-printed mold was prefabricated and then further cultured on a porous hydroxyapatite substrate. The ultimate shear strength was measured using a lap test (**Fig. 2B**). Constructs with an interdigitation depth of nearly 100 μm and a higher frequency of 4 mm^{-1} exhibited a 4.9-fold enhanced ultimate shear strength of 83 kPa compared to the other group with the lower interdigitation depth and frequency. The study further evaluated the neocartilage surface after delamination, finding that the group with greater interdigitation depth and frequency exhibited an adhered hydroxyapatite coverage area on the delaminated neocartilage that was 2.4 times higher than the area of the group with less chondral interdigitation. The authors concluded that the increased chondral interdigitation with the osseous phase was the primary factor that caused the greater interface shear strength. Additionally, adhesion between the two phases was cited as a factor for interface shear strength. The study highlighted the potential value of increasing the interdigitation frequency and depth as a strategy to enhance the interface strength.

A recent study combined multiple 3D-printing methods to improve mechanical performance of the interface. In that study, a triphasic scaffold was constructed with a

polycaprolactone (PCL) microfiber mesh phase in between extrusion 3D-printed osteal and chondral phases [108]. The microfiber mesh was fabricated via melt electrowriting, and then a ceramic osteal phase was 3D-printed onto that microfiber mesh with a pneumatic extrusion-based printer. The resulting structure was then turned upside down so that the microfiber mesh was on top, and then a gelatin methacrylate (GelMA) hydrogel was infilled to the mesh, resulting in the triphasic scaffold with fiber mesh anchorages extending across both the osteal and chondral phases. To quantify interface strength, an interface shear test was performed without a constraining platen on the upper face. The resulting interface shear strength of 17.7 kPa was 6.5-fold higher than the shear strength of scaffolds without the anchoring microfiber mesh. Fabricating the fine microfiber mesh was made possible with a high-resolution melt electrowriting technique that may not be practical with other 3D-printing techniques. That study demonstrated the potential for 3D-printing to enhance interface strength with an interdigitating internal mesh architecture.

The potential benefits of 3D printing for enhancing mechanical integrity of the interface depend on the material properties of each layer. For example, biphasic scaffolds with a 3D-printed hydrogel on a 3D-printed PCL scaffold demonstrated a 40% increased interface shear strength with a stiffer hydrogel compared to a more compliant hydrogel [107]. These scaffolds were co-printed with a single printer and the hydrogel was photocrosslinked within a crosshatch architecture. In that case, the more compliant hydrogel was GelMA (elastic modulus of 3 kPa), and the stiffer hydrogel was polyethylene glycol diacrylate (PEGDA, 62 kPa). To better understand how the differences in stiffness between the two phases may affect the interface strength, those authors performed

computer simulations of interface shear tests. Both the simulation and empirical results emphasized value for high stiffness hydrogels in osteochondral tissue engineering.

Collectively, the studies presented above identified multiple 3D-printing strategies to enhance interface strength in multiphasic scaffold integration, including manipulating material properties and creating an interlocking microarchitecture. The evidence suggested that interlocking features enhanced interface shear strength with examples that exhibited from 3- to 6.5-fold enhanced strength [33], [89], [108]. In contrast, one of the above studies demonstrated that differences in a crosshatch interface microarchitecture had no effect on interface strength [107]. Additional depth, or geometric complexity, may enhance interface strength as demonstrated by some of these studies [33], [89], [108]. With regard to the effect of differing material properties of the two phases in an osteochondral scaffold, increasing the chondral phase stiffness such that it was within an order of magnitude of the osteal phase was suggested to enhance the interface strength. Although post-implantation maturation may improve the scaffold neocartilage stiffness [111], previous studies have suggested that further research is warranted to develop high stiffness chondral regions [107], [112]. Comparing the value of an interlocking design to those that emphasized material stiffness, evidence suggested greater gains may be available from the interlocking design.

2.4 Anatomically Shaped 3D-Printing of Osteochondral Scaffolds

Advances in 3D-printing technologies have made it feasible to rapidly produce complex, anatomically shaped scaffolds [50], [113]. However, there are relatively few studies that have explored 3D-printing to regenerate large-scale joint surfaces with scaffolds that are both 1) multiphasic and 2) anatomically shaped [113], [114], [115]. In this section, we provide an overview of studies that employed 3D-printing to create multiphasic, anatomically shaped, osteochondral constructs (**Table 3**). Anatomies that have been successfully 3D-printed as tissue engineering scaffolds include the proximal tibia, distal femur, ear auricle, knee meniscus, talus, aorta, and temporomandibular joint (TMJ) mandibular condyle [110], [116], [117], [118], [119], [120], [121], [122], [123], with selected examples provided below.

As an example of 3D-printing related to the TMJ, a mandibular condyle scaffold was 3D-printed for only the osteal phase via FDM, which was then press-fit together with a chondral phase [124]. The osteal phase, consisting of a composite with PCL and 40% hydroxyapatite (HAp), was seeded with minipig bone marrow-derived mesenchymal stem cells (BMSCs). The chondral phase was created by shaping a non-woven polyglycolic acid/polylactic acid (PGA/PLA) blend fiber mesh into a condylar surface. As an alternative to the PGA/PLA chondral phase, the same study employed a cell sheet as the chondral phase, created by culturing mini-pig BMSCs above confluency for 4 weeks. Instead of press-fitting to combine with the osteal phase, the cell sheet chondral phase was sutured onto the PCL-HAp condyle-shaped osteal phase. 12 weeks after subcutaneous implantation in athymic nude mice, both the cell sheet and the cell-seeded polymer biphasic condyles exhibited signs of cartilage tissue formation. Bone formation, however, was deficient. A key point of value of this study was in demonstrating methods to adhere two phases

19

together, i.e., a chondral phase on top of the complex geometry of the mandibular condyle, with those methods being a press fit (PGA/PLA blend fiber mesh) or suturing (cell sheet).

In a different TMJ study, which was performed by our group, a mandibular condyle prosthesis was 3D-printed with an FDM extrusion system [32], followed by addition of a hydrogel layer by hand via syringe. The 3D-printed PCL-HAp (20% w/w HAp) prosthesis incorporated a mechanical interlocking feature for enhanced hydrogel integration. The hydrogel was comprised of pentenoate-modified hyaluronic acid, devitalized cartilage, and PEG. The hydrogel precursor solution was syringed onto the PCL-HA condylar substrate's interlocking structure and photocrosslinked. The hydrogel exhibited signs of chondrogenicity *in vitro* [31]. An *in vivo* goat TMJ study was prepared by resecting the right mandibular condyle (left side remained intact), with the TMJ disc being preserved, and implanting the biphasic scaffold orthotopically in the goat. 6 months after implantation, there were signs of neocartilage formation; however, bone formation was not abundant within the PCL/HAp scaffold's ~150 μm pore-size microarchitecture.

In a study related to the distal femur, a multi-material scaffold was co-3D-printed with a multi-head extruder to create an anatomically shaped geometry [125]. PCL was co-printed with two different cell-laden alginates, one with chondrocytes in the region corresponding to the cartilage surface, and the other with osteoblasts throughout the remainder of the scaffold. The PCL geometry resembled the human distal femur and contained microchambers filled with the cell-laden alginates. Regarding the microchambers, some were left empty, while others were filled with chondroblast-laden or osteoblast-laden alginate. Pores were printed at specific sizes, which ranged from 50 to 600 μm. Cell viability within the scaffold persisted for up to 7 days. The study was limited to a

proof-of concept print and did not evaluate chondrogenesis or osteogenesis. Although the proof-of-concept femur-shaped scaffold was limited to 20 layers in height, the multi-head printing concept demonstrated potential for full-sized condylar multi-material scaffolds.

In a tibial plateau study, a human sized tibia-shaped scaffold (42 x 21 x 10 mm) was created and studied *in vitro*. The scaffold had spatially-organized tissues generated with FDM 3D-printed PCL microchambers, into which cell-laden GelMA hydrogels were later inkjet-printed and photocrosslinked [126]. The dimensions of each of the microchambers were approximately 0.8 x 1.2 mm. The different microchambers were filled with different cell types carried by the hydrogel precursor for region-specific tissue engineering. The cartilage region hydrogel had a 3:1 ratio of mesenchymal stem cells and chondrocytes, and the bone region hydrogel was comprised of MSCs only. The study focused on characterizing the cartilage-forming properties of the scaffold without closely examining the mineralizing properties of the scaffold for bone regeneration. A mesenchymal stem cell and chondrocyte-laden hydrogel exhibited signs of neocartilage formation in the surface microchambers after 10 weeks of *in vitro* culture under dynamic loading conditions. Sulfated glycosaminoglycans (sGAGs), collagen II, and lubricin were localized to the scaffold's surface microchambers, demonstrating the potential for region-specific regeneration in a tibial plateau-shaped scaffold.

Another study 3D-printed several anatomically shaped constructs (e.g., vascular tree, ear, and femoral condyle) for a future application of customizing implants for tissue regeneration [127]. Evaluations of advanced *in vitro* or *in vivo* outcomes and interface behavior were not performed. For these implants, the materials employed included polyvinyl alcohol (PVA), PCL, GelMA, and alginate. The vascular tree and ear constructs

were designed to regenerate only one type of material and were thus outside the scope of this review. The bone and cartilage regions of the femoral scaffold were co-printed with a multihead 3D-printer. The bone region was represented by a PCL material that was 3D printed via FDM. The cartilage region was simultaneously co-printed with a GelMA-gellan gum hydrogel that was pneumatically extruded into the PCL chambers and photocrosslinked. The shape of the 3D-printed scaffold resembled an anatomical human bone femur shape, with a hydrogel component on the surfaces that represented cartilage. This early proof-of-concept study evaluated printability of 3D-printing support materials such as PCL, PVA, and alginate. The study demonstrated a new methodology whereby complex 3-dimensional shapes were 3D-printed from multiple materials for potential use in joint tissue engineering.

In another study, a medial femoral condyle and tibial plateau shapes were created using FDM 3D-printing [120]. Although the scaffolds were not directly 3D-printed, they were created by first 3D-printing negative molds, into which alginate and BMSCs were injected for the bone-forming layer. The chondral layer was a cell sheet formed from a 4:1 ratio of co-cultured porcine-derived BMSCs to chondrocytes, which was glued with fibrin to the BMSC-seeded alginate. Both femoral and tibial biphasic constructs were formed separately and cultured together for an additional 4 weeks before implanting subcutaneously for 8 weeks in nude mice. Signs of cartilage formation in the femoral condyle and tibial plateau were evidenced by positive staining for collagen II and sGAGs.

In a different femoral condyle study, a large osteochondral scaffold was constructed with a robust interface [89]. Large, anatomically shaped (i.e., ovine), medial femoral condyle constructs (31 x 14 x 10 mm) were formed in stages. First, porous hydroxyapatite

was CAD/CAM machined into a porous, interdigitating femoral condyle-shaped scaffold. Next, neocartilage was formed from self-assembled juvenile ovine articular chondrocytes. After 5-weeks of *in vitro* culture, neocartilage formation was visualized by histology for GAGs and immunohistochemistry for collagen II, which were localized to the outer region of the construct. Then, the neocartilage was placed onto the porous hydroxyapatite, and cultured in a culture chamber that was polyjet 3D-printed. To encourage interface integration across the interface, a 20 g mass was applied to the construct during tissue culture. The two phases became adhered by ingrowth of the neocartilage into the hydroxyapatite pores during tissue culture. It is noteworthy that the interface was characterized for integration and mechanical interfacial shear strength. A lap shear test was modified for the complex geometry, i.e., the specimen's osteal phase was glued to a popsicle stick and the chondral phase was glued to a strip of paper. The effects of interdigitation depth and interdigitation frequency on interface shear strength were evaluated. Compared to the lower interdigitation depth and lower frequency groups, the group with a depth of 50 μm and a frequency of 4 mm^{-1} exhibited a 4.9-fold higher ultimate shear strength of 83 kPa.

In summary, there are precious few examples in the literature that 3D-printed anatomically accurate osteochondral scaffolds [102], [113]. Detailed anatomy was 3D-printed as a scaffold as early proof-of-concept studies demonstrated [103], [115], [128], [129] [69], [130]. A variety of materials have been employed to construct biphasic 3D-printed scaffolds with an interlocking feature to enhance the scaffold's mechanical performance [63], [106]. Different types of materials generally require different printing methods; for example, cell-laden hydrogels for the cartilage region are generally printed

via a pneumatic extrusion bioprinter with photocrosslinking, whereas biodegradable polyesters for the bone region such as PCL or PLGA are printed via hot-end extrusion (e.g., FDM or polyjet) [63], [67], [71], [105]. Therefore, a key challenge in designing 3D-printed, anatomically accurate, osteochondral scaffolds is the method of integration for differing material types.

Methods of integrating the regions have included co-printing, utilizing tissue culture ingrowth across the interface, or introducing an additional step (e.g., infilling by syringing a hydrogel and crosslinking, suturing, gluing, or culturing under an additional weight). For co-printing applications, the different types of materials are likely to require multiple printheads in the same 3D-printer and require care to ensure the higher temperature with FDM does not adversely affect the hydrogel layer. For cell-culture, additional time is necessary to complete tissue ingrowth. Suturing and gluing include the added challenges that the adhesive technique may damage the biomaterial or introduce artifacts.

We recommend an interlocking strategy that employs an infilling method such as syringing to combine the phases and to exploit the capabilities of 3D-printing to generate robust adhesion at the interface. Although interface strength was rarely emphasized in large, anatomically shaped scaffolds, one study applied a modified lap test to quantify the interface strength and suggested that shear strength be included as a functional index for tissue engineered scaffolds [89]. We recommend that future work consider exploiting extrusion-based 3D-printing to create a robust interlocking interface that is infilled with a hydrogel and cured to form essentially a single, integrated osteochondral scaffold. The use

of an interlocking interface offers potential for translation to anatomically shaped scaffolds that are implanted to restore joint function [107].

2.5 Discussion

There exists great potential for 3D-printing to create scaffolds for regenerating osteochondral structures of complex shapes. There are a limited number of studies that performed interface mechanical tests on 3D-printed osteochondral scaffolds, and even fewer that performed mechanical tests on large anatomically shaped 3D-printed scaffolds. A total of five studies were identified that performed interface shear testing on 3D-printed osteochondral scaffolds. For studies with simple geometries (e.g., cylinder), interface shear tests have been performed by displacing the chondral phase until failure. Although complex geometries may require alternative shear testing methods (e.g., lap tests), we generally recommend the use of interface shear tests. The interface shear test was performed in previous studies of interface strength. The interface shear test emphasizes a shear failure mode, and is relevant to the physiologic environment [74]. We recommend that the interface shear test be performed with a constraining platen to improve reproducibility. The reproducibility advantage with a constraining platen derives from the limited the amount of opening failure, and absence of a requirement for adhesives to grip the specimen.

The interlocking interface provides an invaluable strategy for future work. For future interlocking strategies, our field may look to clinical dentistry for valuable precedent. In clinical dentistry, composite tooth restorations achieve high strength adhesion through a micromechanical interlocking bond [131], [132], [133]. In a mechanism similar to the interlocking interfaces described in osteochondral scaffolds, the tooth structure in a

restoration procedure is modified with phosphoric acid to introduce an interdigitating structure. Then, a flowable polymer adhesive is infilled to the tooth's prepared surface and photocrosslinked. The resulting micromechanical bond has been proven for decades to provide sufficient adhesion for tooth restorations that are subject to harsh mechanical and chemical challenges in the mouth. Successes in dentistry with a mechanically interdigitating approach reaching an interface bond strength of 10-15 MPa is an inspiration for enhancing interface strength in osteochondral tissue engineering [131], [134].

Additionally, this interlocking strategy inspired by dental materials provides a versatile platform for use with a multitude of materials. The infilling material is required only to have sufficient rheological properties to infill the interlocking interface (e.g., hydrogels, curable polymers, or cements). Thus, a wide range of materials may be selected for osteochondral 3D printing, some of which may have outstanding chondrogenic properties, to provide an interlocking osteochondral scaffold with high interface strength. Furthermore, the interlocking strategy provides a practical method for assembling the chondral phase together with the osteal phase. Once the interlocking structure of the osteal phase has been formed, assembly of the osteochondral scaffold only requires infilling and curing of the chondral phase. Although no additional adhesives are required to assemble an interlocking scaffold, the interlocking strategy may accommodate chemical bonding or other strategies such as etching to further enhance interface strength. It may be wise to consider an interlocking interface in future designs of anatomically shaped scaffolds. Additional adhesion strategies (e.g., chemical bonding, solvent casting, and tissue culture ingrowth) may be combined with the interlocking interface to further enhance performance.

Looking to the future, partially degradable 3D-printed metals may be better suited to joint loading applications in the knee or hip, but these materials have generally been designed only for bone regeneration, and have rarely been designed for osteochondral tissue engineering [61], [97], [135]. There is a paucity of studies that investigate metallic anatomically shaped 3D-printed scaffolds [136]; nevertheless, degradable metals may be an intriguing material choice to consider for future 3D-printed, anatomically-shaped, osteochondral scaffolds for regenerative medicine.

As a relatively new field of research, there are gaps in the literature with the opportunity to be filled. For example, full scale scaffolds that match the size of current metallic total joint replacement implants are currently rare in the literature. However, there exist FDM 3D-printers that are capable of printing parts with a build volume that easily accommodates the printing of typical knee replacement components [137]. Another literature gap is the use of standard evaluations that are currently employed in joint replacement materials such as fatigue and wear performance, which to date have not been included in 3D printed, osteochondral, shape-specific scaffolds. However, it is understood that these methods employed with total joint replacements generally pertain to a plastic surface articulating against a metal surface, and that alternative standardized testing may need to be developed for approval to market 3D-printed scaffolds for osteochondral regeneration of complex joint surfaces in the future for human application in the clinic.

Another gap in the osteochondral literature is that although anatomically shaped scaffolds have been 3D-printed, the shape fidelity is generally not characterized. 3D-prints for cardiovascular applications have, however, included shape-fidelity measurements [123]. As 3D-printing technology continues to become more accessible and streamlined in

the future, additional evaluation of accuracy and precision in 3D-printed anatomically shaped scaffolds are likely to be expected by clinical care providers, editors, funding agencies, and regulatory agencies.

A crucial limitation in the literature pertains to *in vivo* evaluation in load-bearing applications. Specifically, 3D-printed, anatomically shaped scaffolds placed orthotopically to restore load-bearing joints have been limited to the TMJ mandibular condyle. Although orthopedic joint studies exist that have included 3D-printed scaffolds shaped as the femoral condyle or tibial condyle, these scaffolds were not evaluated by orthotopic *in vivo* implantation.

Another literature gap pertains to mechanical characterization of the osteochondral scaffold interface. Although extraordinary care has been given in the literature to enhanced adhesion of the interface, quantitative characterization of interface strength has rarely been performed. The non-planar interface of anatomically shaped scaffold has introduced additional challenges for characterizing interface strength, which may be addressed by modification of the interface shear strength test.

Another gap that may increase in importance is that the appropriate pore size for various osteochondral tissue regeneration applications remains unclear. A feasible range from 150 μm up to 600 μm for anatomically shaped architectures has been advised, but further evaluation specific to given materials and printing strategies may be warranted.

Although it is commonly accepted that not all joints require the same amount of load support, 3D tissue printing studies have generally not accounted for the specific load support requirements for anatomically shaped osteochondral scaffolds. Computational modeling offers a valuable tool for estimating a scaffold's mechanical behavior under

complex loading conditions in the joint, and has been employed to characterize stress distributions in osteochondral scaffolds [138]. Unfortunately, validated computer models that elucidate the stresses in novel 3D-printed osteochondral scaffolds under complex joint loads are not readily available. Advances in computer modeling provide a valuable predictor of material behavior that have aided medical device FDA approval [139]. In 2011, the FDA published a strategic plan that highlighted priority areas for advancing regulatory science, in which computational modeling and simulation was identified as a tool [140], [141]. In 2020, the FDA recognized an American Society for Testing and Materials (ASTM F3334-19) consensus standard for the use of computer modeling in medical device regulatory processing of total knee tibial components to alleviate the burdens of physical testing [142] [143]. Computer models may therefore provide a helpful tool to accelerate the design process for the mechanical performance of osteochondral scaffolds [144].

As an important consideration for the future, all patient-fitted 3D-printing begins with 3D-imaging from patient scans that are segmented to create a digital scaffold [145]. Thus, limitations to imaging technology are an essential factor in the translational potential of 3D-printing. Current clinical CT equipment generate volumetric 3D-imaging with a spatial resolution of ~90-300 μm [146], [147], and with scan times close to 20 s [147]. MRI scans have been employed to identify specific patient subchondral bone and cartilage interface architecture; however, MRI scans pose a risk for artifacts from motion during the long scan times estimated at 5-9 min [146], [148], [149]. Although fully recreating trabecular features may require smaller imaging resolutions under 100 μm, clinical CTs with resolutions of 287 μm demonstrated practical use for characterizing subchondral bone yielding applicability similar to that of 35 μm micro-CT [150]. The current 3D-printing

resolutions ranging from approximately 1 to 150 μm are lower than clinical imaging resolutions, suggesting that technical improvements in imaging and 3D-printing resolution for an added range of materials are anticipated to further expand the translational applications of 3D-printing.

2.6 Conclusion

The current review underscores the importance of 3D-printing for integrated osteochondral constructs. 3D-printing has demonstrated capabilities for producing multiphasic scaffolds that are of the appropriate size and shape to regenerate large osteochondral tissues. Interface integration may be enhanced by 3D-printing with design considerations for interdigitation frequency and other microarchitectural complexities beyond that of a simple crosshatch pattern. Differences in material properties in the respective bone and cartilage phases were important to interface stress, underscoring the value of stiffer chondrogenic hydrogels that more closely match the osteal phase stiffness. Overall, 3D-printing demonstrated up to 6.5-fold potential gains in interface shear strength by simply including interface interlocking designs. The interface shear test is the test of choice for quantifying 3D-printed scaffold layer integration. Furthermore, enhancements to the patterning of bioactive signals in osteochondral constructs was demonstrated by using 3D-printing to produce scaffolds with bioactive molecules or cells for specific chondral and osteal regions of the scaffold.

There is a need for further exploration of 3D-printed design, materials, and enhanced interface performance. Future work may combine the interlocking interface strategy with other bonding strategies (e.g., covalent binding). Full-sized anatomically

shaped scaffolds may be 3D-printed and evaluated with more advanced quality assurance methods (e.g., shape fidelity measurements). Computational modeling and simulations may provide a useful tool for accelerating the design process. Currently available 3D-printer build volumes and resolutions appear to satisfy the needs of orthopedics; however, there is a need for improved material properties, and imaging technology to apply 3D-printed scaffolds to all load-bearing joints. The current state of the literature suggests many exciting developments on the horizon for 3D-printed osteochondral scaffolds with anatomically accurate geometries.

Chapter 3: The Ogden model for hydrogels in tissue engineering: Modulus determination with compression to failure[2]

3.1 Abstract

Hydrogel mechanical properties for tissue engineering are often reported in terms of a compressive elastic modulus derived from a linear regression of a typically non-linear stress-strain plot. There is a need for an alternative model to fit the full strain range of tissue engineering hydrogels. Fortunately, the Ogden model provides a shear modulus, μ_0, and a nonlinear parameter, α, for routine analysis of compression to failure. Three example hydrogels were tested: (1) pentenoate-modified hyaluronic acid (PHA), (2) dual-crosslinked PHA and polyethylene glycol diacrylate (PHA-PEGDA), and (3) composite PHA-PEGDA hydrogel with cryoground devitalized cartilage (DVC) at 5, 10, and 15%w/v concentration (DVC5, DVC10, and DVC15, respectively). Gene expression analyses suggested that the DVC hydrogels supported chondrogenesis of human bone marrow mesenchymal stem cells to some degree. Both linear regression (5 to 15% strain) and Ogden fits (to failure) were performed. The compressive elastic modulus, E, was over 4-fold higher in the DVC15 group relative to the PHA group (129 kPa).

Similarly, the shear modulus, μ_0, was over 3-fold higher in the DVC15 group relative to the PHA group (37 kPa). The PHA group exhibited a much higher degree of nonlinearity (α=10) compared to the DVC15 group (α=1.4). DVC hydrogels may provide baseline targets of μ_0 and α for future cartilage tissue engineering studies. The Ogden model was demonstrated to fit the full strain range with high accuracy ($R^2 = 0.998 \pm 0.001$) and to quantify nonlinearity. The current study provides an Ogden model as an attractive alternative to the elastic modulus for tissue engineering constructs.

3.2 Introduction

Mechanically robust hydrogels offer many clinical advantages for cartilage regeneration. Tissue engineering studies often estimate hydrogel stiffness with compressive elastic moduli based on low strain regions up to 20% [151]. Though it has been demonstrated that native cartilage generally may not exceed 10% strain [152], constructs implanted in arthritic or damaged cartilage may be subjected to high strains *in vivo*. Unfortunately, with typically nonlinear stress-strain data, compressive elastic modulus calculations based on linear regression depend on a user-defined strain range [151], [153], [154], which limits the ability to make comparisons among studies. For example, tangent moduli at high strains (30%) were 3-4 times higher than those from the same data set at 5% strain [151].

Nonlinear hyperelastic models such as the neo-Hookean, Mooney-Rivlin, or Ogden models could be used to model nonlinear hydrogel compression data [155], [156], [157], [158]. Models with many parameters offer improved general stress predictions, but their

complexity may be difficult for widespread adoption and unnecessary for a more straightforward comparison with one loading configuration (i.e., uniaxial compression).

The one-term Ogden model is a relatively straightforward equation to capture nonlinear behaviors of different hydrogels for tissue engineering under compression to failure. The Ogden model has been employed for over 50 years [159] to accurately model nonlinear mechanical behaviors for a wide range of materials (e.g., rubber, cartilage, brain, liver, and kidney) including hydrogels [159], [160]. The one-term Ogden model is well suited to nonlinear data with its two parameters: (1) the shear modulus, μ_0, and (2) a nonlinear parameter, α. When $\alpha = 2$, the Ogden model reduces to a neo-Hookean model, which is a simpler model without the Ogden's model's flexibility for nonlinear fitting. Compared to other phenomenological models (e.g., neo-Hookean, Mooney-Rivlin, Demiray, or Gent models), the one-term Ogden model may provide a fairly accurate stress representation across different loading conditions including compression [161], [162] and be expressed in a relatively straightforward mathematical form.

The purpose of the current study was to evaluate neo-Hookean and Ogden model fits to the stress-strain behaviors of representative hydrogels for tissue engineering. Three different representative hydrogels were selected for mechanical analysis: (1) a biopolymer-derived pentenoate-modified hyaluronic acid (PHA) hydrogel [163], (2) a dual crosslinked biopolymer-synthetic composite hydrogel with PHA and polyethylene glycol (PHA-PEGDA) [164], and (3) a biopolymer-synthetic composite (PHA-PEGDA) loaded with putatively bioactive devitalized cartilage particles (DVC) derived from cartilage matrix at 5, 10, and 15% w/v (DVC5, DVC10, and DVC15) [165]. The DVC hydrogels were

selected as reasonable examples to evaluate the Ogden model due to their potentially advantageous mechanical and biological performance for cartilage tissue engineering.

3.3 Materials and methods

3.3.1 Materials

All materials were purchased from Sigma-Aldrich (St. Louis, MO) unless stated otherwise. All cell culture and *in vitro* study supplies were obtained from Thermo Fisher Scientific (Waltham, MA) unless otherwise stated.

3.3.2 PHA synthesis and Nuclear Magnetic Resonance (NMR) characterization

PHA was synthesized as previously described from 1.5 MDa hyaluronic acid (HA, Lifecore Biomedical, Chaska, MN) [166]. Briefly, HA was dissolved (0.5% w/v) in deionized (DI) water and dimethylformamide (DMF) at a 3:2 water to DMF ratio. 4-dimethylamino pyridine was added at 0.25 g per g of HA. 4-pentenoic anhydride was added at a 10-fold molar excess to HA. The pH was maintained between 8-9 using 4M NaOH. Once stabilized for 1 h, the reaction proceeded overnight. Afterward, sodium chloride was added to 0.5M and the PHA was precipitated with acetone using 4 times the reaction volume. Precipitated PHA was then centrifuged and the acetone was discarded. Dialysis for 48 h (MWCO: 6-8 kDa, VWR, Radnor, VA) was then used to purify PHA dissolved in DI water. The functionalized PHA solution was then frozen and lyophilized on a FreeZone 6 Plus lyophilizer (Labconco, Kansas City, MO, USA) before storage at -20°C.

NMR characterization of PHA for degree of substitution was performed as previously described [166]. Scans were performed using a Varian VNMRS-500 MHz

NMR Spectrometer (Palo Alto, CA) at -80°C. Of the repeating disaccharide units, 40% were functionalized in the current study.

3.3.3 DVC processing

Porcine knees were obtained from a local abattoir and cartilage was harvested and stored at -20°C (Hampshire and Berkshire, female, 1 year old, 180-220 kg). The cartilage was washed in DI water and processed into a cryoground powder as previously described [167] using a SPEX 6770 Freezer/Mill (SPEX SamplePrep, Metuchen, NJ, USA). The DVC was lyophilized and stored at -20°C.

3.3.4 Hydrogel preparation and crosslinking

For all hydrogels, PHA concentrations were 4% w/v and PEGDA were 20% w/v, PEGDA 4 kDa used throughout. Increasing DVC concentrations of 5, 10, and 15% w/v were used, resulting in the following hydrogel groups: (1) PHA, (2) PHA-PEGDA, (3) PHA-PEGDA-DVC$_{5\%}$ (DVC5), (4) PHA-PEGDA-DVC$_{10\%}$ (DVC10), and (5) PHA-PEGDA-DVC$_{15\%}$ (DVC15). For all mixtures, PHA was dissolved in phosphate buffered saline (PBS) at a 2-fold concentration and mixed. Once fully dissolved, the photoinitiator, 6.5% w/v lithium phenyl-2,4,6-trimethylbenzoylphosphinate (LAP; 98%; TCL0290-1G) (TCI America; Portland, OR, USA), and crosslinker, 3% w/v dithiothreitol (DTT), were prepared in the remaining PBS to ensure a 1:1 thiol:ene molar ratio for all composites. For PEGDA-containing hydrogels, the crosslinker and photoinitiator were mixed with PEGDA and PBS before combining with PHA and/or DVC. Precursor mixtures were spatulated for at least 15 min prior to backloading into a syringe for application. Hydrogels were photocrosslinked with a 365 nm light at 1280 μW·cm^{-2} for 10 min (EA-160, Spectroline,

Westbury, NY), submersed in PBS overnight at 37°C, and sectioned into 6 mm diameter cylinders with a 6 mm biopsy punch from a 1 mm thick mold.

3.3.5 Cell culture

Human bone marrow mesenchymal stem cells (hBMSCs), originally isolated from a 19-year-old male's healthy iliac crest, and expansion medium were obtained from Rooster Bio, Inc. (Cat# MSC-003, SU-022, SU003, Frederick, MD). Cells were cultured according to manufacturer protocols and passaged every 2-3 days or when confluent using trypsin-EDTA (0.25%).

The base medium consisted of GlutaMAX-I supplement (2 mM; 10566024), penicillin-streptomycin (1%; 15140122), insulin-transferrin-selenium+premix (1%; CB40352), non-essential amino acids (1%; 11140050), sodium pyruvate (1 mM; 11360070), and ascorbate-2-phosphate (50 µg·mL^{-1}; A8960), dexamethasone (100 nM; Sigma-Aldrich, D4902), and mixed with Dulbecco's modified eagle medium (Cat# 10566024). For the chondrogenic medium, 10 ng·mL^{-1} TGF-β3 (R&D Biosystems, Minneapolis, MN; 8420-B3-005) was supplemented to the base medium.

3.3.6 Real-time quantitative polymerase chain reaction

Hydrogels were fabricated under sterile conditions as described above and allowed to equilibrate overnight in PBS at 37°C. Passage 3 cells were seeded (200 cells·µL^{-1}) on each hydrogel in base or chondrogenic medium in 96-well plates. Plates were kept in hypoxic conditions (i.e., 37°C, 5% carbon dioxide, 5% oxygen) with media replenished every 3 days. All samples were prepared for quantitative reverse transcription polymerase chain reaction (RT-qPCR) after 24 days.

A qTOWER (Analytik Jena; Jena, Germany) was used as previously described for RT-qPCR [163], [165]. The following TaqMan Gene expression assays were used: **(1)** GAPDH (Rn01775763_g1), **(2)** aggrecan (ACAN, Rn00573424_m1), **(3)** collagen type I (COL1A1, Rn01463848_m1), **(4)** collagen type II (COL2A1, Rn01637087), and **(5)** SOX9 (SOX9, Rn01751070). Relative gene expression levels were calculated using the $2^{-\Delta\Delta Ct}$ method [168]. The comparator group used to normalize all data was PHA-PEGDA in base medium except for COL2A1. COL2A1 expressions below the detection limit required normalization to PHA-PEGDA in chondrogenic medium (n=8).

3.3.7 Unconfined compression to failure

Specimens (n=6-8) were placed in a Discovery Hybrid Rheometer-2 (TA Instruments, New Castle, DE) equipped with an 8 mm diameter stainless steel parallel plate geometry. Immediately after removing from a PBS bath stored at 37˚C overnight, specimen diameters were punched with a 6 mm diameter biopsy punch, and heights measured at a tare load of 0.01 N. The testing plate was wetted with PBS to reduce adhesion between the specimen and testing plates. Tests were performed at a rate of 5 $\mu m \cdot s^{-1}$ ($0.5\% \cdot s^{-1}$) to approximate quasistatic conditions. Testing continued beyond failure, defined as the highest load after which the load monotonically decreased. The compressive elastic modulus was determined from a linear fit to the 5-15% strain range of the stress/strain curve. The failure stress was designated as the maximum stress, and the failure strain was designated as the strain corresponding to the maximum stress. The energy to failure was determined by the area under the stress-strain plot up to the failure strain.

The single-term Ogden model was fit to the full strain range. The Ogden strain energy equation is [169]

$$W(\lambda_1, \lambda_2, \lambda_3) = \sum_{j=1}^{N} \mu_j \left(\lambda_1^{\alpha_j} + \lambda_2^{\alpha_j} + \lambda_3^{\alpha_j} - 3 \right) / \alpha_j \qquad (1)$$

where λ_i are the principal stretches (λ=strain+1, with strain < 0 and therefore 0 < λ < 1 for compression), μ_j are material constants, and α_j are nonlinear parameters. The equation is used with N terms, typically three or four terms for rubber [170], but here the one-term Ogden model (N=1), which is widely used in biomechanics, was employed [171]. The Cauchy stress for incompressible, uniaxial boundary conditions

$$\sigma_i = \lambda_i \frac{\partial W}{\partial \lambda_i} - p \qquad (2)$$

was solved for the 3-direction (i.e., z-direction), where p is the Lagrange multiplier, by solving the derivative in Eq. (1) and substituting into Eq. (2) (with N=1) to obtain

$$\sigma_3 = \mu \lambda_3^{\alpha} - p \qquad (3)$$

From the boundary conditions, $\sigma_1 = \sigma_2 = 0$ was substituted into Eq. (2) to solve the Lagrange multiplier, p, with the 2-direction as an example:

$$\sigma_2 = \mu \lambda_2^{\alpha} - p = 0 \qquad (4)$$

making use of the isovolumetric assumption ($\lambda_1 \lambda_2 \lambda_3$=1), and boundary condition, $\lambda_1 = \lambda_2 = \lambda_3^{-1/2}$ [160], [172], p was solved in terms of λ_3.

$$p = \mu \lambda_3^{-\alpha/2} \qquad (5)$$

The first Piola-Kirchhoff stress (i.e., engineering stress) is

$$P_3 = \sigma_3 / \lambda_3 \qquad (6)$$

Inserting Eq. (3) and (5) into equation (6):

$$P_3 = \mu \left(\lambda_3^{\alpha-1} - \lambda_3^{-\frac{\alpha}{2}-1} \right) \qquad (7)$$

P_3 was fit directly to compression stress data (negative values for compression), and along with stretch data were used to calculate μ and α using MATLAB (MathWorks, Inc., Natick, MA).

The identity $2\mu_0 = \mu\alpha$ from Ogden's original work was subsequently employed to obtain the conventional shear modulus, μ_0 [159]:

$$\mu_0 = \frac{\mu\alpha}{2} \tag{8}$$

Eq. (7) was chosen to fit data instead of the form that directly includes μ_0 (i.e., if Eq. (8) were substituted into Eq. (7)) thus ensuring a unique solution with $\alpha > 0$, consistent with the Hill stability criterion, without the need for prescribed fitting bounds [173]. In compression, where $\lambda_3 < 1$, the λ_3 term in Eq. (7) with the negative exponent (i.e., the negative term, which is from the Lagrange multiplier) dominates at higher strain magnitudes, providing a negative value on the right-hand side of the equation that is consistent with compression data where $P_3 < 0$. If Eq. (8) were to be substituted into Eq. (7) prior to fitting to data, an additional, undesirable solution with $\alpha < 0$ would become possible, with the other term (i.e., the positive term) having the negative exponent and thereby dominating at higher strain magnitudes, again resulting in a negative P_3.

In addition, neo-Hookean model fits were performed by inserting $\alpha=2$ in Eqs. (7) and (8):

$$P_3 = \mu_0\left(\lambda_3 - \frac{1}{\lambda_3{}^2}\right) \tag{9}$$

3.3.8 Statistical Analysis

GraphPad Prism version 9.3.1 (GraphPad Software, San Diego, CA, USA) was used to perform all statistical analyses. A one-way analysis of variance (ANOVA) test with Tukey's honestly significant difference post-hoc test was used to compare multiple groups. Outlier analysis was performed on RT-qPCR data using Prism's robust regression and

outlier removal method ROUT (Q = 1%) [174]. The significance level was α = 0.05. All results were reported as mean ± standard deviation.

3.4 Results

3.4.1 Cell response to cartilage-matrix hydrogels

Higher DVC concentrations enhanced chondroinductivity relative to PHA-PEGDA, with higher ACAN expression in base medium, and higher SOX9 expressions in both medium conditions (**Fig. 3.1**). More specifically, the DVC10 and DVC15 groups both exhibited over 5-fold increases in ACAN expression compared to the PHA-PEGDA and DVC5 groups in the base medium ($p < 0.05$) (**Fig. 3.1A, B**). In base medium, the DVC15 group exhibited a 4.2-fold higher SOX9 expression relative to the PHA-PEGDA group in base medium ($p < 0.05$), and in chondrogenic medium the SOX9 expression was 1.9-fold higher ($p < 0.05$) (**Fig. 3.1C, D**). Despite the high expression of ACAN and SOX9 genes, COL2A1 was undetectable for all groups with the base medium. With chondrogenic medium, COL2A1 was detected in every group, with no significant differences among groups (**Fig. 3.1E, F**). COL1A1 exhibited a range of expression levels (0.7 and 1.3) across the hydrogels in both media (**Fig. 3.1G, H**).

3.4.2 Hydrogel elastic and failure properties

The compressive elastic modulus was lowest in the PHA group (129 kPa), with 3.2, 3.7, and 3.9-fold larger moduli for the DVC5, DVC10, and DVC15 groups, respectively ($p < 0.05$) (**Fig. 3.2C**). DVC-containing hydrogels exhibited over 2.4-fold higher elastic moduli compared to PHA-PEGDA ($p < 0.05$). DVC10 and DVC15 exhibited 13 and 21% higher elastic moduli, respectively, than DVC5 ($p < 0.05$).

The ultimate stresses for all the hydrogel groups ranged from 343 to 389 kPa, with no significant differences among groups (**Fig. 3.2D**).

The failure strain magnitudes for the PHA-PEGDA, DVC5, DVC10, and DVC15 groups were 1.21, 1.07, 1.10, and 1.13-fold higher than the failure strain magnitude for the PHA group (47%), respectively ($p < 0.05$) (**Fig. 3.2E**). The ultimate strain magnitude of the DVC15 group was 6% higher than that of the DVC5 group ($p < 0.05$).

The PHA group exhibited an energy to failure of 35 $kJ·m^{-3}$. The energies to failure of the DVC groups were over two times higher than that of the PHA group ($p < 0.05$), and the PHA-PEGDA group energy to failure was 57% greater than that of the PHA group ($p < 0.05$) (**Fig. 3.2F**).

In summary, adding PEGDA enhanced the failure strain and energy to failure of the PHA hydrogels, and the further addition of DVC enhanced the compressive elastic modulus of the PHA-PEDGA hydrogels. Increased DVC content did not impact the failure behaviors of PHA-PEGDA.

3.4.3 Hydrogel shear moduli and nonlinear properties

The stress/strain data for all hydrogels exhibited pronounced nonlinearity above ~30% strain magnitudes (i.e., $\lambda < 0.7$). The nonlinear parameter, α, was highest in PHA hydrogels (10), 57% less for the PHA-PEGDA group, 80% less for the DVC5 group, and 86%, and 87% less for the DVC10 and DVC15 groups, respectively ($p < 0.05$). No significant differences in α were exhibited among the DVC groups (**Fig. 3.3B**), where values of α were all near the neo-Hookean model simplification of $\alpha = 2$.

The shear moduli, μ_0, exhibited a trend like that of the compressive elastic moduli described above. The shear modulus was lowest in the PHA group (37 kPa) and was 1.4-

fold higher in the PHA-PEGDA group, and 2.9 to 3.0-fold higher in the DVC groups (p < 0.05) (**Fig. 3.3C**).

Overall, the Ogden model fit the data from all the hydrogel groups well ($R^2 = 0.998 \pm 0.001$) (**Fig. 3.4**). Although the neo-Hookean model fit the data from the PHA-PEGDA and DVC groups fairly well ($R^2 \geq 0.98$), it was unable to fit the PHA group data well ($R^2 = 0.8 \pm 0.03$). Relative errors for the neo-Hookean model were higher than the Ogden model for the PHA and PHA-PEGDA groups but were comparable for the DVC groups (**Fig. 3.4**).

The E/μ_0 ratios for the PHA and PEGDA groups ranged up to 3.5 and were between 3.8 and 4.5 for the DVC groups (**Table 3.1**).

3.5 Discussion

The Ogden model provided an accurate fit for all five representative hydrogel groups across the full range to failure (>40% strain magnitude). The neo-Hookean model, with its simpler mathematical form, fit DVC hydrogels well, but the neo-Hookean model did not capture the highly nonlinear behavior of PHA and PHA-PEGDA with the high accuracies of the Ogden model, which quantified the degree of nonlinearity. More sophisticated models with multiple parameters and terms (e.g., 4th-order weak form nonlinear, or a three-term Ogden) may provide increasingly accurate fits [156], [170], but that additional complexity may not be necessary for uniaxial compression of hydrogels for tissue engineering. Here, in addition to other studies [161], [175], the one-term Ogden model provided a balance between mathematical simplicity and an accurate fit to the data. Insomuch as stiffness is an indicator of engineered tissue quality, the Ogden model may

offer better estimates of stiffness than the tangent modulus as it does not depend on an arbitrarily defined strain range like the tangent modulus.

Both shear and compressive elastic moduli increased with the addition of PEGDA and DVC. For linearly elastic, homogeneous, isotropic, incompressible solids, the shear modulus, μ_0, and the compressive elastic modulus, E, follow the relation, $E/\mu_0=3$ at infinitesimal strains. With the caveat and understanding that the E came from a linear fit to nonlinear data over a somewhat arbitrarily determined strain range, ratios of exactly 3 would not be expected, but consideration of this ratio can provide a helpful point of comparison. It is helpful context to note that the E/μ_0 ratios in the current study (3.2-4.5) were relatively consistent with each other and with those that were previously reported (~3-4) for a neo-Hookean model with agarose-PEGDA hydrogels [176], [177].

Previously published [176] interpenetrating networks comprised of agarose and PEGDA exhibited a lower shear modulus of 40.0 kPa than the composite PHA-PEGDA hydrogels of the current study (up to 113 kPa). The prior data were captured in unconfined compression at a lower strain rate (0.5 μm·s^{-1}) than the current study (5 μm·s^{-1}) and fit with a neo-Hookean model. Another study reported μ_0=868.5 kPa for human knee cartilage using a one-term Ogden model, but specimens were tested in compression and tension at a higher strain rate (13%·s^{-1}) than the current study (0.5%·s^{-1}) while glued to the grips [158]. The DVC groups may provide a reasonable baseline for cartilage tissue engineering for μ_0 and α of approximately 100 kPa and 1.5, respectively, until future studies can provide a more comprehensive target range. Ogden model target values must include both μ_0 and α because they are not independent.

44

In the current study, hydrogels with low α values (i.e., DVC) exhibited less strain-stiffening (i.e., less nonlinear) than those with higher α values (i.e., PHA and PHA-PEGDA). Generally, additional Ogden terms (or an alternative model) are recommended when fitted α values exceed 10 to 20 [171]. For a more detailed discussion of how α describes nonlinearity, the reader is referred to [175]. Inferior engineered tissue quality may potentially be associated with nonlinearity (i.e., higher α), but that remains to be explored in future work.

Energies to failure of hydrogels in the current study ($\sim$70 kJ·m^{-3}) were less than a curdlan/polyacrylamide double network synthetic hydrogel's 4.4 MJ·m^{-3} [179], but similar to an alginate/chitosan-based double network hydrogel (89.7 kJ·m^{-3}) [178]. The energies in the current study (i.e., toughness values) followed a trend exhibited by both the shear and compressive moduli (i.e., increased from PHA to PHA-PEGDA-DVC composites).

Evidence of chondrogenesis with the hydrogels containing DVC (e.g., SOX9 and aggrecan upregulation) supported the inclusion of the DVC-containing groups as reasonable examples for evaluation with the Ogden model (Brown et al., 2022; Haghwerdi et al., 2021; Huang et al., 2022; Rathan et al., 2019; Baei et al., 2021; Beck et al., 2016a; Rathan et al., 2019).

Like all constitutive relations, the Ogden model has limitations. The stress-strain profile is rate-dependent, thus the parameters the Ogden model provides depend on the strain rate. To achieve quasistatic conditions, ramp rates are advised to be on a scale similar to the characteristic time for gel diffusion [181]. For the purposes of this study, a commonly used tissue engineering study rate of 5%·s^{-1} was applied, though lower rates may be considered [177]. The Ogden equation used here assumes incompressibility (i.e., a

Poisson's ratio of v=0.5 at low strains) and provided a high-quality fit. However, if additional complexity is warranted in future studies, a compressible model is available [169]. For example, highly permeable hydrogels under high compression beyond 50%, heterogeneous hydrogels, or composite hydrogels with anisotropic or transversely isotropic reinforcement structures may exhibit limitations with the Ogden model fit. The Ogden model is phenomenological and thus does not have physical constants for the material microstructure. However, a derivation with appropriate constraints demonstrated equivalency between the Ogden model and a non-affine, non-Gaussian 3-chain model [182]. Mixture theory and biphasic or triphasic models offer valuable insights regarding time-dependent behaviors [157], [183], [184]. Mixture theory carries the advantage of theoretical derivations being based on the cartilage structure, but the model complexity may require substantial effort for tissue engineering groups to adopt. The Ogden model has the advantages of high adaptability and quality fit across a broad strain range for data commonly collected in tissue engineering studies.

3.6 Conclusions

A basic, one-term Ogden model provided accurate comparisons of multiple tissue engineering hydrogel groups under unconfined compression for the entire stress-strain profile to failure. Rather than applying a linear fit to nonlinear data over a limited and arbitrarily-selected strain range to obtain an elastic modulus, as is common practice in tissue engineering studies, the one-term Ogden model adds only one more parameter beyond a modulus value, specifically the α parameter that provides valuable information by quantifying deviation from linearity.

Given the Ogden model's versatility, straightforward form, over 50-year history of success in fitting nonlinear experimental data, and unsupervised fitting process that need not be defined *a priori*, the Ogden model proved to be a valuable alternative to the linear, compressive elastic modulus. Consistent modulus determination using the Ogden model may help provide well-defined design goals for successful tissue engineering constructs.

Chapter 4: Regenerative Engineering of a Biphasic Patient-Fitted Temporomandibular Joint Condylar Prosthesis[3]

4.1 Abstract

Regenerative medicine approaches to restore the mandibular condyle of the temporomandibular joint (TMJ) may fill an unmet patient need. Here, a method to implant an acellular regenerative TMJ prosthesis was developed for orthotopic implantation in a pilot goat study. The scaffold incorporated a porous, polycaprolactone-hydroxyapatite (PCL-HAp, 20wt% HAp) 3D-printed condyle with a cartilage-matrix-containing hydrogel. A series of material characterizations were used to determine the structure, fluid transport, and mechanical properties of 3D-printed PCL-HAp. To promote marrow uptake for cell seeding, a scaffold pore size of 152 ± 68 μm resulted in a whole blood transport initial velocity of 3.7 ± 1.2 mm·s^{-1} transported to the full 1 cm height.

The Young's modulus of PCL was increased by 67% with the addition of HAp, resulting in a stiffness of 269 ± 20 MPa for etched PCL-HAp. In addition, the bending modulus increased by 2.06-fold with the addition of HAp to 470 MPa for PCL-HAp. The prosthesis design with an integrated hydrogel was compared with unoperated contralateral control and no-hydrogel group in a goat model for 6 months. A guide was used to make the condylectomy cut, and the TMJ disc was preserved. MicroCT assessment of bone suggested variable tissue responses with some regions of bone growth and loss, though more loss may have been exhibited by the hydrogel group than the no-hydrogel group. A benchtop load transmission test suggested that the prosthesis was not shielding load to the underlying bone. Although variable, signs of neocartilage formation were exhibited by Alcian blue and collagen II staining on the anterior, functional surface of the condyle. Overall, the current study demonstrated signs of functional TMJ restoration with an acellular prosthesis. There were apparent limitations to continuous, reproducible bone formation, and stratified zonal cartilage regeneration. Future work may refine the prosthesis design for a regenerative TMJ prosthesis amenable to clinical translation.

4.2 Introduction

The temporomandibular joint (TMJ) is essential to many daily life functions such as speaking, laughing, mastication, and upper-airway support. Though TMJ disease prevalence is high, affecting up to 12% of the overall population [1], [5], treatment with a TMJ total joint prosthesis is indicated only for a select patient population of the approximately 1 in 800 who have open surgery [185], [186]. Inflammatory TMJ arthritis, recurrent fibrous and/or bony ankylosis, failed autogenous or alloplastic reconstruction,

resorption, and trauma are among indications for a TMJ prosthesis [187], [188], [189]. Current TMJ prosthesis biomaterials cannot accommodate pediatric patient growth, and may not be appropriate for patients with metal hypersensitivities [190], [191]. Therefore, regenerative medicine approaches are actively being investigated to develop a prosthesis capable of mandibular condylar tissue regeneration [7], [192].

TMJ animal models range from small, such as mouse or rabbit, to large, such as goat or Yucatan minipig [11], [29], [193], [194], [195]. Goat TMJ disc attachments to the condyle are similar to human disc attachments with medial and lateral collateral ligaments [196]. Zhu *et al*.[197], examined coronoid process donor tissue to reconstruct the mandibular condyle of goats. The Almarza group has performed a range of studies to establish baseline knowledge of the goat's TMJ tissue structures and behaviors [29], [198].

Both pre-vascularized and dual perfusion bioreactor-incubation regenerative medicine approaches have recently been pursued for TMJ tissue engineering. Hollister and colleagues[30] implanted a 3D-printed mandibular condyle scaffold coated with bone morphogenetic protein (BMP)-2 into the temporalis muscle of Yucatan mini-pigs. After cellular infiltration and vascularization were established, a horizontal condylectomy was performed and the scaffold was fixed in place. After 6 months, computed tomography (CT) scans and histology suggested vascularization, bone infiltration, and signs of neocartilage formation in the porous condyle scaffold. Chen *et al*.[195], pre-cultured autologous stem cells on subject-specific decellularized bone matrix geometries for 6 weeks prior to implantation. The bioreactor-derived cartilage-bone construct regenerated tissues that more closely resembled control cartilage and subchondral bone tissues than either bone-only or acellular grafts. Previously, our group employed an acellular approach with a

gradient of growth factors in a cylindrical, microsphere-based scaffold to regenerate focal mandibular condyle defects in rabbits [199]. Research to date has reported signs of mandibular condyle bone and cartilage regeneration with a seeded scaffold approach [200], yet a practical approach that can be rapidly produced for off-the-shelf immediate implantation for successful regeneration of continuous bone and cartilage tissues remains elusive.

A resorbable scaffold that can support loads and regenerate mature, stratified cartilage on the articulating surface of regenerated bone leaving no trace of the implanted material remains a common limitation for TMJ tissue engineering [3], [195], [197]. Significant bone regeneration has been documented with porous polycaprolactone (PCL) and hydroxyapatite (HAp) scaffolds [25]. In the current study, a biphasic scaffold prosthesis was assembled from two parts: (1) an anatomically accurate 3D-printed bone regeneration structure comprised of porous polycaprolactone and 20% w/w hydroxyapatite (PCL-HAp), and (2) a potentially chondrogenic hydrogel comprised of photocrosslinkable, 4% w/v pentenoate-modified hyaluronic acid (PHA), 20% w/v polyethylene glycol (PEGDA), and 15% w/v devitalized cartilage (DVC) [163], [165], [167]. Chondrogenesis and mechanical properties of the PHA-PEGDA-DVC hydrogel were previously reported by our group [31]. The 3D-printed PCL-HAp was characterized for structure, mechanical properties, and biofluid transport. A Spanish cross goat model with an approximately human-sized TMJ was used to evaluate tissue regeneration in a pilot study over 6 months of orthotopic implantation [29]. PCL-HAp only, and a biphasic PCL-HAp + PHA-PEGDA-DVC hydrogel-integrated condylar prosthesis were evaluated against native tissues from the contralateral condyle. The purpose of the study was to characterize an

acellular scaffold and regenerate bone throughout the condylar head with cartilage regeneration on the condyle's articulating surface.

4.3 Methods

4.3.1 3D-printing biphasic prosthesis and cartilage-matrix hydrogel synthesis.

Polycaprolactone (PCL, 50 kDa, Polysciences, Inc., Warrington, PA) filament with 20% w/w hydroxyapatite powder (HAp, Aldrich, St. Louis, MO) was made using a filament extruder (Noztek Touch, Shoreham, West Sussex, or Filabot Ex6, Barre, VT). PCL and HAp were mixed with the desired ratio and planetary ball-milled for 6 hours (PQ,N2 Across International, Livingston, NJ), and extruded at 135˚C at a rate of 30 rpm. Filament was fed into a Flashforge Creator Pro printer (Zhejiang, P.R. China) for 3D-printing at 135˚C. For 3-point bend testing, parts were printed on a Cura Lulzbot Taz 6 3D-printer (Lulzbot, Fargo, ND) with the same parameter settings as the Flashforge. A patient-fitted prosthesis was digitally designed using CT scans of each goat (16-slice Philips CT, Amsterdam, Netherlands) with a microporous architecture inside the condylar head **(Fig. 4.1A).** 3D-printed PCL-HAp was then submersed in 5 M NaOH for 30 min, washed 3X in DI water, and sterilized overnight using ethylene oxide. Two different prosthesis groups were made either without a hydrogel (i.e., PCL-HAp only), or with PHA-PEGDA-DVC hydrogel syringed onto the surface and into mechanical integration features.

The hydrogel was synthesized as previously described [31]. Briefly, 1.5 MDa hyaluronic acid (HA, Lifecore Biomedical, Chaska, MN) was dissolved and functionalized with 4-dimethylamino pyridine and 4-pentenoic anhydride added at 0.25 g per g HA and

10-fold molar excess, respectively (Sigma-Aldrich, St. Louis, MO). Functionalized PHA solution was precipitated using acetone, purified, and frozen, before lyophilization on a FreeZone 6 Plus lyophilizer (Labconco, Kansas City, MO, USA) and stored at -20 ˚C.

NMR characterization of PHA was performed as previously described [166] with a 64% functionalization of the disaccharide repeat units.

Porcine knees (Hampshire and Berkshire, female, 1 year old, 180-220 kg) were obtained from a local abattoir to prepare DVC powder from cartilage as previously described [167]. The DVC was lyophilized and stored at -20 ˚C.

Hydrogels were prepared with 4% PHA, 20% PEGDA, and 15% w/v DVC as previously described [31]. The photoinitiator, 2.2 mM lithium phenyl-2,4,6-trimethylbenzoylphosphinate (LAP; 98% ; TCL0290-1G) (TCI America; Portland, OR, USA), was prepared in phosphate-buffered saline (PBS; Sigma-Aldrich). Once dissolved, the crosslinker dithiothreitol (Sigma-Aldrich, St Louis, MO) was added to ensure a 1:1 thiol:ene molar ratio for all composites. Precursor mixtures were spatulated for at least 15 min then syringed onto the 3D-printed scaffold bedside before photocrosslinking for 10 min (365 nm light at 1280 $\mu W \cdot cm^{-2}$, EA-160, Spectroline, Westbury, NY).

CT scans from each goat were registered and implants designed following consultation with TMJ Concepts. Each scan was segmented for the condyle and ramus using Seg3D (University of Utah SCI Institute). The part was enlarged such that a 0.165 mm offset resulted between prosthesis and bone. A condyle cutting plane was derived from points in the superior external auditory meatus and inferior orbit. The implant collar was extruded from the ramus surface and combined with the resected condyle in Meshmixer (San Rafael, CA). All screw holes were 0.094".

4.3.2 Surgical Implantation

All experiments were performed with the approval of the Institutional Animal Care and Use Committee. After a surgical plane of anesthesia was achieved **(Supplemental Fig. 4.1)**, two incisions were performed to gain access to the bone, and permit both the guided condylectomy and the condylar implants insertion **(Fig. 4.1B)**. Initially, a preauricular incision was performed 1 cm below the zygomatic arch, parallel to the posterior border of the mandible with approximately 2.5 cm of extension. After that, another 2.5 cm long retromandibular incision was performed in a curvilinear fashion, following the mandibular angle contour at the level of the mandibular inferior border. The two incisions were separated by a length of approximately 2 cm. After reaching the bone, subperiosteal dissection was accomplished to expose the medial and the lateral aspects of the ramus and condyle, with attention to preserve the disc. After adequate level of dissection was obtained, a custom-made cutting guide was inserted through the retromandibular incision and fixed to the ramus with 4 titanium screws (KLS Martin, Jacksonville, FL), thus providing a planar guide for condyle resection, performed using a Bien-air reciprocating saw (Bien-air Dental, Bienne, Switzerland). The condyle was then disinserted and removed taking care to preserve the disc, and the cutting guide was replaced by the implant, which was fixed in place with 8 screws **(Fig. 4.1C)**.

4.3.3 Load transmission to underlying jaw

To estimate physical forces transmitted to the underlying bone, a uniaxial mechanical testing setup was used to evaluate loads in two locations: (1) applied to the

surface of the condyle, $F_{Applied}$, and (2) $F_{Transmitted}$ measured between the prosthesis condyle and underlying jaw structure with a FlexiForce pressure sensor (Barneveld, Netherlands) **(Fig. 4.2).** The % load transmitted was calculated using the following equation.

$$\% \, Load_{transmitted} = \frac{F_{Transmitted}}{F_{Applied}} \cdot 100\% \tag{1}$$

4.4 Experiment

4.4.1 Animals

Six Spanish cross female goats (initial weight: 33 ± 5 kg, final weight: 52 ± 13 kg, age: 3-5 years) were used in the current study. All goats were purchased and boarded at the University of Oklahoma Health Sciences Center Division of Comparative Medicine. Goats were assigned to two pilot groups for 6-month implantation periods with either no-hydrogel, or a hydrogel integrated prosthesis.

4.4.2 Structural characterization of 3D-printed prosthesis

3D-printed PCL-HAp specimens were sputter coated with gold on a Hummer VI (Anatech Ltd., Battlecreek, MI), and examined under a field emission scanning electron microscope (SEM, Zeiss NEON 40 EsB, Stuttgart, Germany) with 5 kV acceleration voltage. Furthermore, energy dispersive X-ray spectroscopy was used to identify elemental structure.

4.4.3 Uniaxial tensile testing

Uniaxial testing followed American Society for Testing and Materials (ASTM) standard #D1708. Briefly, dogbones with a 5x3mm cross section, and 22 mm gauge length

were extended uniaxially at a rate of 1 mm·min^{-1} in a TestResources uniaxial tester (Shakopee, MN). Three groups were evaluated for tensile properties: (1) PCL, (2) PCL-HAp, and (3) etched PCL (ePCL-HAp). For ePCL-HAp, the composite was submersed in 5 M sodium hydroxide (30 min) to improve hydrophilicity and washed three times in DI water before testing. Linear regression from 5-30% of the ultimate strain was used to obtain the Young's modulus. The ultimate stress and strain were determined from the global maximum stress, and the yield stress and strain were determined using the 0.2% strain offset. n=5-6.

4.4.4 Three-point bend testing

PCL, PCL-HAp, and PCL-HAp beams were 3D-printed (70x15x3mm) and tested for flexural stiffness following ASTM standard #D790. A span length of 48mm was set on a 3-point bending fitting for the TestResources machine. Beams were deflected at a flexural strain rate of 1%·min^{-1} to 5% flexural strain. The flexural modulus was determined from the slope of the 1-2.5% flexural strain range. Beams were printed on the Cura TAZ 6 Lulzbot 3D-printer. n=6.

4.4.5 Load transmission test

PCL-HAp prostheses with either a thick, 5 mm collar used in the current animal study, or a thin, 3 mm collar prosthesis, were tested for load transmission. Prosthesis fixation was achieved using the top four screw points where only the top half of the prosthesis with the condyle was printed and tested. A load was applied at a rate of 10 lb·min^{-1} to 5 lbs. and held for 1 min. Transmitted load was measured on a FlexiForce load sensor (Tekscan, Norwood, MA), which was preconditioned with a 70 lb$_f$ load for 5 min.

After each data-collection run, a calibration run was performed with an unconstrained condyle. A power law equation was fit to the calibration data to convert signal to transmitted load from the FlexiForce sensor. n=4.

4.4.6 Biofluid transport via capillary rise

Scaffolds from either PCL-HAp, or ePCL-HAp were printed to assess whole blood capillary rise through the porous architecture. A 10x10x3 mm scaffold was printed with a zig-zag pattern and 0.60, 0.85, and 1.10 mm line-distances such that the actual cross-sectional pore sizes were 152 ± 68, 360 ± 140, and 570 ± 240 μm for the 150, 350, and 550 μm groups, respectively. A bath with whole goat blood (Innovative research, Novi, MI) was raised to contact the scaffold. Imaging was captured at 60 fps and a custom MATLAB script was used to process each image and calculate an ensemble average of the blood height. The initial velocity for each sample was calculated from a linear fit to the initial 2 second period of data. n=6-7.

4.4.7 Bone assessment with Micro-CT

At the 6-month completion of the study, each implant was resected *en bloc* along with the TMJ disc and fossa. The specimens were then scanned with a micro-CT system set to 70 kV, and 200 μA (Quantum FX, Perkin Elmer Co, Waltham, MA) with a 30 mm field of view. Each scan was segmented using Seg3D (University of Utah SCI Institute) for implant, screw, and bone materials. A custom MATLAB script was used to register each object in space for consistent viewing perspectives. Renderings of the segmented and registered objects were performed using Autodesk Fusion 360 (San Francisco, CA).

4.4.8 Soft tissue assessment with histology and immunohistochemistry

Resected tissue specimens were fixed in 10% neutral buffered formalin (VWR, Radnor, PA) dissected and imaged for gross morphology. Boney tissues were decalcified in newcomer supply (Newcomer Supply, Fisher, Hampton, NH) for at least 4 months before sectioning with a blade. All tissues were dehydrated in 70% ethanol (VWR, Radnor, PA) overnight and paraffin embedded for slide mounting. Slices 4 μm thick were mounted and staining for hematoxylin and eosin (H&E), or Alcian blue on a ST5020 workstation (Leica, Wetzlar, Germany). Immunostaining was performed with a Leica BOND III BOND RX automatic system (Wetzlar, Germany) with a 12-hour antigen-retrieval step at 60 ˚C at pH 9.0 to prevent bone delamination. Soft tissue specimen antigen retrieval was performed at 100˚C for 20 min at pH 6.0. For collagen II and CD4 immunostaining, rabbit primary antibodies were purchased from Abcam (#ab34712, Cambridge, UK), and Novus (#NBP1-19371SS, St Louis, MO), respectively. For secondary antibody, post-primary IgG-linker reagent with 3,3'-diaminobenzidine tetrahydrochloride (DAB) as chromogen and counter-stained with hematoxylin. Antibody-specific positive and negative control (omission of primary antibody) were parallel stained. Additional positive control tissue for CD4 was obtained from goat submandibular lymph node.

4.4.9 TMJ disc gross morphology scoring

TMJ discs were randomly sorted and scored by four oral surgery clinicians. A scoring system was modified from van den Borne *et al*.[201], with a range from 0 (poor) to 4 (excellent).

4.4.10 Statistical analysis

Statistical analyses were performed with one-way ANOVA with Tukey's post-hoc test, or a one-way t-test for two groups. Significance was defined when α=0.05. All data were mean ± standard deviation.

4.5 Experimental Results

4.5.1 Animals

Five goats were euthanized after 6 months and one euthanized early (4 months) due to conditions unrelated to the study, i.e., a caseous lymphadenitis caused by a *Corynebacterium pseudotuberculosis* infection likely contracted before boarding **(Supplemental Fig. 4.1).** Results were thus reported for three no-hydrogel and two hydrogel group specimens. All animals exhibited weight gain averaging 18 ± 10 lbs. over the study duration and resumed normal jaw function within 2 hours of surgery.

4.5.2 Structural and Mechanical properties of 3D-printed prosthesis

Energy dispersive x-ray spectroscopy (EDS) exhibited a homogeneous distribution of calcium and phosphorous throughout 3D-printed PCL-HAp **(Fig. 4.3)**.

Young's moduli increased by 67% with the addition of HAp relative to PCL PCL-HAp; with no difference after etching **(Fig. 4.4C)**. Strain energies were 1.8-fold higher in PCL than PCL-HAp, and not different between PCL-HAp and ePCL-HAp **(Fig. 4.4D)**. Ultimate tensile stresses and yield stresses did not exhibit differences among groups **(Fig. 4.4E, G)**. Ultimate strains reduced by 0.6-fold from PCL to PCL-HAp, and ePCL-HAp **(Fig 4.4F)**. Furthermore, yield strains were 1.5-fold higher in PCL than in PCL-HAp and ePCL-HAp **(Fig. 4.4 H)**.

Flexural stiffness was 2.06-fold higher in PCL-HAp than the PCL group but did not change after etching **(Fig. 4.5)**.

Load transmission to underlying bone-grip was approximately 12% higher for thin-collared implants than for thick-collar implants that were used in the current study's pilot animal study **(Fig. 4.6)**.

4.5.3 Porous architecture supports whole blood infiltration

For all the NaOH-etched scaffolds, capillary rise of whole blood reached the full 1 cm height within one minute **(Fig. 4.7A)**. Small, 152 ± 68 μm pore length scaffolds exhibited an initial velocity of 3.7 ± 1.2 mm·s^{-1}, and increasing pore sizes reduced the initial velocities by 31% and 77% for 360 ± 140, and 570 ± 240 μm, respectively **(Fig. 4.7B)**. Differences in initial velocity were not exhibited by the etched 150 and 350 μm groups. Non-etched scaffolds exhibited negligible capillary rise **(Fig. 4.7B)**.

4.5.4 Bone growth and resorption surrounding condyle

Bone growth and resorption exhibited by micro-CT-derived renderings were highly variable from specimen to specimen. Resorption was focused to regions directly under the prosthesis condyle and a gap was left between the prosthesis collar and bone **(Fig. 4.8)**. An approximate measurement made on MicroCT images suggested the depth of resorption was lower in the hydrogel group (A: 6.0, B: 5.6, and C: 2.6 mm) than the no-hydrogel group with lengths of D: 7.2 and E: 9.2 mm. Bone growth surrounding the implanted condyle was localized to both the medial and posterior regions of the condyle. In all cases except B, soft tissues enveloped the condyle.

4.5.5 Possible neocartilage in regenerated soft tissue

Sagittal sections of soft tissue enclosing the implanted condyle exhibited signs of neocartilage formation. Positive Alcian blue and collagen II staining was localized to the functional anterior side in non-hydrogel C and hydrogel-integrated D implant **(Fig. 4.9)**. CD4 staining for helper T cells was variable with faint to no stain in the control, B, C, and D to moderate staining in A and E.

4.5.6 TMJ disc histology

Histology of the TMJ discs exhibited highly variable results from perforated, granulation tissue, to nearly pristine **(Fig. 4.10)**. No observable granulation tissue was exhibited by the discs for control, B, C, and E. For B, a central disc perforation was observed. Discs for A and E presented with granulation tissue. For C, the disc histology closely matched that of the unoperated control disc.

4.5.7 TMJ disc gross morphological scoring

Disc scores suggested degeneration, hypertrophy, and irregular macroscopic appearances for discs A, B, and E) **(Table 4.1)**. Though goat B scored 0 for degeneration due to perforation, the macroscopic appearance scored 1.8, higher than discs A (1.3) and E (1.0). Discs A and B scored 30% higher overall than goat E. The disc from goat C scored slightly higher than the average control disc score (4.0 vs. 3.9). It is noteworthy that the disc from goat C appeared longer anteroposteriorly and shorter mediolaterally than the contralateral control disc. No scores could be collected for goat D because the disc fused to the condyle, making it difficult to discern disc tissue from other soft tissues.

4.6 Discussion

The current study demonstrated the feasibility of an acellular, biphasic TMJ prosthesis for immediate loading. The integrated hydrogel prosthesis exhibited variations in gross appearance, and staining of key neocartilage markers. Specifically, one specimen from each group (hydrogel and no-hydrogel) exhibited collagen II and Alcian blue staining. CD4 staining was pronounced in one specimen from each group, and the remaining specimens exhibited little CD4 staining. It is possible that higher inflammation was associated with CD4 staining, though Vapniarsky *et al*.[202], demonstrated animals with chronic inflammation did not exhibit higher levels of CD4 compared to a negative control. All specimens featured fibrous soft tissues throughout the condylar head's porous architecture. Furthermore, the TMJ disc exhibited variable gross appearances and Alcian blue staining, with a nearly pristine disc coming from a hydrogel-free prosthesis. Further studies may examine strategies for TMJ disc management and attachment during implantation. In addition, a more sophisticated, zonal material approach may be warranted to integrate stratified subchondral bone, and layered cartilage structures into a regenerated mandibular condyle. Adjustments to both biochemical (e.g., BMP-2) and physical (e.g., adjusting pore size, loading to bone, and degradation) signaling could be incorporated into the prosthesis design to improve tissue regeneration and reproducibility.

In both hydrogel and no-hydrogel groups, the prosthesis restored chewing function in a human-sized TMJ model. All subjects resumed eating a normal diet and gained weight throughout the study period. Bone responses to the scaffolds, however, were variable with regions of resorption immediately under the prosthesis. The condyles in some cases

appeared to have plastically deformed toward the underlying ramus. Tensile testing revealed that the Young's modulus of PCL was enhanced to 269 MPa by the addition of HAp. For comparison, the compressive modulus of PCL-HAp has been reported in the range of 20 kPa to 150 MPa [203], [204], [205]. Additional bending support in the collar of the prosthesis was enhanced by the HAp with a flexural modulus of 470 MPa [206], [207], [208]. For plastic deformation or failure, strains beyond 3% in the prosthesis collar were likely allowed by resorption of supporting bone.

There are many different sources of signaling for bone maintenance and growth, including mechanical forces to the underlying bone. The mechanical loading regimen most suitable to restore bone remains unclear for the TMJ, though loads of approximately 20 lb_f have been measured in Macau condyles, and 5 lb_f were estimated from a study with humans during normal chewing function [209], [210]. Analysis of joint implants has suggested higher load transmission can prevent stress-shielding and thus improve bone density [211], [212]. In contrast, dental implants may fail to osseointegrate when immediately loaded without a 4-6 month period of load-free conditions [213], [214]. In the current study, we introduced a method with a load sensor to measure transmitted loads. The prosthesis design here transmitted a significant proportion of a 5 lb_f applied load (>80%) to the supporting structure, and yet all subjects exhibited bone loss. In contrast, high stiffness metal TMJ implants rarely exhibited significant bone loss with reports of functional success for over 20 years [215], [216]. A more refined understanding of the types and magnitudes of stresses that encourage bone formation may be important to successful bone regeneration strategies in immediate TMJ loading applications [209], [217], [218], [219]. The load transmission test introduced here may be useful in future work for TMJ prosthesis designs that take bone

mechanotransduction into consideration. Clinical joint immobilization following surgical implantation may be a further consideration for bone integration [220].

Neocartilage formation suggested evidence of a functional environment for cartilage tissue stimulus. Staining for Alcian blue and collagen II was localized to the anterior, functioning surface of a prosthesis that had no hydrogel to provide any chondroinductive cue. The posterior, nonfunctioning surface of the condyle exhibited no Alcian blue or collagen II staining. Furthermore, for the integrated hydrogel case, there were signs of bone formation on the anterior surface, though positive Alcian blue and collagen II was exhibited in a region adjacent to new bone on the anterior surface. These observations were in agreement with the concept of using functional loading to regenerate cartilage tissues [221], [222].

Though it may not be possible to determine cell source for regenerated neocartilage based on staining and morphology from histology, potential tissue sources that could contain progenitor cells were considered based on anatomic proximity. Given the higher numbers of stem cells in bone marrow than blood, adipose, or TMJ, the cell source for regenerated condylar tissues could likely have been bone marrow from the ramus or through systemic circulation [223]. The TMJ disc is a dense collagenous structure, but evidence of vasculature through the TMJ disc could provide transport for some *Chad+* chondrogenic fibroblasts [224], [225]. Future work may be able to develop cell lineage tracking methods to provide compelling evidence for the origins of regenerated tissue [195], [226], [227], [228].

Within the condyle porous architecture, highly aligned fibrous tissues formed, though more time *in vivo* could potentially allow for mineralized tissue formation. The

current study emphasized a capillary rise scaffold design with ~150 μm pore sizes to gain regenerative utility from the native cells located in the adjacent ramus bone marrow. Future work may explore larger, transport-sustaining pore sizes, or other pore geometries to better stimulate osteogenesis throughout the scaffold [229], [230].

The health of the TMJ disc offered signs of functional joint regeneration. Pristine disc structures scored higher than the average control disc throughout the 6-month implantation period. The presence of Alcian blue staining in the disc, though only on the anterior region, suggested a healthy disc structure. Although, other cases here exhibited disc perforation, or granulation tissue, and potential signs of fibrous ankylosis with disc fusion to the condyle. Tissue-scale pathogenesis of ankylosis in TMJ and other joints warrants further investigation [231], [232], [233], [234], [235].

The current study had certain limitations. Additional timepoints with CT scans would be helpful for characterizing prosthesis deformation, or identifying locations where bone changes initiated. The structural integrity of the condyle was only examined after resection and may not provide an accurate reflection of *in vivo* relationships between TMJ structures. Though a biphasic scaffold was developed, only a bulk hydrogel was used here. Regenerating zonal cartilage architectures remains a goal for TMJ tissue engineering, though progress has been made with a bioreactor approach [195]. Hypothesis testing was not available due to the limited number of animals in this pilot study. Any comparisons from the *in vivo* results were thus suggested trends only rather than scientific conclusions. A larger number of animals (n=6) could allow for hypothesis testing and statistical analysis for future investigations beyond this pilot study.

4.7 Conclusions

The results of the current pilot study suggested improving bone continuity with the scaffold is a major goal for acellular TMJ condylar tissue engineering, which may require future efforts to consider cell seeding in the operating room and/or addition of biologic signals. An additional goal remains improving cartilage regeneration with an integrated and layered structure like that of native condylar cartilage. Design features for resorbable scaffolds that could improve bone regeneration include adjustments to the porous architecture, load transmission profile, degradation rate, and use of biochemical signaling from growth factors (e.g., BMP-2) or peptides.

Chapter 5: Interface Performance Enhancement in 3D-Printed Biphasic Scaffolds with Interlocking Hourglass Geometry[4]

5.1 Abstract

The cartilaginous surfaces in ginglymus (hinge) joints such as the knee, elbow, and the ginglymoarthrodial temporomandibular joint (TMJ) primarily function under unidirectional shear and orthogonal compression. Regenerative medicine approaches to treat injured or arthritic joints include biphasic scaffolds, which must withstand the joint's biomechanical demands. In the current study, we leveraged computational modeling and empirical testing to design a 3D-printed biphasic scaffold with enhanced biomechanical performance. A sinusoidal hourglass tube geometry was introduced to support shear stresses at the interface and to support orthogonal compression. Biphasic constructs were evaluated with both empirical and *in silico* interface shear experiments. A thermal extrusion 3D-printed polylactic acid (PLA) hourglass interface was infilled with a hydrogel, comprised of either (1) agarose, or (2) pentenoate-modified hyaluronic acid (PHA), polyethylene glycol diacrylate (PEGDA), and devitalized cartilage (DVC). Shear loads were applied either parallel to the tube's long axis (i.e., 1-direction) or orthogonally (i.e., 2-direction). Additionally, the hourglass tube architecture was evaluated in compression in the 1- and 3-directions.

---

[4] In the process of submission to: Annals of Biomedical Engineering.

Empirically, ultimate interface shear stresses up to 51 ± 7 kPa were observed for the infilled PHA-PEGDA-DVC hydrogels, with higher values in both loading directions compared to a crosshatch scaffold ($p < 0.05$). The computer model suggested a geometry-dependent shear load-transfer. The ultimate compressive stress for the hourglass architecture in the 3-direction reached 6.9 ± 1.8 MPa, which was 39% higher than the crosshatch architecture. The hourglass design enhanced performance under shear in the 1-direction and compression in the 3-direction, which may add value for future designs employed for regenerating tissue in ginglymus joints that primarily function under unidirectional shear and orthogonal compression.

5.2 Introduction

Osteoarthritis is a highly prevalent disease that results in damage to joint tissues and in joint pain [35], [236], [237], [238]. Osteoarthritis may severely degrade the osteochondral unit, which is comprised of cartilage and bone [239]. Surgical treatment of osteoarthritis or other cartilage injuries may be performed on the ginglymoarthrodial temporomandibular joint (TMJ) or other ginglymus joints such as the knee or elbow [185]. Limitations to existing treatments for osteoarthritis and other joint injuries have inspired the development of tissue engineered scaffolds to repair and regenerate osteochondral tissues.

Tissue engineering scaffolds provide a regenerative approach, with different layers to regenerate cartilage and bone, i.e., biphasic scaffolds [30], [240], [241]. Biphasic scaffolds face challenges including integration with the surrounding tissue, or incongruent surface repairs, which may lead to stress concentrations and scaffold loosening [242], [243]. After implantation, biphasic scaffolds experience a biomechanical challenge from the joint's opposing surface. Ginglymus (i.e., hinge) joint function primarily introduces shear stresses to the scaffold in one direction and compression to the scaffold in the orthogonal direction. Without sufficient reinforcement, these shear and compression loads may result in mechanical failure and poor tissue repair [244]. For example, the mandibular condylar of the TMJ is loaded with superoinferior compression and with anteroposterior shear. Thus, there is a biomechanical challenge to create biphasic scaffolds with a strong interface capable of supporting physiologic loads.

In the current study, we evaluated a biphasic scaffold with the overall goal of enhancing biomechanical performance. Representing the 'bone' region, a 3D-printed structure was fabricated, with an hourglass microarchitecture that we introduced. The 'cartilage' region was represented with an infilled hydrogel. The specific biomechanical goals were to create a 3D-printed biphasic scaffold with superior interface integration under shear loads and enhanced support of orthogonal compression. The scaffold design was transversely isotropic, i.e., exhibiting symmetry in two dimensions. The unique direction of the hourglass structure was aligned with the long axis defined here as the 1-direction. It is noteworthy that the 2- and 3-directions of the hourglass geometry were symmetric, acknowledging that varying the spacing between the tubes would produce a fully anisotropic structure. Thus, the hourglass structure was designed to support the TMJ mandibular condyle's anteroposterior shear (i.e., 1-direction), and superoinferior compression (i.e., 3-direction). The hourglass tube design drew inspiration from undulating steel rods used to reinforce concrete buildings. In addition, the hourglass tube introduces an arch to spread out stresses analogous to a stone arch bridge. Thus, we hypothesized that a mechanically interlocking hourglass pattern would enhance, relative to a typical crosshatch pattern with similar porosity, the apparent performance of the scaffold under shear loads in the 1-direction and under compression loads in the 3-direction.

Biomechanical considerations are not always included in the outcome analyses of osteochondral tissue engineering research, or if present, may be focused on evaluating the individual mechanical properties of the scaffold's biomaterials separately [83], [245], [246], [247]. Although much progress has been made in enhancing the biomechanics of biphasic scaffolds, studies often rely on compression tests without accounting for the

complex loading environment in joints. Some investigations have evaluated interface performance under shear loads, although testing methodologies have not been consistent [85], [86], [89], [108].

For example, a lap shear test was performed to evaluate interface performance of tissue engineered constructs fabricated with *in vitro* tissue culture cell sheets on porous hydroxyapatite [248]. In a different example, an interface shear test was performed on a biphasic scaffold to determine the effect that different substrate pore areas had on interface strength [33]. The consistent interface shear test results and accessible sample preparation in the latter study inspired the current study to pursue interface shear testing.

The current study evaluated the interface of biphasic scaffolds with an interface shear test performed in the 1- or 2-directions, and additionally submitted the hourglass architecture to compressive loads in the 1- and 3-directions. The purpose of designing samples with a 2 mm lip of hydrogel material was to enable the interface shear test to be conducted, allowing reproducible evaluation of the ultimate interface shear stresses.

Several investigations have examined how scaffold interface geometries may support interface shear in osteochondral tissue engineering. Porous crosshatch architectures with parallel lines deposited in alternating 0 and 90° directions have been investigated with a variety of strut spacings for osteochondral scaffolds. However, one study exhibited no differences in interface shear stress between a crosshatch pattern and a smooth control [107]. In contrast, other studies have demonstrated enhanced interface strength with a porous interface. For example, a 3-fold improvement in interface shear strength was exhibited by a porous scaffold compared to a smooth surface [33]. In another study, over 6.5-fold improvements were exhibited by a porous, interlocking scaffold

compared to a smooth surface [108]. The contrasting interface performance in previous studies inspired the current work to further investigate potential interface shear strength enhancement from the interface geometry [33], [89], [108]. The porous crosshatch design has been tested in many previous investigations of scaffold mechanical performance [70], [72], [79], [109], [204], [249], [250], [251], and thus provided a common point of reference for comparing the performance of a novel interface geometry. In addition to interface shear, the compressive behavior is important to scaffold success after implantation. Many other microarchitectures, e.g., a diamond [252], gyroid [144], Voronoi network [253], or honeycomb [144] architecture have additionally been evaluated in compression [252], [254], [255], [256] [257].

The purpose of the study was to evaluate the 1) anisotropic compressive stiffness and strength of a polylactic acid (PLA) scaffold based on either the hourglass architecture or a standard crosshatch architecture, and 2) anisotropic shear stiffness and strength of two different hydrogels in the PLA scaffolds. In addition, a computer model of the interface shear test was developed to analyze the stress. For the shear evaluation, we 3D-printed the PLA scaffold and infilled it with either an agarose hydrogel or a cartilage-matrix hydrogel for empirical testing. The rationale for the 5% agarose hydrogel was for rapid fabrication and screening before submitting the design to further evaluation with the next hydrogel. The rationale for the 4% pentenoate-modified hyaluronic acid, 20% polyethylene glycol diacrylate, and 5% devitalized cartilage hydrogel was its previous use in our recently published TMJ mandibular condyle regeneration study [31], [32].

5.3 Materials and methods

5.3.1 Materials

All materials were purchased from Sigma-Aldrich (St. Louis, MO) unless stated otherwise.

5.3.6 Hourglass Design

Hourglass interface features were digitally designed with a custom MATLAB script using the following sinusoidal wave function for the hourglass tube radius, r.

$$r = \frac{1}{4}\left[D + d + (D - d)\cos\left(\frac{2\pi x}{\lambda}\right)\right] \qquad (Eq.\ 5.1)$$

x was the length, which varied along the tube's longitudinal axis. Four design parameters were used to define the interlocking substrate geometry: (1) Maximum diameter, D, (2) minimum diameter, d, (3) node-node length, λ, and (4) the maximum angle that subtends the long axis of the hourglass tube, θ, calculated from a given parameter set (**Fig. 5.1A**).

$$\theta = tan^{-1}\left[\frac{dr}{dx}\right] at\ x = 0.75\lambda \qquad (Eq.\ 5.2)$$

Where

$$\frac{dr}{dx} = -\frac{0.5\pi}{\lambda}(D - d)sin\left(\frac{2\pi x}{\lambda}\right) \qquad (Eq.\ 5.3)$$

The hourglass tube radius was revolved about the tube's long axis with a cylinder function from the GibbonCode library [258] to create the 3-dimensional hourglass tube.

For a selected θ, the minimum diameter was determined by solving Eqs. 5.2 and 5.3 for d (Eq 5.4), with the remaining variables (i.e., D, λ) held constant.

$$d = D - \frac{2\lambda}{\pi}tan\ \theta \qquad (Eq.\ 5.4)$$

Hourglass tubes were arranged such that there was 0.2 mm overlap in the 2- and 3-directions with the adjacent tubes, creating a transversely isotropic geometry. Thus, the structure exhibited symmetry along the 2- and 3-directions with the 1-direction aligned with the tube's longitudinal axis.

5.3.2 Interface Shear Computational Model

A computer model was generated to evaluate surface shear loading of the hydrogel integrated with a rigid hourglass interface structure. The hourglass tube was generated with a cubic hydrogel region spanning 1 mm beyond the tube diameter on the sides in the 2-direction, 0.2 mm below the tube in the 3-direction, and a height that was 2 mm above the tube (**Fig. 5.1B**). The hydrogel was 10 mm in length along the 1-direction, equal in length to the hourglass tube.

The dimensions of the design were defined such that the 1-direction was along the tube's long axis. For stress analysis and computer modeling, the 1-, 2-, and 3-directions were consistent with the x-, y-, and z-directions, respectively.

An interface shear computer model was generated for 10 different hourglass geometries ranging from $\theta = 7°$ to $52°$ infilled with a cartilage-matrix hydrogel (**Fig. 5.1B**).

The model geometries were generated with a custom MATLAB script that used the GibbonCode library to generate a 10-noded tetrahedra volume mesh ($\sim$3 elements $\cdot$ mm^{-1}) and to assign boundary conditions [258]. The interface shear stresses were then solved with the finite element method in the FEBio software environment [259]. The hourglass tubes were generated with a cosine wave, where d, D and node-node distance, λ were varied to define the amplitude and wavelength. The θ angle was then calculated . An Ogden model

was assigned as the hydrogel's constitutive relation in the computer model according to the following equation for stress, σ, as we previously described [31].

$$\sigma = \mu\left(\lambda^{\alpha-1} - \lambda^{-\frac{\alpha}{2}-1}\right) \qquad \text{(Eq. 5.5)}$$

Where μ is a coefficient related to the classical shear modulus, μ_0, as

$$\mu_0 = \frac{\mu\alpha}{2} \qquad \textit{(Eq. 5.6)}$$

$\mu_0 = \mu\alpha/2$, λ is the stretch ratio (ranges from 0 to 1 for compression), and α is the nonlinear parameter. By convention σ < 0 for compression. The stiff hourglass tube was assigned as a rigid body.

The hydrogel's outer surfaces were assigned unconstrained boundary conditions except for the 3-direction at the top surface. To simulate the empirical setup with the top-constraining portion of the crosshead, the top surface was constrained in the 3-direction, but allowed to move in the 1- and 2- directions. The hourglass tube was fixed in space and the boundary nodes between the tube and hydrogel were assigned a sliding contact. A 0.07 mm prescribed displacement was applied to a 2 mm tall region of the hydrogel side wall above the tube. For 1-direction shear test models, displacement was prescribed in the 1-direction, and for 2-direction tests, displacement was prescribed in the 2-direction.

Interface stress analysis was performed on the FEBio output using MATLAB. The apparent interface shear modulus was determined with a linear fit to the model's interface stress and nominal strain. To analyze the interface stress distribution along the tube, a radial region of interest that extended 0.5 mm beyond the hourglass tube surface was defined for a series of 2-3-plane cross-sections along the 1-direction of the mesh. The maximum 1st principal stress (tensile stress) and minimum 3rd principal stress (compressive stress) were

plotted with respect to the tube's long axis in the 1-direction. The stress-effects of the hourglass tube shape were determined by varying the hourglass angle, θ, along with the minimum diameter.

5.3.3 PHA synthesis and Nuclear Magnetic Resonance (NMR) characterization

Pentenoate-modified hyaluronic acid (PHA) was synthesized from 1.5 MDa hyaluronic acid (HA, Lifecore Biomedical, Chaska, MN) as previously described [166]. Briefly, HA was dissolved (0.5% w/v) in deionized (DI) water and dimethylformamide (DMF) at a 3:2 water to DMF ratio. 4-dimethylaminopyridine was added at 0.25 g per g of HA. 4-pentenoic anhydride was added at a 10-fold molar excess to HA. The pH was maintained between 8-9 using 4M NaOH to allow the functionalization reaction to form PHA. PHA was precipitated after reacting overnight, then centrifuged, with the acetone supernatant being discarded. Dialysis was performed for 48 h (MWCO: 6-8 kDa, VWR, Radnor, VA) to purify PHA dissolved in DI water. The PHA solution was freeze-dried on a FreeZone 6 Plus lyophilizer (Labconco, Kansas City, MO, USA) before storage at -20 ˚C.

NMR characterization of PHA for degree of substitution was performed as previously described [166]. Scans were performed using a Varian VNMRS-500 MHz NMR Spectrometer (Palo Alto, CA) at -80 ˚C. Of the repeating disaccharide units, 40% were functionalized with pentenoate groups in the current study.

5.3.4 DVC processing

Cartilage was harvested from porcine knees (Hampshire and Berkshire, female, 1 year old, 180-220 kg) obtained from a local abattoir and stored at -20˚C. The cartilage was coarse-ground with a coffee grinder (Kitchen Aid, Benton Harbor, MI, USA) and cryoground into a powder as previously described [167] using a SPEX 6770 Freezer/Mill (SPEX SamplePrep, Metuchen, NJ, USA). The DVC powder was then lyophilized and stored at -20 ˚C.

5.3.5 Hydrogel preparation and crosslinking

For cartilage-matrix hydrogels, the PHA concentration was 4% w/v, polyethylene glycol diacrylate (PEGDA) (4 kDa) was 20% w/v, and DVC was 5% w/v. These PHA-PEGDA-DVC hydrogels were prepared as previously described [31]. PHA and DVC were reconstituted together in phosphate buffered saline (PBS), and PEGDA was reconstituted separately in PBS before combining. The crosslinker and photoinitiator were mixed with PEGDA and PBS before combining with PHA and DVC. Once the PEGDA was fully dissolved, a photoinitiator, 6.5% w/v lithium phenyl-2,4,6-trimethylbenzoylphosphinate (LAP; 98%; TCL0290-1G) (TCI America; Portland, OR, USA), and crosslinker, 3% w/v dithiothreitol (DTT), were prepared in the remaining phosphate buffered saline (PBS) to ensure a 1:1 thiol:ene molar ratio for all composites. Precursor mixtures were spatulated for at least 5 min prior to backloading into a syringe for application. Hydrogels were photocrosslinked with a 365 nm light at 1280 μW $\cdot$ cm^{-2} for 10 min (EA-160, Spectroline, Westbury, NY).

Additionally, agarose hydrogels were prepared by mixing 5% w/v agarose (cat# A9539) with PBS, microwaving for 10 s (microwave brand) and centrifuging at 600 g for 5 s to remove air bubbles.

5.3.7 3D-Printing

The hourglass substrate was 3D-printed from polylactic acid (PRO Series PLA, MatterHackers, Lake Forest, CA) on a commercially available 3D printer (AnkerMake M5, Anker Innovations Co., Ltd., Changsha, Hunan, P.R. China). The print temperature was 200 °C, and the build plate temperature was 60 °C. The layer height was 0.2 mm, and the line width was 0.4 mm. The print speed was 250 mm $\cdot$ s^{-1}. The hourglass feature infill density was 100% with a concentric pattern. For interface testing, the base was the crosshatch pattern with layers oriented 90° from each other and a line distance of 1 mm.

5.3.8 Interface shear test specimen preparation

Three different hourglass interface groups were 3D-printed with $\theta = 20°$, $\theta = 30°$, and $\theta = 40°$, while holding constant D = 3.5 mm, λ = 5 mm, and calculating d as 2.4, 1.7, and 0.8 mm, respectively. The specimen dimensions that were fabricated for interface shear tests were 10 x 10 x 10 mm^3 with substrate, interface, and hydrogel layers. The hourglass interface substrates were 3D-printed from PLA with 1 layer of 3 hourglass tubes that were oriented side-by-side with a 0.2 mm side-by-side overlap in the 2-direction. The single layer of hourglass tubes was printed on a rectangular base, with a 0.2 mm overlap in the 3-direction between the tubes and the base. The rectangular base was printed as a porous crosshatch architecture. Biphasic specimens were prepared by infilling the hourglass samples with a hydrogel using a 3D-printed well such that the hydrogel extended 2 mm

above the substrate. The well was removed after the agarose solidified. Either 5% agarose or 4% PHA, 20% PEGDA, 5% DVC hydrogels were infilled. The 10 x 10 x 10 mm^3 samples were thus layered with a hydrogel for the top 2 mm, an interlocking interface that was 3.5 mm thick, and a 4.5 mm thick, porous base (**Fig. 5.1C**). For comparison, a smooth control group was an 8 mm tall smooth solid base with a 2 mm tall hydrogel filled on top. A crosshatch group had an 8 mm tall porous base infilled with a hydrogel such that the biphasic specimens were 10 x 10 x 10 mm^3.

Either agarose or PHA-PEGDA-DVC hydrogels were infilled into the substrate using a well-casting technique [248], [260]. Casting wells were 3D-printed from PLA and lubricated with vacuum grease (88693 silicone grease, Danco Inc., Irving, TX), placed on a glass microscope slide, and filled with the hydrogel precursor (i.e., either agarose or PHA-PEGDA-DVC). Then, the hourglass substrates were turned to face the hydrogel and press-fit into the hydrogel-filled wells such that the hydrogel thickness was 2 mm beyond the surface hourglass features. For agarose, the precursor was allowed to cool to room temperature for 10 min after microwaving before the biphasic construct was removed from the well. For PHA-PEGDA-DVC hydrogels, the precursor was light-cured through the glass slide for 10 min. Further light curing was performed for 5 min on each side perpendicular to the top after removing the sample from the well.

Biphasic samples were thus created with agarose for testing the interface behavior for five groups: (1) Smooth surface control, (2) cross hatch, (3) $\theta = 20°$, (4), $\theta = 30°$, and (5) $\theta = 40°$. These five agarose groups were evaluated with interface shear tests in both the 1-direction (parallel with the tube's long axis) and 2-directions. The PHA-PEGDA-DVC

hydrogels were evaluated afterward, with a screened subset of groups evaluated with interface shear tests, specifically only the smooth surface, crosshatch, and $\theta = 40°$ groups.

5.3.8 Interface shear testing

A custom L-shaped grip for the interface shear test was designed in SolidWorks (Dassault Systèmes, Vélizy-Villacoublay, France) and 3D-printed from PLA. Specimens (n = 6) were mounted in the grip and positioned using a screw such that the top surface of the hydrogel lightly contacted the L-shaped crosshead (**Fig. 5.1C**). The L-shaped crosshead was then moved laterally across the interface specimen surface until the 2 mm tall wall of the crosshead contacted the hydrogel, generating interface shear loading. A tare load of 0.1 N was applied and then the test was performed at $1 \text{ mm} \cdot \text{min}^{-1}$ (i.e., strain rate = 0.167 % $\cdot \text{ s}^{-1}$) until failure, which was defined by the peak stress after which the load decreased. The shear stress was calculated by dividing the reaction force by the specimen's original top surface area. Nominal strains were calculated using displacement along the loading direction and a gauge length consistent with the specimen length along the loading direction. The apparent interface shear modulus was calculated using a linear fit to the 2.5-5% strain range of the stress/strain plot. The hourglass interface structure was 3D-printed with PLA, and the hydrogel was infilled with either 5% agarose, or PHA-PEGDA-DVC hydrogels made as described earlier.

5.3.7 Hourglass infill architecture compression testing

An hourglass infill architecture was 3D-printed from PLA by arranging $\theta = 40°$ hourglass tubes side-by-side with a 0.2 mm overlap in the 2- and 3-directions to build 10 x 10 x 10 mm^3 sample for compression testing. The resulting structure was comprised of 3

layers of hourglass tubes with each layer made up of 3 tubes arranged side-by-side such that the structure exhibited transverse isotropy with symmetry in the 2- and 3-directions (**Fig. 5.1D**). For comparison, a crosshatch architecture was 3D-printed with a similar porosity to the hourglass architecture. We note that the crosshatch architecture is likewise transversely isotropic, but with symmetry in the 1- and 2-directions. Therefore, for each architecture, the 1- and 3-directions were not symmetric with each other in structure.

Samples from the hourglass and crosshatch groups (n = 6) were weighed to calculate porosity [261], [262] using a PLA density of 1.25 g · cm^3. Compression testing was performed in the 1- or 3-direction with a uniaxial tester (TestResources, Shakopee, MN). The 2-direction was not evaluated because each architecture had a plane of isotropy with another direction (i.e., with the 1-direction for the crosshatch group, and with the 3-direction for the hourglass group). A tare load of 10 N was applied and samples were compressed at a rate of 1 mm · min^{-1} (strain rate = 0.167 % · s^{-1}) until failure, which was defined as the peak stress after which the stress decreased. The compressive modulus was calculated as the slope of a linear fit to the initial 0-2% strain range to approximate the stiffness of the sample from the initial deformation in the stress/strain plot. Ultimate stress and failure strains were derived from the maximum stress. The energy at failure was calculated as the area under the stress/strain plot up to failure.

5.3.8 Statistical Analysis

GraphPad Prism version 10.1.1 (GraphPad Software, San Diego, CA, USA) was employed to perform all statistical analyses. A one-way analysis of variance (ANOVA) test with Tukey's honestly significant difference post-hoc test was employed to compare

multiple groups. The significance level was α = 0.05. All results were reported as mean ±

standard deviation.

5.4 Results

5.4.1 Interface shear computer model validation

The apparent interface shear moduli from the computer simulation provided a

reasonable comparison with the empirical data when using the hydrogel constitutive

relation from compression testing (**Fig. 5.2A**). The model's apparent interface shear moduli

for the $\theta = 40°$ hourglass were slightly lower than those of the experiments in both the 1-

and 2-direction, but nearly within one standard deviation (**Fig. 5.2A**). A series of 20

different simulations with different hourglass angles from 7° to 52° exhibited increasing

apparent shear moduli from ~8 to 200 kPa, respectively, in the 1-direction (**Fig. 5.2B**). For

the 2-direction, however, the apparent shear modulus exhibited an inverse relationship that

decreased with increasing angle θ from 250 kPa to 180 kPa for $\theta = 7°$ and 50°, respectively.

The apparent interface shear modulus exhibited intersecting values of 190 kPa for the 1-

and 2-directions at $\theta \sim 40°$ (**Fig. 5.2B**).

5.4.2 Hourglass interface stress analysis

The computer model was leveraged to examine stress distributions inside the

hydrogel space infilled around the hourglass geometry. The principal stresses in 3

dimensions are defined from largest to smallest as 1st, 2nd, and 3rd, respectively. Thus, in

the finite element model's output, the maximum 1st principal stress represents the

maximum tensile stress (i.e., positive value), and similarly the minimum 3rd principal stress

represents maximum compressive stress (i.e., negative value) [259].

The 3rd principal stress increased in magnitude as the angle θ increased for the hourglass tube groups (**Fig. 5.3A-C**). Stress concentrations were located near the interface of the hourglass's upsloping feature (**Fig. 5.3B, C**). In the interface region, with increasing θ, the stress concentration exhibited a shift in location from the left side to the central portion of the hourglass tube (**Fig. 5.3E-G**, and **Fig. 5.3H-J**). The lefthand area of the maximum first principal stress decreased from 70% down to 51% as θ went from 7 to 44°. The central region exhibited increases in 1st principal stress from 26% to 42% with increasing θ. Similarly, the 3rd principal stress magnitude decreased from 79% to 53% for the left side with increasing θ (**Fig. 5.3H-J**). And the central region exhibited an increase in 3rd principal stress magnitude from 19% to 44% as θ increased (**Fig. 5.3H-J**). It is noteworthy that the maximum 1st principal stress of 15 kPa did not increase from $\theta = 25°$ to 44° as much as the 3rd principal stress magnitude did, from ~15 to 35 kPa for $\theta = 25°$ to 44°, respectively.

5.4.3 Hourglass interface shear performance with agarose

Interface shear tests exhibited enhanced interface performance for specimens with $\theta = 20°$, 30°, and 40° hourglass structures infilled with 5% agarose (**Fig. 5.4**). Representative plots of the interface shear stress vs. nominal strain exhibited linear behavior in both the 1- and 2-directions (**Fig. 5.4A, B**). All the hourglass groups and the crosshatch scaffold exhibited enhanced interface shear performance compared to the control smooth surface in both the 1- and 2-directions ($p < 0.05$, **Fig. 5.4C-J**). Therefore, the following comparisons do not include the control smooth surface, focusing on comparisons among the hourglass groups and the crosshatch group.

For the 1-direction, the apparent interface shear modulus did not differ among the hourglass groups and the traditional crosshatch interface group (**Fig. 5.4C**). For the $\theta = 30°$ in the 2-direction, the modulus was 27% lower than the crosshatch ($p < 0.05$), but the other hourglass groups did not exhibit significant differences from each other or from the crosshatch group (**Fig. 5.4D**).

With regard to the failure properties, the ultimate strains for all three hourglass groups in the 1-direction were 33 to 54% ($p < 0.05$) higher than the crosshatch (**Fig. 5.4E**). The $\theta = 40°$ hourglass interface exhibited a 49% higher failure strain compared to the crosshatch, and a 12-fold higher failure strain compared to the smooth control (**Fig. 5.4E**). For the 2-direction, ultimate strains did not exhibit significant differences among any of the hourglass groups and the crosshatch group (**Fig. 5.4F**).

The ultimate interface shear stress in the 1-direction revealed superior performance of the $\theta = 40°$ hourglass group. Specifically, the $\theta = 40°$ hourglass group ultimate stress was 50% higher than for the crosshatch group ($p < 0.05$). (**Fig. 5.4G**). The $\theta = 40°$ hourglass group ultimate stress was additionally 39% higher than the 20° hourglass group ($p < 0.05$). The ultimate interface shear stress of the 30° hourglass group was not significantly different from those of the crosshatch group or the other hourglass groups. The $\theta = 40°$ group additionally exhibited a 29% higher ultimate interface shear stress than the crosshatch group in the 2-direction (**Fig. 5.4H**). The 2-direction $\theta = 40°$ ultimate interface shear stress of 27 kPa was 47% higher than $\theta = 30°$, and 41% higher than the 20° hourglass interface ($p < 0.05$, **Fig. 5.4H**).

The energy to failure in the 1-direction again revealed superior performance of the 40° hourglass group. In fact, both the 40° and 30° hourglass groups had higher energies to

failure than the crosshatch group, being 2-fold higher ($p < 0.05$) and 50% higher ($p < 0.05$), respectively **(Fig. 5.4I)**. In contrast to the 1-direction, no significant differences in energy to failure were exhibited among the hourglass groups and the crosshatch group in the 2-direction (**Fig. 5.4J**).

5.4.4 The hourglass interface enhanced shear performance with cartilage-matrix hydrogels

Based on the superior performance in material failure properties of the 40° hourglass group with agarose, the 40° hourglass shape was selected to move forward for evaluation with the cartilage matrix hydrogel. Therefore, interface shear tests were performed again with a cartilage matrix hydrogel using the 40° hourglass interface in both 1- and 2-directions. When infilled with the PHA-PEGDA-DVC hydrogel, the apparent interface shear moduli did not exhibit significant differences among the groups in the 1-direction. However, the 40° hourglass structure in the 1-direction demonstrated superior failure properties, with 54% higher ultimate interface shear stress, 49% higher nominal strain at failure, and 2.2-fold higher energy to failure than the crosshatch group, respectively ($p < 0.05$, **Fig. 5.5 B-D**).

For the 2-direction, the 40° hourglass group exhibited a 25% higher ultimate interface shear stress, a 29% higher nominal strain at failure, and a 56% higher strain energy at failure than the crosshatch group ($p < 0.05$). The hourglass structure interface performance was more enhanced under loading in the 1-direction than the 2-direction, revealing anisotropic failure properties.

Comparing the two different hydrogels, it is noteworthy that the ultimate interface shear stress and energy to failure with the crosshatch structure using PHA-PEGDA-DVC were 50% higher and 2-fold higher than with agarose, respectively.

5.4.5 Porous hourglass infill architecture supports compressive loads

The 40° hourglass and crosshatch groups under compression both exhibited anisotropy, with differences in properties for each group between the 1-direction and 3-direction. Representative plots demonstrated an approximately linear stress strain relationship (**Fig. 5.6A, B**). The 40° hourglass group exhibited a $67 \pm 1\%$ porosity, only 5% different from the crosshatch group porosity of $72 \pm 1\%$ ($p < 0.05$). There were no significant differences in compressive moduli among the different architectures or loading directions (**Fig. 5.6C**).

The failure strains for both the crosshatch and $\theta = 40°$ hourglass groups were higher in the 3-direction than in the 1-direction. Specifically, the crosshatch groups exhibited a 4.3-fold higher failure strain in the 3-direction than the 1-direction ($p < 0.05$). The hourglass groups exhibited a 1.96-fold higher failure strain in the 3-direction than the 1-direction ($p < 0.05$, **Fig. 5.6D**). The failure strains in the 1-direction were 7.1% and 6.9%, respectively, for the hourglass and crosshatch groups (no significant difference). However, in the 3-direction, the crosshatch group had the highest overall failure strain, which was 2.0-fold higher than the failure strain of the hourglass group ($p < 0.05$).

The ultimate stresses for the crosshatch and the hourglass scaffolds were 2.1-fold and 1.2-fold higher in the 3-direction than in the 1-direction, respectively ($p < 0.05$).

In addition, the ultimate stress was higher for the hourglass group compared to the crosshatch group in both directions. Specifically, the ultimate stress for the hourglass group was 45% higher than the crosshatch group ultimate stress of 2.15 MPa in the 3-direction, and 53% higher than the crosshatch 4.48 MPa in the 1-direction ($p < 0.05$, **Fig. 5.6E**).

The energy at failure in the 3-direction was nearly 50% higher for the crosshatch group than for the 40˚ hourglass group. However, the 40˚ hourglass group in that 3-direction exhibited a higher energy to failure than either the crosshatch or the hourglass structure loaded in the 1-direction ($p < 0.05$, **Fig. 5.6F**).

5.5 Discussion

In the current study, we introduced a novel hourglass scaffold architecture that exhibited enhanced interface performance when infilled with a tissue engineering cartilage-matrix hydrogel. Furthermore, the hourglass architecture provided compressive strength benefits when employed as a repeating scaffold architectural pattern. The evidence suggested that the hourglass structure is valuable for hinge joint applications where the physiologic loading has both shear and compressive factors. Because the hourglass structure was anisotropic and exhibited superior interface performance in the 1-direction (i.e. aligned with the hourglass tube), and superior compressive performance in the 3-direction, the preferred orientation for applications to the TMJ mandibular condyle, for example, is with the tubes aligned with the anteroposterior direction of loading. Thus, the additional interface strength in the 1-direction and the enhanced compressive strength the hourglass structure exhibited in the 3-direction is leveraged to support compressive loads in the TMJ mandibular condyle.

A major goal of this study was to 3D-print a biphasic scaffold infilled with a cartilage-matrix hydrogel, with an interlocking interface to enhance the interfacial shear strength between the bone and cartilage scaffold phases. With supporting evidence from the computer model stress analysis, and empirical testing with agarose, hourglass tubes with $\theta = 40°$ hourglass were selected for interface shear tests with the cartilage-matrix hydrogel. 3D-printed hourglass interface structures were successfully infilled with either PHA-PEDGA-DVC or agarose hydrogels resulting in a 3-layered scaffold (i.e., osteal microarchitecture, interface region, and chondral phase). Furthermore, the cross-sectional imaging in Figure 5.4 highlighted how the infill method resulted in a hydrogel that was integrated with the hourglass interface (**Fig. 5.4**).

Interface strengths for osteochondral scaffolds have been previously measured with interface shear tests [107], [108], [248], [263]. The current study used an interface shear test to evaluate the effects of interface geometry on interface integration. For comparison, when Zhang *et al.* [263] introduced a porous geometry, an interface shear stress test was employed to collect stress data that was 3-fold higher than a smooth control. The difference in ultimate shear stress between the previous study's 340 kPa ultimate interface shear stress and the current study's 51 kPa was related to different material choices. The previous study employed polyethylene glycol, and β-tricalcium phosphate (PEG/β-TCP) osteochondral scaffold by 3D-printing a PEG hydrogel via stereolithography within the pore area of β-TCP bone matrix. Whereas the current study used a cartilage-matrix hydrogel with chondrogenic potential. The PHA-PEGDA-DVC cartilage matrix hydrogel infilled crosshatch group exhibited interface strengths of 33 kPa (**Fig. 5.5C**) that were 56% higher than agarose infill crosshatch scaffolds (**Fig. 5.4G**). In a different study, Choe *et al.*[107]

prepared a bioprinted osteochondral scaffold with an interdigitating pattern of PCL and PEGDA. The interface shear strength was 64 kPa, which was not significantly different from a control smooth PCL (66 kPa). The current study, however, demonstrated that the hourglass geometry enhanced the ultimate interface shear stress by 54% over a crosshatch design. The previous studies, in addition to the current study provided evidence that modifying the interface geometry was beneficial to enhancing the interface performance.

Adhesive failure was not considered in the current model, and was not observed in the experiments, but with high toughness hydrogels capable of supporting greater compressive stresses than those that are currently available, adhesive failure may contribute to failure at the hourglass interface.

Differences in hydrogel cohesive strength could have been relevant to the different shear strengths in agarose compared to PHA-PEGDA-DVC. Agarose was previously shown to exhibit an ultimate compressive stress of 2.5-100 kPa, compared to the 49-200 kPa bulk yield stress reported for PEGDA [176], [264], [265]. PHA-PEGDA-DVC exhibited an ultimate compressive strength of ~350 kPa in a previous study [31]. Therefore, the higher ultimate shear stress in interface tests with PHA-PEGDA-DVC were consistent with the previously performed compressive strength testing when compared with agarose. Multimaterial formulations have demonstrated success strengthening agarose, and other hydrogels that could be useful for further development of osteochondral scaffolds [31], [176], [265].

One of the benefits of the hourglass approach is that it is amenable to modular advances in hydrogel-based tissue engineering. It may be possible to integrate richly chondrogenic hydrogels with the hourglass base as new advances in translational medicine

are achieved in future studies. Although the current study used a single material to print the scaffold, other studies have used a hybrid approach alternating cell-laden hydrogels and synthetic polymers for structural reinforce to print the two phases [266]. Nevertheless, the current study provided evidence of strong adhesion between the infilled hydrogel and the base hourglass scaffold suggesting that the infill strategy employed here could be advantageous for future joint regeneration applications. As mentioned above, other tissue engineering hydrogels, or potentially cell-laden hydrogels provide alternative infilling materials for the hourglass interlocking geometry approach.

The computer model of the cartilage-matrix hydrogel infilled with the hourglass structure provided value in determining a design angle of 40° that would provide the most possible loading resistance in both directions, where the two different shear direction moduli intersected (**Fig. 5.2C**). Desirable performance in the 1-direction was achieved without sacrificing performance in the 2-direction by selecting a $\theta = 40°$ hourglass structure. To the best of our knowledge, anisotropy has not been emphasized in previous studies on biphasic interface strengthening strategies.

The interface shear modulus additionally provided the model with a comparison with the empirical interface shear experiment. The model exhibited apparent interface moduli that were on the same order of magnitude with the empirical results. The agreement between the model and experiment provided a basis for validation of the computer model results. Although three hourglass tubes were arranged side-by-side in the experiment, the simple representative hourglass structure of the computer model provided a reasonable comparison with the experiment results. Different hydrogels were used in the empirical

tests, but the increasing apparent interface shear modulus trend with different hourglass angles.

The mechanism by which the hourglass exhibited enhanced interface shear performance was further analyzed with a computer model. In empirical tests, increasing the θ angle raised the ultimate shear stress in the 1-direction with agarose. The model predicted that the increased θ angle shifted the stress to be more compressive. Additionally, increasing θ redistributed the stress out further across the hourglass surface. Although the model used cartilage matrix hydrogel properties, all the constitutive relations were kept constant across simulations with different θ, emphasizing trends caused by the θ geometry. The advantage of the hourglass shape in the 1-direction being that the slope caused a shift in stress toward compressive stress. The simulations helped to visualize the distribution of the 3rd principal stresses, σ_3 inside the hydrogel during shear loads in the 1-direction (**Fig. 5.3A-C**). The greater 3rd principal stress magnitudes exhibited by the hourglass structures with higher θ than those with lower θ provided an advantage for enhancing strength. The propensity of the hourglass to generate higher compressive stresses provided more resistance to horizontal loads than lower θ designs (**Fig. 5.2B, 5.3A-C**). Other computer models from previous studies suggested that adding an interdigitating crosshatch pattern increased both σ_1 and σ_3 [107], [267]. The smooth rising hourglass shape in the current study did not demonstrate higher tensile stresses when θ increased from 25 to 44° (**Fig. 5.3F, G**). The potential value of the hourglass feature at enhancing interface strength was demonstrated by a transfer of loading to the right, and a shift to greater compressive stresses (i.e., higher magnitude σ_3) with no appreciable changes to the tensile stress, σ_1. The shift to compressive stress may have raised the load at which adhesive failure would occur in

91

experiments due to the hydrogel sliding across the tube. The stress analysis suggested that the hourglass design would be capable of both enhancing the scaffold interface strength by shifting the stress to compression and transferring the loads across the hourglass surface.

The changes in θ had on the two different loading directions were the result of the hourglass tube's anisotropy. The direct relationship θ had with the 1-direction was likely due to the more distinct wall-feature as a compressive barrier against loading with increasing θ. Whereas from the 2-perspective, increasing θ created more separation from the length of the tube and thus reduced the resistance for the loading crosshead.

The interface shear strength values from the current study suggested that agarose and PHA-PEGDA-DVC infilled scaffolds may not provide adequate strength for all physiologic conditions. Joints that bear most of the weight such as the knees would likely require scaffolds that may support higher shear stresses than the 51 kPa exhibited in the current study [268]. Changes to the design that make the hydrogel flush to the surface may increase the actual performance of biphasic scaffolds. For example, a previous study's biphasic scaffold created a sunken interlocking region that allowed a hydrogel to be infilled flush with the surface of the temporomandibular joint condyle [32]. Although the scaffold must remain intact to achieve tissue repair after implantation, it is not clear what specific interface shear stress requirements would be for adequate osteochondral regeneration in various diarthrodial joints. Scaffold interface strength should allow for a period of post-implantation repair in the physiologic joint environment. For comparison, interface shear strengths of 85 kPa were achieved when a neocartilage layer was combined with a porous hydroxyapatite and cultured *in vitro* for 35 days of cell-mediated remodeling [248], [269]. Future work may examine other material systems with higher strength hydrogels.

Multi-material systems that employ multiscale 3D-printing methods offer additional advantages to enhanced interface shear strength. For example, Diloksuman *et al.*[108] leveraged multiple 3D-printing methods to introduce multiscale interface strengthening structures. In that study, a small-scale melt-electrowritten microfiber mesh comprised of PCL provided an interlocking interface between 3D-printable calcium phosphate-based ink and a GelMA hydrogel. Although the resulting ultimate interface shear stress was enhanced by 6.5-fold over non-interlocking interfaces, the magnitude of interface shear stress was limited to 18 kPa. The interlocking strategy reported in the current study, and in numerous other studies enhanced the interface shear performance of biphasic hydrogels; however, further advances in generating high strength interfaces are likely to benefit from the development of hydrogels with enhanced mechanical properties [31], [108], [248], [263].

Compression testing was used to evaluate the anisotropic behavior of hourglass patterns (**Fig. 5.6**). Although the energy to failure for the 40° hourglass under compression in the 3-direction was lower than that of a crosshatch pattern, ultimate stress in the 3-direction for the hourglass structure was higher than the crosshatch. The high energy to failure for the crosshatch in the 3-direction was due to the higher 30% failure strains in the crosshatch design. Compared to the hourglass pattern, the crosshatch stress-strain curve exhibited a larger region of plastic deformation where the stress leveled off before failure (**Fig. 5.1A**).

The additional strength in the 3-direction for the hourglass architecture, taken together with its enhanced interface mechanical performance described above in the 1-

direction, makes the hourglass design an attractive candidate for future work that aims to implant a biphasic scaffold for joint regeneration. Care must be taken to orient implanted hourglass-based scaffolds such that the 1-direction (i.e., aligned with hourglass axis) is aligned with the principal direction of physiologic shear loads and the 3-direction is aligned with compressive loads. For the case of the ginglymoarthroidial temporomandibular joint and the ginglymus knee and elbow joints, the current study suggested the most advantageous orientation for hourglass scaffolds would align the hourglass tubes' long axes with the anteroposterior direction.

The current study developed a combination of computer models to analyze the interface stress effects from changes in the hourglass tube geometry and further evaluated the hourglass structure with an empirical interface shear test. The protocols described in the current study provide a means of evaluating other geometric designs. For example, adjusting the hourglass design by increasing tube spacing in the 2-direction and increasing the overlap in the 3-direction, to reinforce strength in direction of compression could provide greater strength without changing the porosity. The computer model developed in the current study provides a platform for assessing the potential benefits of future hydrogel formulations with higher strength in an interlocking biphasic scaffold.

Like all computer models, limitations may have reduced the predictive potential for the current models. The materials properties were solid, and incompressible. An Ogden model was used to capture the hydrogel's nonlinear stress/strain behavior with a reasonably high-quality fit to compression data [31]. However, the same Ogden relation was used for both compressive and tensile stresses in the model, whereas the hydrogel was only evaluated in compression for fitting the Ogden values [31]. Differences between the

94

compressive and tensile behavior could be included in future models with a previously proposed variant of the Ogden model, however, additional empirical data on hydrogel tension may be required [270]. The friction-free interface between hydrogel and hourglass tube represented a potential limitation of the model that could have contributed to higher values for the experiment's apparent interface modulus compared to the model's.

Future work may consider other hydrogel properties such as viscoelasticity, and permeability that were not captured by the Ogden model used in the current study [31]. Although temporal behaviors may be modeled (e.g., with triphasic theory [271], [272]) and may be important to a range of physiological joint functions, for evaluating the geometric stress effects of the hourglass, we considered the quasi-static Ogden model to provide a useful comparison of stresses generated around the hourglass surface. The hourglass was modeled as a rigid solid; however, should stronger, higher stiffness properties be achieved for the chondral hydrogel phase that approach those of the 3D-printed polymer hourglass structure, then deformation of the hourglass structure would likely become important to the scaffold's interface performance.

The current study constructed an hourglass interface feature based on a sinusoidal wave, but other designs could modify the curve to become steeper in such a way that the stress is further shifted to compression. A variety of other design modifications to the sinusoidal hourglass tube could potentially be explored in future work by varying the design parameters provided here, or by investigating the effects of different hourglass tube arrangements (e.g., a crosshatch pattern of hourglass tubes).

5.6 Conclusions

3D-printing has inspired new strategies to reinforce the interface of scaffolds for osteochondral regeneration. In the current study, we introduced an hourglass geometry that demonstrated desirable anisotropic behaviors. Specifically, the hourglass geometry provided enhanced interface shear strength in one direction parallel with the hourglass tube's long axis and enhanced compressive strength in the orthogonal direction. Therefore, the hourglass interlocking geometry presents a desirable match for the anisotropic mechanical demands of ginglymoarthrodial joints that generate shear loads in the anteroposterior direction and orthogonal compressive loads.

Interface stress analysis suggested that the stress shifted to a become more compressive in nature, that could prevent hydrogel failure in tension. The simulations further suggested that the hourglass's θ design parameter exhibited an important effect on the apparent interface shear modulus with similarly high values for the 1- and 2-directions of shear loading at 40°. Interface shear experiments on a 40° hourglass biphasic scaffold infilled with PHA-PEGDA-DVC demonstrated superior mechanical performance for both the 1- and 2-directions compared to a crosshatch control. Furthermore, the compressive strength of the 40° hourglass infilling architecture exhibited advantages when oriented such that compressive loads are perpendicular to the hourglass tube's long axis. Thus, the mechanically interlocking strategy with an hourglass feature represents a promising direction for improving osteochondral scaffold outcomes after implantation. Future work is warranted that incorporates the hourglass feature with high strength hydrogels into an anatomically-shaped osteochondral scaffold for potential *in vivo* implantation into a ginglymoarthrodial joint such as the temporomandibular mandibular condyle.

Chapter 6: 3D-Printed Polycaprolactone Scaffolds Embedded with Hydroxyapatite, Devitalized Tendon, or Demineralized Bone Matrix[5]

6.1 Abstract

Critical-sized bone defects remain a major challenge in the clinic as commercially available scaffolds fail to regenerate sufficient, stable bone. A clinical need for enhanced osteoinductive scaffolds has been recognized to improve treatment outcomes for critical-sized bone defects. Modification of polymeric biomaterials with bioactive materials provide both osteoconductive and osteoinductive cell responses to improve bone regeneration. Here, we established a method for fabricating polycaprolactone-based (PCL) filament as a composite material with high natural bioactive content that can be used in commercially available fused deposition modeling 3D-printers. For osteoconductive functionalization, we employed hydroxyapatite. For osteoinductive functionalization, we incorporated either Allogro® demineralized bone matrix (Allo) or devitalized tendon (DVT) into polycaprolactone 3D-printed scaffolds.

Porous 50% w/w PCL-based scaffolds were 3D-printed with the remaining 50% w/w comprised of: (A) 37.5/12.5%, (B) 25/25%, and (C) 12.5/37.5% mixtures of osteoconductive hydroxyapatite (HAp) and osteoinductive Allo or DVT, respectively. A room-temperature HAp blast coating technique was additionally investigated to introduce hydroxyapatite coating to 3D-printed PCL-HAp. A method was presented to assess 3D-print quality. The 3D-printed scaffolds were characterized with scanning electron microscopy, and mechanical testing. Irregular surface textures were introduced to 3D-printed PCL with the addition of hydroxyapatite, devitalized tendon, or demineralized bone matrix. The compressive modulus of the multimaterial mixture with 50% polycaprolactone, 12.5% hydroxyapatite, and 37.5% w/w demineralized bone (PCL-HAp-Allo-A) was 60% higher compared to pure polycaprolactone (8 ± 3 MPa). Furthermore, the osteogenic expression of human bone mesenchymal stem cells (hBMSCs) on the 3D-printed PCL-HAp-Allo-C scaffold had significantly greater average osteogenic gene expression for RUNX2, OCN, and COLX compared to pure PCL. Overall, a mixture of PCL, HAp, and Allo better supported in vitro signs of osteogenesis without compromising the cellular survival or stiffness of a pure polycaprolactone scaffold. Future work is warranted that investigates the potential for PCL-HAp-Allo-A to induce bone regeneration *in vivo.*

6.2 Introduction

Critical-sized bone defects resulting from cancer resection, or congenital diseases, in addition to non-union after trauma often requires treatment with bone grafts [273], [274].

The gold standard for bone grafting, autografts (i.e., tissue harvested from the host), are limited by an additional procedure with potential donor-site morbidities and complications [275], [276]. Synthetic scaffolds provide an attractive alternative to autografts; however, limited bone regeneration prevent them from being used for critical-sized defects. A bioactive biomaterials approach is needed to fabricate bone scaffolds that can provide stable bone regeneration of critical sized defects. The following bioactive materials have been used in previous investigations aimed at regenerating bone: (1) Allogro® demineralized bone matrix (Allo) has demonstrated both osteoinductive and osteoconductive properties for bone grafting [273], [277]. Hydroxyapatite (HAp), bone's fundamental mineral constituent is an osteoconductive material that is additionally used for bone grafting [278]. (3) Devitalized tendon (DVT) has been investigated as a collagenous extracellular matrix to expedite endochondral ossification [279], [280], [281], [282]. However, these bioactive constituents must be combined with a scaffold vehicle to maintain a localized regenerative response in tissues [283].

Interest in 3D-printing for tissue engineering has boomed with a high number of publications from less than 5 citations in 2010 to over 1800 citations in 2022 [12]. 3D-printed scaffolds are an attractive strategy for bone regeneration applications because they can be rapidly fabricated with high control over an interconnected porous architecture to promote bone regeneration [13] [14–20] Polycaprolactone (PCL) has long been a material of choice for osteogenic scaffolds that exhibit biodegradable properties, and has been FDA-approved in specific applications [289]. PCL has been combined with several other bioactive compounds for various tissue engineering applications [291], [292], [293], [294]. PCL composites have been 3D-printed through a variety of techniques such as fused

deposition modeling (FDM) or inkjet printing [285], [295], [296]. The relatively low cost of FDM 3D-printers has made it widely available for bone tissue engineering in a convenient and portable format [284], [285], [286], [287], [288], [289], [290]. FDM printing has demonstrated sufficient resolutions to recreate bone structure and is capable of 3D-printing a wide range of polymer compositions with potential applications to bone tissue engineering.

3D-printers have been adapted to print several biodegradable polymers (e.g., PLLA, PVA, and PLGA) that may be combined with bioactive materials as a composite [297]. 3D-printed PCL has been functionalized with several different components at different concentrations. In previous studies, Hydroxyapatite was successfully FDM 3D-printed with PCL at concentrations ranging up to 40% [28]. A 3D-printable ink was utilized to print scaffolds with up to 90% w/w hydroxyapatite [29]. DBM and HAp were both combined with PLGA at 70% v/v to prepare an ink for 3D-printing with a 3:1 ratio of HAp:DBM [27]. Many other bioactive components (e.g., bio-oss, bioglass, tricalcium phosphate, growth factors, and decellularized bone matrix) have additionally been combined with PCL to create FDM 3D-printed scaffolds for bone tissue engineering [30,31].

Bone scaffolds may undergo additional surface modifications to tune a biomimetic response. Hydroxyapatite coatings have continuously been investigated for bone tissue engineering for the last few decades [300]. HAp has been coated onto metallic implants with a variety of techniques (e.g., electrochemical deposition, plasma spraying) to enhance osseointegration [33]. In a previous study, 3D-printed PCL-βTCP was modified using a solution of collagen and 5% w/w HAp that was allowed to evaporate leaving the bioactive

material coating on the scaffold [302]. Dip coating titanium implants with bioactive glass has been investigated for dental implants [303]. Although PCL has been used to coat metallic implants [300], [304], and HAp has been blast-coated onto titanium at room temperature [305], to the best of our knowledge HAp has not previously been coated on 3D-printed PCL with a pressure blasting technique.

In the current study we introduce a 3D-printed PCL-based scaffold containing mixtures of bioactive HAp with either DBM or DVT. We additionally blast coated a PCL-HAp composite with pure HAp powder at room temperature. The composites developed in the current study aimed to address several limitations of synthetic 3D-printed materials by presenting the cells with varying bioactive components: HAp provided an osteoconductive bioactivity; DBM or DVT provided osteoinductivity. The goals of the current study were to (1) Present a method to assess 3D-print quality of a commercially available FDM 3D-printer and tune printer settings. (2) Evaluate 3D-printed surface quality and mechanical performance of several 3-component material concentrations. And (3) evaluate the osteogenic cell response to the scaffold with human bone marrow stem cells (hBMSCs).

6.3 Methods

6.3.1 Supplies

All materials were obtained from Sigma-Aldrich (St. Louis, MO) unless otherwise stated. All *in vitro* study and cell culture supplies were obtained from Thermo Fisher Scientific (Waltham, MA) unless stated otherwise. Porcine Achilles tendon was obtained from Oklahoma State University College of Veterinary Medicine from unrelated studies.

6.3.2 Filament making and 3D-printing scaffolds using fused deposition modeling

PCL (50k MW, Polysciences, Inc., Warrington, PA) filament containing various concentrations of HAp (Aldrich, St. Louis, MO), with either DVT (made from porcine Achilles tendon procured from a local abattoir), or Allo (Allosource, Cherry Creek, CO) was made using a filament extruder (Filabot, Barre, VT). All composite materials (i.e., PCL, HAp, and DVT or Allo) were weighed dry, combined to the desired ratios, then mixed by handshaking a closed vessel for 2 min. The mixture was then loaded into the hopper of the filament extruder and extruded at 60˚C to produce a filament diameter of ~1.75 mm. A custom variable speed puller motor assembly was employed to grip and pull the filament through a cold DI water bath at a controlled rate. Filament was then fed into a Lulzbot TAZ 6 printer (Lulzbot, Fargo, ND) for 3D-printing at 80˚C. Print speeds were 70 mm·s^{-1} unless otherwise described. Diagnostic 3D-printed part designs for evaluating print quality were adopted from common practice among 3D-printing enthusiasts and designed using Solidworks (Dassault Systèmes, Vélizy-Villacoublay, France). 3D-printed scaffolds were then submersed in 5 M NaOH for 30 min to enhance surface texture and hydrophilicity, washed 3X in DI water, and sterilized for 30 min using ultraviolet light. Overall, eleven different material groups were made. Two-component composites with (1) Pure PCL, (2) PCL-HAp, (3) PCL-DVT, and (4) PCL-Allo were made with 50% w/w. (5) PCL-HAp-Coat group was fabricated by blasting the surface of PCL-HAp with 30 PSI pressurized air with additional HAp and then washing 3X with DI water. Three component mixtures were additionally fabricated at three different concentrations: The letters *A*, *B*, and *C* were used

to designate both the (6-8) PCL/HAp/DVT and (9-11) PCL/HAp/Allo group concentrations of (A) 50/37.5/12.5%, (B) 50/25/25%, and (C) 50/12.5/37.5% w/w, respectively.

6.3.3 Print dimensions and quality assessment

Print quality was evaluated by comparing images of the experimentally printed scaffolds to a digital design. Images were first registered, binarized, and next a cross-correlation was performed to determine the percentage of pixels that matched between the printed version and the digital design image. The printed constituents were evaluated by measuring the color difference relative to pure PCL. Allo had a goldenrod color appearance that was darker than the other materials used in the current study. The color difference was measured by comparing images of solid Allo-containing composite discs with pure PCL and calculating the Euclidean distance in the international commission on illumination CIELAB color space using a custom MATLAB script.

6.3.4 Scanning electron microscopy and energy dispersive X-ray spectroscopy

Images of each scaffold were captured for evaluation of the surface quality. Specimens were sputter coated with 4 nm iridium on a Hummer VI (Anatech Ltd., Battlecreek, MI). A Thermo Quattro S field-emission environmental scanning electron microscope (FE-ESEM, Thermo Fisher, Waltham, MA) was used with a 20 kV acceleration voltage. X-ray spectra were plotted to evaluate peak sizes associated with specific elements in the composites.

6.3.5 Unconfined compression testing

A uniaxial mechanical testing setup was used to evaluate the compressive modulus of composite PCL prints (Test Resources, Shakopee, MN). Discs were 3D-printed (n=6) with a thickness of 1.1 ± 0.1 mm and diameters that were 6.6 ± 0.2. Individual specimen dimensions were used to calculate the stress and strain for each specimen. A tare load of 10 N was used prior to compressing each disc at 1 mm·min^{-1} (1.7 %·s^{-1}) until reaching a gap length of 0.4 mm where the test was ended. The compressive elastic modulus was determined by fitting a line to the 2-5% strain range of the stress/strain curve.

6.3.6 Cell culture

hBMSCs, originally isolated from seven individual donors' healthy iliac crest, and expansion medium were obtained from Rooster Bio, Inc. (Cat# MSC-003, SU-022, SU003, Frederick, MD). Cells were combined from each donor in equal amounts and cultured according to the manufacturer protocol and passaged every 4-5 days or when confluent using trypsin-EDTA (0.25%). The base medium consisted of penicillin-streptomycin (1%; 15140122), insulin-transferrin-selenium+premix (1%; Cat# CB40352), non-essential amino acids (1%; 11140050), sodium pyruvate (1 mM; Cat# 11360070), and ascorbate-2-phosphate (50 μg·mL^{-1}; A8960), dexamethasone (100 nM; Sigma-Aldrich, Cat# D4902), and mixed with Dulbecco's modified eagle medium (Cat# 10566024). For the osteogenic medium, 100 ng·mL^{-1} bone morphogenetic protein (BMP-2, Cat# 355-BM, R&D Biosystems, Minneapolis, MN) was supplemented to the base medium.

6.3.7 Reverse transcription quantitative polymerase chain reaction

Porous scaffolds with a solid base were 3D-printed as described above. The scaffolds were placed in a tissue culture treated 96-well plate. Passage 3 cells were seeded (20,000 cells per scaffold, 100 cells·μL^{-1}) on each scaffold in base or osteogenic medium. Plates were kept in hypoxic conditions (i.e., 37˚C, 5% carbon dioxide, 5% oxygen) with media replenished every 3 days. All samples were prepared for quantitative reverse transcription polymerase chain reaction (RT-qPCR) after 14 days.

A Bio-rad CFX Opus 96 Real-Time PCR System (Hercules, CA) was used as previously described [38]. The following Bio-rad PrimePCR™ PCR assays were used: **(1)** GAPDH (qHsaCEP0041396), **(2)** runt-related transcription factor 2 (RUNX2, qHsaCEP0051329), **(3)** collagen type I (COL1A1, qHsaCEP0050510), **(4)** collagen type X (COLX, qHsaCEP0051254), and **(5)** Osteocalcin (OCN, qHsaCEP0041159). Relative gene expression levels were calculated using the $2^{-\Delta\Delta Ct}$ method [39]. The comparator group used to normalize all data was PCL in base medium (n=8).

6.3.8 Statistical analysis

Statistical analyses were performed with one-way ANOVA with Tukey's post-hoc test. Significance was defined when α=0.05. All data were mean ± standard deviation.

6.4 Experimental Results

6.4.1 Print Quality

Porous scaffolds exhibited enhanced print quality at speeds above 30 mm·s^{-1}. Prints exhibited an irregular boundary compared to the computer-generated design (**Fig. 6.1A**) at a low speed of 5 mm·s^{-1} (**Fig. 6.1B**). Prints at higher speeds of 60 (**Fig. 6.1C**) and 110

mm·s^{-1} exhibited more regular boundaries than prints at slow print speed of 5 mm·s^{-1} (**Fig. 6.1D).** Prints with moderate speeds between 20-100 mm·s^{-1} exhibited 15% higher correlation values averaging 0.31 ± 0.02 approaching compared to the low-speed prints (i.e., < 2 mm·s^{-1} printhead speed) with a correlation value of 0.25 (**Fig. 6.1E**).

6.4.2 Visible light spectrum analysis

Solid 3D-prints for each material investigated here exhibited higher color differences relative to pure PCL with increasing concentrations of Allo (**Fig. 6.2A**). However, the other constituents, DVT and HAp, did not exhibit a dose-dependent relationship with color difference. The Allo demineralized bone matrix exhibited a darker, more yellow quality as may be appreciated by examining the top 5 representative images in **Fig. 6.2B**.

6.4.3 Scanning electron microscopy and X-ray energy dispersive spectroscopy

Calcium (Ca) signals exhibited by PCL-HAp-Allo and PCL-HAp-DVT were consistent with the ratios of HAp content. Specifically, high, medium, and low peak Ca signals of 41, 17, and 6% relative to carbon (C) were exhibited by Allo-A, Allo-B, Allo-C, respectively, consistent with the 37.5%, 25%, and 12.5% HAp in those groups (**Fig. 6.2C**). Additionally, the high, medium, and low peak Ca signals of 22, 7, and 3% were exhibited by scans of DVT-A, DVT-B, and DVT-C, respectively (**Fig. 6.2D**).

The prints exhibited various textures with the addition of the different constituents (**Fig. 6.3)**. Pure PCL exhibited a smooth surface. Surfaces with mixtures of HAp and DVT (i.e., PCL-HAp-DVT-A through C) and mixtures of HAp and Allo (i.e., PCL-HAp-Allo-

A through C) exhibited heightened textures compared to PCL. The PCL-DVT surface exhibited a highly undulating surface compared to PCL-Allo, PCL-HAp, and PCL. A thin layered structure was exhibited by the PCL-HAp-Coat group.

6.4.4 Unconfined compression

Representative stress vs. strain plots exhibited a range of different slopes for the different material groups (**Fig. 6.4A**). The compressive elastic moduli were higher in PCL-Allo (i.e., 15 ± 3 MPa) and PCL-HAp-DVT-C (i.e., 15 ± 4 MPa) than in PCL (8 ± 3 MPa, $p < 0.05$, **Fig. 6.4B**). PCL-HAp's modulus increased by 54% to 12 ± 2 MPa compared to pure PCL. The lowest modulus of the groups tested in the current study was exhibited by PCL-DVT (5 ± 4 MPa). The A-, B-, and C-mixtures for both DVT and Allo exhibited similar trends, however, no statistically significant differences were exhibited between the three-component mixtures. All of the A-, B-, and C- mixtures for DVT and Allo were at least 34% higher than PCL ($p < 0.05$) except there was no difference for PCL-HAp-Allo-B with a compressive modulus of 10 ± 4 MPa.

6.4.5 Reverse transcription quantitative polymerase chain reaction

Higher expressions of osteoblast markers, RUNX2 and OCN, were exhibited by the PCL-HAp-Allo-C group than the pure PCL, PCL-HAp, PCL-HAp-Allo-A, PCL-HAp-Allo-B, and DVT-containing groups of PCL-HAp-DVT-A and PCL-HAp-DVT-B ($p < 0.05$, **Fig. 6.5A, B**). Specifically, PCL-HAp-Allo-C exhibited a 31-fold, 111-fold, and a 100-fold increase in RUNX2, OCN, and COLX, respectively relative to PCL ($p < 0.05$).

No differences in COL1 expression were exhibited by the different material groups (**Fig 6.5C**). COLX expression was additionally higher in PCL-HAp-Allo-C compared to all other groups except for PCL-HAp-Coat and PCL-HAp-DVT-C (**Fig. 6.5D**).

6.5 Discussion

The current study demonstrated a practical method for 3D-printing PCL-based materials customized with a range of bioactive materials. PCL was mixed together with HAp and DVT or HAp and DBM from a raw powder to fabricate filament that can be used in commercially available fused deposition modeling 3D-printers. Scaffolds with up to 50% w/w bioactive material were achieved in the current study compared to other studies that used fused deposition modeling with bioactive concentrations of 10-40% w/w [31,40,41]. The resulting filament was made with high concentrations of putatively osteogenic components of HAp, DVT, or DBM [42]. In another study, a so-called "3D-paint", or bioprintable ink for pneumatic extrusion combined 30% v/v PLGA with a mixture of HAp and DBM [27]. The current study exhibited novelty in mixing HAp and DBM into a filament for fused deposition modeling. Higher concentrations of 60 and 70% HAp in PCL-HAp were fabricated in the current study (data not shown) resulting in highly non-uniform and brittle filament that was not usable in the 3D-printer. In the current study, we successfully fabricated filament with up to 50% w/w bioactive materials that could be 3D-printed as porous scaffolds.

PCL-based 3D-printing with fused deposition modeling has inherent challenges due to the material properties of PCL. The melting temperature of PCL is ~60°C, much lower than the 200°C of other FDM filaments (e.g., PLA or PETG3D). The lower melting

temperature of PCL did not present a challenge for the 3D-printer's hot end to melt; on the contrary, the PCL was prone to melting in the feeding tube above the heat break before entering the hot end resulting in potential jamming.

For the materials used in the current study, we determined that a temperature of 80°C was high enough for flowable lines to print without jamming. The low melting temperature of PCL additionally presented a challenge for the layer-by-layer 3D-printing process. Structural support must be present for the successive layers to be printed; however, layers of PCL that have not cooled from the hot molten phase could introduce artifacts in the successive layers and/or failed 3D-prints. In a previous study that used pneumatic extrusion 3D-printing with 30% HAp and PCL [31], the temperature, pneumatic pressure, and extrusion head speed were varied empirically to maximize print quality. Print quality was assessed using a previously published technique where a top-down image of the printed part was compared with a computer-generated image of the part's design to provide a correlation factor [17]. The aforementioned study's 40% infill density cubic scaffolds were printed at different filament feed rates resulting in a maximum correlation factor of 0.32 at a feed rate of 190 mm/min. In the current study, a maximum correlation coefficient of 0.35 was obtained using a print speed of 60 mm·s^{-1}. The feed rate in our Lulzbot TAZ 6 3D-printer was calibrated to 406 stepper motor steps for one mm of filament. The lower print quality at slow speeds suggested that the printing parameters were better coordinated at higher speeds than those below 30 mm·s^{-1}. For comparison, another study that accurately 3D-printed PCL scaffolds used speeds of 2 mm·s^{-1} [43]. The results of the current study suggested that higher quality prints with PCL materials using a FDM 3D-printer are

produced with temperatures of 80˚C and print speeds at 60 mm·s^{-1} than those with lower speeds below 30 mm·s^{-1}.

The Allo content in 3D-printed discs was characterized using a visual spectrum analysis, though additional validation of this technique is required to interpret conclusive meaning. To our knowledge, this technique has not been used to evaluate content, but a similar CIELAB technique was validated to assess the color of objects that were 3D-printed in a desired color [44]. Our results suggested that the observed color differences between DBM and the other components may be leveraged to measure differences in 3D-printed material content with additional work to calibrate the color differences with content differences. Other techniques to characterize material content such as: FTIR, XRD, EDS, or Raman spectroscopy could be useful for validating visual spectrum analysis in future work [31,43,45].

Variable surface textures from smooth (i.e., pure PCL) to irregular (i.e., PCL-DVT) were evident in SEM images of the different 3D-printed materials. The smooth appearance of pure PCL with uniform struts in the current study was consistent with SEM of 3d-printed PCL reported in other studies [31]. Although a more irregular surface for PCL-HAp was reported in another study, the HAp was coated onto a plasma-treated PCL scaffold by immersing the scaffold in a 1% w/w solution of HAp and distilled water [43]. Images from computed tomography (CT) and SEM in a different study exhibited an irregular surface for PCL combined with 30% w/w HAp, Bio-Oss, or decellularized bone matrix [31]. In another study, a fairly uniform surface for 9:1 HAp:PCL was exhibited by SEM; however, the study used an ink-based 3D-printing method that was different from the current study's FDM method [29]. HAp:DBM ratios of 3:1, 1:1, and 1:3 were mixed with 30% v/v

polylactide-co-glycolide copolymer and characterized with SEM on cross-sections of 3D-printed struts that were cut [27]. The different ratios of HAp:DBM were evidenced by the different size particles for HAp and DBM in the SEM images of the strut cross-sections. Similarly, the SEM images that contained DBM or HAp in the current study exhibited a more irregular surface than pure PCL. SEM images in another study that combined collagen with PCL exhibited a more irregular surface than pure PCL consistent with SEM of DVT-containing scaffolds in the current study [43].

The HAp coating onto PCL-HAp with a blasting technique resulted in a thin layer of calcium-containing material on the surface with regions that appeared to be pure HAp. The regions of thick HAp present a possible risk of brittle delamination, and wear particle formation with the potential to stimulate an unwanted foreign body response if implanted *in vivo*. Previous studies investigated foreign body reaction related to wear particles dislodged from the implanted joint surface [46,47]. In contradiction to the current study, another study used a coating of 1 % w/w HAp that exhibited a relatively uniform surface appearance as evidenced by SEM [43].

The 8 to 15 MPa modulus range in the current study's PCL-based composites were consistent with the range reported in the literature. A wide range of moduli from 4 to 300 MPa have been reported in PCL-based composites comprised of HAp or other bioactive materials (e.g., Bio-oss, decellularized bone matrix) [29,31,40,41,48,49]. The increase in stiffness from the addition of HAp was consistent with results reported in other studies [40,48]. In a different study, the addition of 30% strontium-HAp to PCL increased the modulus 2-fold to 50 MPa [48]. A lower modulus; however, was observed with 50% concentrations of strontium-HAp. The relatively lower PCL modulus in the current study

was likely due to differences in the testing methods and material preparation, such as a 10 times faster compression rate of 10 mm·s^{-1} and PCL-HAp being mixed with a tetrahydrofuran solvent that was evaporated before 3D-printing. Another study used a melt blended PCL incorporating 30% HAp and reported a modulus of 39.71 ± 3.38 MPa [40]. Again, the higher modulus compared to our study may have been due in part to the different composite preparation techniques of a solvent to mix PCL with HAp, or melt blending in a separate step before extruding from a printhead syringe.

Cells seeded onto both of the -C mixtures (i.e., PCL-HAp-Allo-C and PCL-HAp-DVT-C) that had 37.5% w/w Allo or DVT and 12.5% w/w HAp exhibited cellular upregulation of RUNX2, OCN, and COLX. The lower gene expressions for mixtures -A and -B suggested that there was a ratio-dependent hBMSC response to the putatively osteoconductive HAp and osteoinductive Allo or DVT. A different study that 3D-printed PCL with 30% w/w HAp exhibited upregulation of RUNX2 compared to PCL, but no significant differences were observed in OCN gene expression [31]. The highest upregulation of RUNX2, OCN, and COLX with PCL-HAP-Allo-C and second highest expression in PCL-HAp-DVT-C further supported the conclusion that the cells exhibited osteogenic differentiation in response to a specific ratio of DVT or Allo osteoinductive materials with HAp. In a different study, a combination of 3:1 HAp:DBM with 30% v/v PLGA as a 3D-printed ink exhibited upregulation of both RUNX2 and OCN gene expression [50]. The osteoinductive behavior of Allo has been the subject of prior investigations that aimed to establish a high throughput bioassay for its bioactivity, yet to date *in vivo* methods remain the standard method for characterizing the bioactive quality of Allo [5]. The results of the current study suggested that the bioactivity of Allogro DBM

were enhanced in combination with a specific ratio of HAp and PCL. Upregulation of osteogenic genes in response to DVT suggested that the collagenous phase was additionally important to the potentially osteogenic mixture with HAp. In any case, it remains unclear what molecular constituents were responsible for the upregulated genetic expression with specific ratios of Allo or DVT with HAp and PCL. The current study may provide useful insights for further investigations of a high throughput bioassay to determine osteoinductive quality of fresh-processed DBM. For example, quantification of cell proliferation and deposited extracellular matrix could be evaluated as previously described [5], or RNA sequencing could be performed on a range of materials presented in the current study to determine a broader gene regulation profile associated with new bone formation. Furthermore, the specific proteins and other molecular components of the current study's materials could be additionally characterization and then prepared as a set of purified materials for further investigation.

The data in the current study confirmed clear advantages for using PCL-HAp-Allo-C for an osteogenic scaffold. Upregulation of osteogenic markers suggested that the -C materials may exhibit an osteogenic response *in vivo*. The combination of HAp with DBM or DVT in the current study introduced a biological response that warrants further investigation into the molecular biology mechanisms for hBMSC-to-osteoblast differentiation. The mechanical properties were stiffer than pure PCL with the -C mixtures, confirming the potential for scaffold implantation. We do not expect the biocompatibility or physical properties for the -C mixtures to detract from the biocompatibility of pure PCL as a scaffold material of choice for implantation. Further investigation of the degradation properties could help determine the potential for *in vivo* implantation. The results for the -

C mixtures in the current study warrant further investigation to determine the ultimate regenerative potential with an *in vivo* study. For example, ruther investigation of the high osteogenic expression could be performed by evaluating osseus tissue growth surrounding an implanted scaffold 3D-printed from PCL-HAp-Allo-C.

6.6 Conclusions

Custom bioactive mixtures of PCL-based filament were successfully fabricated and used to 3D-print several composite PCL-mineral scaffolds. The scaffolds were characterized for relative osteogenic gene expression utilizing hBMSCs. 3D-printed, porous scaffolds comprised of PCL-HAp-Allo exhibited greater osteoinductive potential only when fabricated at 50/12.5/37.5% concentrations compared to synthetic PCL or other composite concentrations. Although the PCL-HAp-DVT-C scaffolds also exhibited partially enhanced osteoinductivity the expression levels were not higher than the pure PCL or control groups. The PCL-HAp-Allo-C composite induced significant upregulation of RUNX2, OCN, and COLX relative to pure PCL scaffolds. This greater osteo-inductivity may be due to the irregular surface texture (as imaged with SEM), or the presentation of the apatite *and* collagen phases from Allo, or growth factors on the surface of the scaffolds following the printing process. These results indicate that mixing 3D-printed PCL scaffolds with a combination of HAp and Allo DBM together potentially enhance bone healing *in vivo* compared to HAp, DVT, or DBM alone.

Chapter 7: Discussion and Conclusions

7.1 Summary

The current dissertation developed several novel, 3D-printable biomaterials that were characterized *in vitro,* and evaluated *in vivo* for tissue regeneration in the temporomandibular joint mandibular condyle. Two key types of biomaterials were developed and characterized for their potential to regenerate cartilage and bone: (1) A cartilage-matrix based hydrogel, and (2) Polycaprolactone functionalized with demineralized bone matrix and hydroxyapatite. A pilot study was performed *in vivo* to characterize the regenerative potential of the 3D-printed scaffold, either with or without the cartilage matrix-based hydrogel. Additionally, a novel interface design was explored to enhance the interface shear mechanical performance of a 3D-printed scaffold and a cartilage-matrix hydrogel.

First, I characterized the chondrogenicity and mechanical performance of a cartilage-matrix hydrogel (Chapter 3). This study highlighted the mechanical characterization of tissue engineering hydrogels and offered an Ogden model analysis with a high-quality fit to the stress/strain data across the full strain range to hydrogel failure. With the Ogden model, the strain range used in the fitting process need not be defined *a priori*. The main conclusion was that the Ogden model was a valuable alternative to the linear, compressive modulus for characterizing tissue engineered hydrogel mechanics to failure. Although the chondroinductive effects of devitalized cartilage were previously explored in our research group, novel insights were additionally presented about the effect of devitalized cartilage content in a composite hydrogel with pentenoate-modified

hyaluronic acid-polyethylene glycol diacrylate on the chondrogenic expression of human mesenchymal bone marrow stem cells. Upregulated expression of ACAN and SOX9 was associated with a 15% w/v devitalized cartilage composite hydrogel. The genetic expression data that suggested these hydrogels were potentially chondrogenic provided validation for application of the Ogden model. Part of the study's goal was to apply the Ogden model to a tissue engineering hydrogel. This work presents a significant advancement in the application of the Ogden model to hydrogels employed for tissue engineering.

Next, I characterized the *in vivo* effects of a 3D-printed, patient-fitted biphasic TMJ mandibular condyle implant on cartilage and bone regeneration (Chapter 4). Although there has been limited research on a biphasic scaffold to regenerate TMJ tissues, the use of a biphasic acellular scaffold to regenerate region-specific cartilage and bone in the TMJ mandibular condyle has been overlooked. I fabricated a novel, 3D-printed biphasic scaffold with custom, in-house filament comprised of polycaprolactone, and 20% w/w hydroxyapatite that was infilled with a cartilage-matrix hydrogel. 6 months post-implantation in a small animal, I characterized the bone and cartilage tissue response. The study revealed that the biphasic scaffold could support TMJ function, exhibit signs of neo-cartilage formation in the surface region, and bone formation; however, improving bone continuity within the scaffold remains a major goal. The study additionally revealed that the qualitative strength of biphasic scaffolds was improved by introducing PEGDA to the hydrogel.

Finally, I generated a computer-aided design of an interface geometry that demonstrated enhanced interface mechanical performance in biphasic scaffolds (Chapter

5). I conceptualized an hourglass tube geometry to enhance the interface inspired by undulating steel rods used to reinforce concrete, and the arch form used to reinforce the strength of bridges. I constructed a fully parameterized hourglass interface geometry and determined the effects of one key parameter (i.e., the hourglass curve angle, θ) *in silico* on the interface mechanical performance with a finite element computer model. The main conclusion from the computer model was that the hourglass geometry strengthened the interface by supporting shear loads through compressive stress. The computer model results were confirmed with empirical testing, which demonstrated enhanced interface mechanical performance with a 3D-printed hourglass interface infilled with a cartilage-matrix hydrogel. This work presented a significant advancement in our understanding of the mechanical behavior of biphasic scaffolds under shear loads.

Additionally, I expanded the capabilities of the existing 3D-printed scaffold biomaterial to include hydroxyapatite and demineralized bone matrix (Chapter 6). Stable bone regeneration for the TMJ condyle require a bioactive scaffold. In Chapter 2, a polycaprolactone, 20% w/w hydroxyapatite 3D-printed material supported TMJ function, however, there was no osteoinductive component. The enhanced 3D-printed biomaterial in chapter 6 exhibited signs of *in vitro* osteoinduction with upregulated expression of OCN, RUNX2, and COLX. The study revealed that up to 50% w/w solid, bioactive materials may be combined with polycaprolactone for successful filament fabrication, and that the specific ratios of polycaprolactone, hydroxyapatite, and demineralized bone matrix within the filament (i.e., 50%/12.5%/37.5%, respectively) were important to the stem cell's osteoinductive response.

7.2 Future Directions

Although the enhanced TMJ mandibular condyle biomaterials presented in this dissertation advanced our understanding of the potential for cartilage and bone regeneration, they additionally highlighted the complex nature of osteochondral scaffolds and numerous factors that contribute to their specific cartilage and bone tissue regeneration.

The incorporation of both a 3D-printed osteal phase architecture with a cartilage-matrix hydrogel expanded our knowledge of cartilage and bone tissue regeneration *in vivo*. Currently, a single composition of polycaprolactone and 20% hydroxyapatite was 3D-printed, and a future next step may be to incorporate demineralized bone matrix at a specified concentration with hydroxyapatite and polycaprolactone to enhance bone tissue regeneration *in vivo*. While the upregulation of osteal genes in stem cells seeded on 50% PCL functionalized with 12.5% hydroxyapatite, and 37.5% demineralized bone matrix was observed in Chapter 6, these were *in vitro* results with controlled cell culture conditions. Using 3D-printed, patient-fitted condylar scaffolds comprised of functionalized polycaprolactone would allow us to determine the osteoinductive response *in vivo*. Additionally, the degradation properties of polycaprolactone and 20% hydroxyapatite was sufficient to support TMJ function. We can further study the effect of functionalizing PCL with hydroxyapatite and demineralized bone matrix at different ratios by performing an accelerated degradation study and characterizing the mass loss and mechanical properties. This would allow us to study the potential for osteoinductive 3D-printed polycaprolactone functionalized with hydroxyapatite and demineralized bone matrix to support TMJ function and elicit robust bone tissue regeneration *in vivo*. We may additionally include post-processing treatments of the 3D-printed scaffold to enhance the mechanical properties (e.g., thermal treatments).

Further, an hourglass-based microarchitecture may be used to enhance the mechanical properties of a TMJ scaffold oriented to absorb the joint's primary loading directions of compression and shear. To absorb the superoinferior compressive forces of the TMJ mandibular condyle, the hourglass structure proved to be effective with the long axis perpendicular to compression. For the anteroposterior hinge and sliding movements of the TMJ mandibular condyle, hourglass tubes oriented parallel with the shear provided the best interface strength. Future applications of the hourglass geometry in the TMJ may orient an hourglass microarchitecture such that the long axis is aligned with shear in the anteroposterior direction.

The modular method of biphasic scaffold fabrication with the hourglass interface allows any chondroinductive hydrogel formula to be infilled with the hourglass interlocking interface designed as described above in Chapter 5. Future work may develop a chondroinductive hydrogel with enhanced cohesive strength that is infilled with the hourglass feature to further enhance the interface strength. The sinusoidal wave form of the hourglass geometry itself can additionally be modified to have a more pronounced crest of convexity to potentially enhance interface shear strength.

Further, the current thesis focused on regeneration of osteochondral tissues to restore a healthy, resected TMJ mandibular condyle. Future work may expand these scaffold properties to account for the effects of aging and sex differences on TMJ condyle regeneration. The introduction of different pathologies, such as osteoarthritis, or trauma would provide a more holistic perspective on the TMJ mandibular condyle's tissue microenvironment and the specific pathology's role on osteochondral tissue regeneration. For example a scaffold to repair trauma in the TMJ may offer additional mechanical

reinforcement, or a different scaffold to regenerate tissues lost to osteoarthritis may be include anti-inflammatory design features.

7.3 Conclusion

This work led to five novel findings. First, the Ogden model was a useful tool for characterizing the mechanical behavior of representative tissue engineering hydrogels at high strains. Second, stem cells seed on composite cartilage-matrix hydrogels exhibited upregulation of chondrocyte-specific gene markers. Third, differences in an interlocking hourglass interface geometry may affect the interface mechanical performance of an infilled hydrogel. Fourth, biphasic scaffolds may be 3D-printed with customizable PCL filament and support TMJ function *in vivo*. Fifth, 3D-printed PCL functionalized with hydroxyapatite and demineralized bone matrix is potentially osteoinductive. Together these results provide a comprehensive analysis with *in silico, in vitro,* and *in vivo* characterizations of 3D-printable biomaterials and provide important insights that can influence future research, clinical applications, and tissue engineering approaches to temporomandibular joint mandibular condyle tissue regeneration.

References

[1] L. F. Valesan *et al.*, "Prevalence of temporomandibular joint disorders: a systematic review and meta-analysis," *Clin. Oral Investig.*, vol. 25, no. 2, pp. 441–453, Feb. 2021, doi: 10.1007/s00784-020-03710-w.

[2] V. Østensjø, K. Moen, T. Storesund, and A. Rosén, "Prevalence of painful temporomandibular disorders and correlation to lifestyle factors among adolescents in norway," *Pain Res. Manag.*, vol. 2017, pp. 1–10, 2017, doi: 10.1155/2017/2164825.

[3] K. A. Athanasiou, A. A. Almarza, M. S. Detamore, and K. N. Kalpakci, *Tissue engineering of temporomandibular joint cartilage*. in Synthesis Lectures on Tissue Engineering. Cham: Springer International Publishing, 2009. doi: 10.1007/978-3-031-02577-8.

[4] M. M. Sperry, S. Kartha, B. A. Winkelstein, and E. J. Granquist, "Experimental methods to inform diagnostic approaches for painful tmj osteoarthritis," *J. Dent. Res.*, vol. 98, no. 4, pp. 388–397, Apr. 2019, doi: 10.1177/0022034519828731.

[5] "Prevalence of TMJD and its Signs and Symptoms | National Institute of Dental and Craniofacial Research," National Institute of Dental and Craniofacial Research. Accessed: Mar. 26, 2023. [Online]. Available: https://www.nidcr.nih.gov/research/data-statistics/facial-pain/prevalence

[6] M. K. Murphy, R. F. MacBarb, and M. E. Wong, "Temporomandibular joint disorders: a review of etiology, clinical management, and tissue engineering strategies," 2015.

[7] J. R. Salash *et al.*, "Potential indications for tissue engineering in temporomandibular joint surgery," *J. Oral Maxillofac. Surg.*, vol. 74, no. 4, pp. 705–711, Apr. 2016, doi: 10.1016/j.joms.2015.11.008.

[8] L. M. Wolford, D. A. Cottrell, and C. H. Henry, "Temporomandibular joint reconstruction of the complex patient with the techmedica custom-made total joint prosthesis," *J. Oral Maxillofac. Surg.*, vol. 52, no. 1, pp. 2–10, Jan. 1994, doi: 10.1016/0278-2391(94)90003-5.

[9] L. R. L. B. D. Oliveira, I. D. S. Alves, A. P. F. Vieira, U. L. Passos, C. D. C. Leite, and E. S. Gebrim, "Temporomandibular joint: from anatomy to internal derangement," *Radiol. Bras.*, vol. 56, no. 2, pp. 102–109, Mar. 2023, doi: 10.1590/0100-3984.2022.0072-en.

[10] V. P. Willard, B. Arzi, and K. A. Athanasiou, "The attachments of the temporomandibular joint disc: a biochemical and histological investigation," *Arch Oral Biol*, vol. 57, no. 6, pp. 599–606, 2012, doi: 10.1016/j.archoralbio.2011.10.004.The.

[11] K. N. Kalpakci, V. P. Willard, M. E. Wong, and K. A. Athanasiou, "An interspecies comparison of the temporomandibular joint disc," *J. Dent. Res.*, vol. 90, no. 2, pp. 193–198, Feb. 2011, doi: 10.1177/0022034510381501.

[12] M. S. Detamore and K. A. Athanasiou, "Structure and function of the temporomandibular joint disc: Implications for tissue engineering," *J. Oral Maxillofac. Surg.*, vol. 61, no. 4, pp. 494–506, Apr. 2003, doi: 10.1053/joms.2003.50096.

[13] B. J. Bielajew *et al.*, "Knee orthopedics as a template for the temporomandibular joint," *Cell Rep. Med.*, vol. 2, no. 5, p. 100241, May 2021, doi: 10.1016/j.xcrm.2021.100241.

[14] D. Nedrelow, M. Detamore, and M. Wong, "Chondrocytes and fibrochondrocytes," in *Cell-toCell Communciation: Cell-Atlas - Visual Biology in Oral Medicine*, Quintessence, 2022, pp. 45–54.

[15] M. Singh and M. S. Detamore, "Biomechanical properties of the mandibular condylar cartilage and their relevance to the TMJ disc," *J. Biomech.*, vol. 42, no. 4, pp. 405–417, 2009, doi: 10.1016/j.jbiomech.2008.12.012.

[16] E. T. Niezen, B. Van Minnen, R. R. M. Bos, and P. U. Dijkstra, "Temporomandibular joint prosthesis as treatment option for mandibular condyle fractures: a systematic review and meta-analysis," *Int. J. Oral Maxillofac. Surg.*, vol. 52, no. 1, pp. 88–97, Jan. 2023, doi: 10.1016/j.ijom.2022.05.014.

[17] R. A. Strauss and A. Radwan, *Trauma surgery, an issue of atlas of the oral & maxillofacial surgery clinics*. Elsevier Health Sciences, 2019.

[18] Y. R. Khattak *et al.*, "Can growing patients with end-stage TMJ pathology be successfully treated with alloplastic temporomandibular joint reconstruction? – A systematic review," *Oral Maxillofac. Surg.*, Sep. 2023, doi: 10.1007/s10006-023-01180-4.

[19] D. Sultan, R. Pellecchia, and L. G. Mercuri, "Alloplastic TMJ replacement in the skeletally immature patient - A systematic review," *J. Cranio-Maxillofac. Surg.*, Mar. 2024, doi: 10.1016/j.jcms.2024.03.028.

[20] L. M. Wolford, R. Movahed, and D. E. Perez, "A classification system for conditions causing condylar hyperplasia," *J. Oral Maxillofac. Surg.*, vol. 72, no. 3, pp. 567–595, Mar. 2014, doi: 10.1016/j.joms.2013.09.002.

[21] E. Tanaka, M. S. Detamore, and L. G. Mercuri, "Degenerative disorders of the temporomandibular joint: etiology, diagnosis, and treatment," *J. Dent. Res.*, vol. 87, no. 4, pp. 296–307, Apr. 2008, doi: 10.1177/154405910808700406.

[22] L. G. Mercuri and M. S. Caicedo, "Material hypersensitivity and alloplastic temporomandibular joint replacement," *J. Oral Maxillofac. Surg.*, vol. 77, no. 7, pp. 1371–1376, Jul. 2019, doi: 10.1016/j.joms.2019.01.042.

[23] D. Chen *et al.*, "Tissue engineered autologous cartilage-bone grafts for temporomandibular joint regeneration," *Sci. Transl. Med.*, vol. 12, no. 565, pp. 1–16, 2020, doi: 10.1126/scitranslmed.abb6683.

[24] B. T. Smith *et al.*, "Multimaterial dual gradient three-dimensional printing for osteogenic differentiation and spatial segregation," *Tissue Eng. - Part A*, vol. 26, no. 5–6, pp. 239–252, 2020, doi: 10.1089/ten.tea.2019.0204.

[25] S. Hollister *et al.*, "Engineering craniofacial scaffolds," *Orthod. Craniofac. Res.*, vol. 8, no. 3, pp. 162–173, Aug. 2005, doi: 10.1111/j.1601-6343.2005.00329.x.

[26] S. J. Hollister, R. A. Levy, T.-M. Chu, J. W. Halloran, and S. E. Feinberg, "An image-based approach for designing and manufacturing craniofacial scaffolds," *Int. J. Oral Maxillofac. Surg.*, vol. 29, no. 1, pp. 67–71, Feb. 2000, doi: 10.1034/j.1399-0020.2000.290115.x.

[27] R. Schek, J. Taboas, S. Hollister, and P. Krebsbach, "Tissue engineering osteochondral implants for temporomandibular joint repair," *Orthod. Craniofac. Res.*, vol. 8, no. 4, pp. 313–319, Nov. 2005, doi: 10.1111/j.1601-6343.2005.00354.x.

[28] F. Wang, Y. Hu, D. He, G. Zhou, X. Yang, and E. Ellis, "Regeneration of subcutaneous tissue-engineered mandibular condyle in nude mice," *J. Cranio-Maxillofac. Surg.*, vol. 45, no. 6, pp. 855–861, 2017, doi: 10.1016/j.jcms.2017.03.017.

[29] A. R. Chin, J. Gao, Y. Wang, J. M. Taboas, and A. J. Almarza, "Regenerative potential of various soft polymeric scaffolds in the temporomandibular joint condyle," *J. Oral Maxillofac. Surg.*, vol. 76, no. 9, pp. 2019–2026, Sep. 2018, doi: 10.1016/j.joms.2018.02.012.

[30] S. Abramowicz, S. J. Crotts, S. J. Hollister, and S. Goudy, "Tissue-engineered vascularized patient-specific temporomandibular joint reconstruction in a Yucatan pig model," *Oral Surg. Oral Med. Oral Pathol. Oral Radiol.*, vol. 132, no. 2, pp. 145–152, Aug. 2021, doi: 10.1016/j.oooo.2021.02.002.

[31] D. S. Nedrelow, J. M. Townsend, and M. S. Detamore, "The ogden model for hydrogels in tissue engineering: modulus determination with compression to failure," *J. Biomech.*, vol. 152, no. 0021–9290, pp. 111592–111599, 2023.

[32] D. S. Nedrelow *et al.*, "Regenerative engineering of a biphasic patient-fitted temporomandibular joint condylar prosthesis," *Tissue Eng. Part C Methods*, vol. 29, no. 7, pp. 307–320, Jul. 2023, doi: 10.1089/ten.tec.2023.0093.

[33] W. Zhang *et al.*, "The effect of interface microstructure on interfacial shear strength for osteochondral scaffolds based on biomimetic design and 3D printing," *Mater. Sci. Eng. C*, vol. 46, pp. 10–15, Jan. 2015, doi: 10.1016/j.msec.2014.09.042.

[34] J. Lo, L. Chan, and S. Flynn, "A systematic review of the incidence, prevalence, costs, and activity/work limitations of amputation, osteoarthritis, rheumatoid arthritis, back pain, multiple sclerosis, spinal cord injury, stroke, and traumatic brain injury in the united states: a 2019 update," *Arch Phys Med Rehabil*, vol. 102, no. 1, pp. 115–131, 2022, doi: 10.1016/j.apmr.2020.04.001.A.

[35] C. L. Camp, M. J. Stuart, and A. J. Krych, "Current concepts of articular cartilage restoration techniques in the knee," *Sports Health*, vol. 6, no. 3, pp. 265–273, 2014, doi: 10.1177/1941738113508917.

[36] Y. Zhang and J. M. Jordan, "Epidemiology of osteoarthritis," *Clin. Geriatr. Med.*, vol. 26, no. 3, pp. 355–369, 2010, doi: 10.1016/j.cger.2010.03.001.

[37] M. Sloan, A. Premkumar, and N. P. Sheth, "Projected volume of primary total joint arthroplasty in the u.s., 2014 to 2030," *J. Bone Jt. Surg.*, vol. 100, no. 17, pp. 1455–60, 2018, doi: http://dx.doi.org/10.2106/JBJS.17.01617.

[38] N. H. Dormer, C. J. Berkland, and M. S. Detamore, "Emerging techniques in stratified designs and continuous gradients for tissue engineering of interfaces," *Ann. Biomed. Eng.*, vol. 38, no. 6, pp. 2121–2141, 2010, doi: 10.1007/s10439-010-0033-3.

[39] S. Patel *et al.*, "Integrating soft and hard tissues via interface tissue engineering," *J. Orthop. Res.*, vol. 36, no. 4, pp. 1069–1077, 2018, doi: 10.1002/jor.23810.

[40] N. Yildirim, A. Amanzhanova, G. Kulzhanova, F. Mukasheva, and C. Erisken, "Osteochondral interface: regenerative engineering and challenges," *ACS Biomater. Sci. Eng.*, vol. 9, no. 3, pp. 1205–1223, Mar. 2023, doi: 10.1021/acsbiomaterials.2c01321.

[41] N. H. Dormer, C. J. Berkland, and M. S. Detamore, "Emerging techniques in stratified designs and continuous gradients for tissue engineering of interfaces," *Ann. Biomed. Eng.*, vol. 38, no. 6, pp. 2121–2141, Jun. 2010, doi: 10.1007/s10439-010-0033-3.

[42] R. Choe, E. Devoy, E. Jabari, J. D. Packer, and J. P. Fisher, "Biomechanical aspects of osteochondral regeneration: implications and strategies for three-dimensional bioprinting," *Tissue Eng. Part B Rev.*, vol. 28, no. 4, pp. 766–788, Aug. 2022, doi: 10.1089/ten.teb.2021.0101.

[43] M. Tamaddon, H. Gilja, L. Wang, X. S. , J. Miguel Oliveira3, R. Tan, and C. Liu, "Osteochondral scaffolds for early treatment of cartilage defects in osteoarthritic joints: from bench to clinic," *Biomater. Transl.*, vol. 1, no. 1, pp. 3–17, 2020.

[44] S. E. Doyle *et al.*, "3d printed multiphasic scaffolds for osteochondral repair: challenges and opportunities," *Int. J. Mol. Sci.*, vol. 22, no. 22, p. 12420, Nov. 2021, doi: 10.3390/ijms222212420.

[45] F. Gao *et al.*, "Direct 3d printing of high strength biohybrid gradient hydrogel scaffolds for efficient repair of osteochondral defect," *Adv. Funct. Mater.*, vol. 28, no. 13, pp. 1–13, 2018, doi: 10.1002/adfm.201706644.

[46] M. Kuzucu *et al.*, "Extrusion-based 3d bioprinting of gradients of stiffness, cell density, and immobilized peptide using thermogelling hydrogels," *ACS Biomater. Sci. Eng.*, vol. 7, no. 6, pp. 2192–2197, Jun. 2021, doi: 10.1021/acsbiomaterials.1c00183.

[47] K. Willson and A. Atala, "Medical 3d printing: tools and techniques, today and tomorrow," *Annu. Rev. Chem. Biomol. Eng.*, vol. 13, no. 1, pp. 481–499, Jun. 2022, doi: 10.1146/annurev-chembioeng-092220-015404.

[48] S. E. Doyle *et al.*, "3d printed multiphasic scaffolds for osteochondral repair: challenges and opportunities," *Int. J. Mol. Sci.*, vol. 22, no. 22, p. 12420, Nov. 2021, doi: 10.3390/ijms222212420.

[49] D. Ege and V. Hasirci, "Is 3d printing promising for osteochondral tissue regeneration?," *ACS Appl. Bio Mater.*, vol. 6, no. 4, pp. 1431–1444, Apr. 2023, doi: 10.1021/acsabm.3c00093.

[50] S. Wang, S. Zhao, J. Yu, Z. Gu, and Y. Zhang, "Advances in translational 3d printing for cartilage, bone, and osteochondral tissue engineering," *Small*, vol. 18, no. 36, p. 2201869, Sep. 2022, doi: 10.1002/smll.202201869.

[51] Y. Hao *et al.*, "3d printing hip prostheses offer accurate reconstruction, stable fixation, and functional recovery for revision total hip arthroplasty with complex acetabular bone defect," *Engineering*, vol. 6, no. 11, pp. 1285–1290, 2020.

[52] M. Di Prima, J. Coburn, D. Hwang, J. Kelly, A. Khairuzzaman, and L. Ricles, "Additively manufactured medical products – the FDA perspective," *3D Print. Med.*, vol. 2, no. 1, p. 1, Dec. 2016, doi: 10.1186/s41205-016-0005-9.

[53] N. Yildirim, A. Amanzhanova, G. Kulzhanova, F. Mukasheva, and C. Erisken, "Osteochondral interface: regenerative engineering and challenges," *ACS Biomater. Sci. Eng.*, vol. 9, no. 3, pp. 1205–1223, Mar. 2023, doi: 10.1021/acsbiomaterials.2c01321.

[54] R. F. Faidallah, M. M. Hanon, Z. Szakál, and I. Oldal, "Biodegradable materials used in fdm 3d printing technology: a critical review," *J. Mod. Mech. Eng. Technol.*, vol. 9, pp. 90–105, Dec. 2022, doi: 10.31875/2409-9848.2022.09.11.

[55] S. Chae and D.-W. Cho, "Biomaterial-based 3D bioprinting strategy for orthopedic tissue engineering," *Acta Biomater.*, vol. 156, pp. 4–20, Jan. 2023, doi: 10.1016/j.actbio.2022.08.004.

[56] E. H. Tümer and H. Y. Erbil, "Extrusion-based 3d printing applications of pla composites: a review," *Coatings*, vol. 11, no. 4, p. 390, Mar. 2021, doi: 10.3390/coatings11040390.

[57] Z. U. Arif, M. Y. Khalid, R. Noroozi, A. Sadeghianmaryan, M. Jalalvand, and M. Hossain, "Recent advances in 3D-printed polylactide and polycaprolactone-based biomaterials for tissue engineering applications," *Int. J. Biol. Macromol.*, vol. 218, pp. 930–968, Oct. 2022, doi: 10.1016/j.ijbiomac.2022.07.140.

[58] H. Tetsuka and S. R. Shin, "Materials and technical innovations in 3D printing in biomedical applications," *J. Mater. Chem. B*, vol. 8, no. 15, pp. 2930–2950, 2020, doi: 10.1039/D0TB00034E.

[59] J. Li *et al.*, "3D printing for regenerative medicine: From bench to bedside," *MRS Bull.*, vol. 40, no. 2, pp. 145–154, Feb. 2015, doi: 10.1557/mrs.2015.5.

[60] Q. Yan *et al.*, "A review of 3d printing technology for medical applications," *Engineering*, vol. 4, no. 5, pp. 729–742, Oct. 2018, doi: 10.1016/j.eng.2018.07.021.

[61] L. F. Velásquez-García and Y. Kornbluth, "Biomedical applications of metal 3d printing," *Annu. Rev. Biomed. Eng.*, vol. 23, no. 1, pp. 307–338, Jul. 2021, doi: 10.1146/annurev-bioeng-082020-032402.

[62] H. Gao *et al.*, "Porous tantalum scaffolds: fabrication, structure, properties, and orthopedic applications," *Mater. Des.*, vol. 210, p. 110095, Nov. 2021, doi: 10.1016/j.matdes.2021.110095.

[63] S. M. Bittner, J. L. Guo, A. Melchiorri, and A. G. Mikos, "Three-dimensional printing of multilayered tissue engineering scaffolds," *Mater. Today*, vol. 21, no. 8, pp. 861–874, Oct. 2018, doi: 10.1016/j.mattod.2018.02.006.

[64] A. B. Mt. Natarajan, V. Ph. D. Sivadas, and P. D. Ph. D. Nair, "3D-printed biphasic scaffolds for the simultaneous regeneration of osteochondral tissues," *Biomed. Mater.*, vol. 16, no. 5, p. 054102, Sep. 2021, doi: 10.1088/1748-605X/ac14cb.

[65] X. Niu, N. Li, Z. Du, and X. Li, "Integrated gradient tissue-engineered osteochondral scaffolds: Challenges, current efforts and future perspectives," *Bioact. Mater.*, vol. 20, pp. 574–597, Feb. 2023, doi: 10.1016/j.bioactmat.2022.06.011.

[66] D. Kilian, T. Ahlfeld, A. R. Akkineni, A. Bernhardt, M. Gelinsky, and A. Lode, "3D Bioprinting of osteochondral tissue substitutes – in vitro-chondrogenesis in multi-

layered mineralized constructs," *Sci. Rep.*, vol. 10, no. 1, p. 8277, May 2020, doi: 10.1038/s41598-020-65050-9.

[67] Y. Du *et al.*, "Selective laser sintering scaffold with hierarchical architecture and gradient composition for osteochondral repair in rabbits," *Biomaterials*, vol. 137, pp. 37–48, Aug. 2017, doi: 10.1016/j.biomaterials.2017.05.021.

[68] G. L. Koons, P. D. Kontoyiannis, M. Diba, L. K. Chim, D. W. Scott, and A. G. Mikos, "Effect of 3d printing temperature on bioactivity of bone morphogenetic protein-2 released from polymeric constructs," *Ann. Biomed. Eng.*, vol. 49, no. 9, pp. 2114–2125, Sep. 2021, doi: 10.1007/s10439-021-02736-9.

[69] R. Choe, E. Devoy, E. Jabari, J. D. Packer, and J. P. Fisher, "Biomechanical Aspects of Osteochondral Regeneration: Implications and Strategies for Three-Dimensional Bioprinting," *Tissue Eng. Part B Rev.*, vol. 00, no. 00, 2021, doi: 10.1089/ten.teb.2021.0101.

[70] H. Suo, Y. Chen, J. Liu, L. Wang, and M. Xu, "3D printing of biphasic osteochondral scaffold with sintered hydroxyapatite and polycaprolactone," *J. Mater. Sci.*, vol. 56, no. 29, pp. 16623–16633, Oct. 2021, doi: 10.1007/s10853-021-06229-x.

[71] M. Altunbek, F. Afghah, O. S. Caliskan, J. J. Yoo, and B. Koc, "Design and bioprinting for tissue interfaces," *Biofabrication*, vol. 15, no. 2, p. 022002, Apr. 2023, doi: 10.1088/1758-5090/acb73d.

[72] S. M. Bittner *et al.*, "Fabrication and mechanical characterization of 3D printed vertical uniform and gradient scaffolds for bone and osteochondral tissue engineering," *Acta Biomater.*, vol. 90, pp. 37–48, May 2019, doi: 10.1016/j.actbio.2019.03.041.

[73] S. Zhang, Q. Li, P. Liu, C. Lin, Z. Tang, and H.-L. Wang, "Three-dimensional cell printed lock-key structure for oral soft and hard tissue regeneration," *Tissue Eng. Part A*, vol. 28, no. 1–2, pp. 13–26, Jan. 2022, doi: 10.1089/ten.tea.2021.0022.

[74] N. D. Broom, A. Oloyede, R. Flachsmann, and M. Hows, "Dynamic fracture characteristics of the osteochondral junction undergoing shear deformation," *Med. Eng. Phys.*, vol. 18, no. 5, pp. 396–404, 1996, doi: 10.1016/1350-4533(95)00067-4.

[75] E. R. Flachsmann, N. D. Broom, and A. Oloyede, "A biomechanical investigation of unconstrained shear failure of the osteochondral region under impact loading," *Clin Biomech*, vol. 10, no. 3, pp. 156–165, 1995.

[76] J. Lee *et al.*, "Composite spheroid-laden bilayer hydrogel for engineering three-dimensional osteochondral tissue," *Tissue Eng. Part A*, p. ten.tea.2023.0299, Jan. 2024, doi: 10.1089/ten.tea.2023.0299.

[77] A. Motealleh, P. Dorri, A. H. Schäfer, and N. S. Kehr, "3D bioprinting of triphasic nanocomposite hydrogels and scaffolds for cell adhesion and migration," *Biofabrication*, vol. 11, no. 3, 2019, doi: 10.1088/1758-5090/ab15ca.

[78] A. Di Luca *et al.*, "Surface energy and stiffness discrete gradients in additive manufactured scaffolds for osteochondral regeneration," *Biofabrication*, vol. 8, no. 1, 2016, doi: 10.1088/1758-5090/8/1/015014.

[79] L. Chen *et al.*, "3D printing of a lithium-calcium-silicate crystal bioscaffold with dual bioactivities for osteochondral interface reconstruction," *Biomaterials*, vol. 196, pp. 138–150, 2019, doi: 10.1016/j.biomaterials.2018.04.005.

[80] M. Zhu, X. He, C. Xin, Y. Zhu, and Z. Liu, "3D printing of an integrated triphasic MBG-alginate scaffold with enhanced interface bonding for hard tissue applications," *J. Mater. Sci. Mater. Med.*, vol. 31, no. 12, 2020, [Online]. Available: http://dx.doi.org/10.1007/s10856-020-06459-6

[81] W. Wei and H. Dai, "Articular cartilage and osteochondral tissue engineering techniques: Recent advances and challenges," *Bioact. Mater.*, vol. 6, no. 12, pp. 4830–4855, 2021, doi: 10.1016/j.bioactmat.2021.05.011.

[82] C. D. Hoemann, C.-H. Lafantaisie-Favreau, V. Lascau-coman, G. Chen, and J. Guzmán-morales, "The Cartilage–Bone Interface," *Articul. Cartil. Inj. Knee Basic Sci. Surg. Repair*, vol. 25, no. 2, pp. 85–98, 2012, doi: 10.1055/b-0034-92479.

[83] M. T. Frassica and M. A. Grunlan, "Perspectives on synthetic materials to guide tissue regeneration for osteochondral defect repair," *ACS Biomater. Sci. Eng.*, vol. 6, no. 8, pp. 4324–4336, 2020, doi: 10.1021/acsbiomaterials.0c00753.

[84] V. B. Sitterle, W. Sun, and M. E. Levenston, "A modified lap test to more accurately estimate interfacial shear strength for bonded tissues," *J. Biomech.*, vol. 41, no. 15, pp. 3260–3264, Nov. 2008, doi: 10.1016/j.jbiomech.2008.09.006.

[85] J. Liu *et al.*, "Fatigue-resistant adhesion of hydrogels," *Nat. Commun.*, vol. 11, no. 1, p. 1071, Feb. 2020, doi: 10.1038/s41467-020-14871-3.

[86] C. Yu, H. Gao, Q. Li, and X. Cao, "Injectable dual cross-linked adhesive hyaluronic acid multifunctional hydrogel scaffolds for potential applications in cartilage repair," *Polym. Chem.*, vol. 11, no. 18, pp. 3169–3178, 2020, doi: 10.1039/D0PY00371A.

[87] L. Romito and G. A. Ameer, "Mechanical interlocking of engineered cartilage to an underlying polymeric substrate: towards a biohybrid tissue equivalent," *Ann. Biomed. Eng.*, vol. 34, no. 5, pp. 737–747, May 2006, doi: 10.1007/s10439-006-9089-5.

[88] C. Scotti *et al.*, "Engineering human cell-based, functionally integrated osteochondral grafts by biological bonding of engineered cartilage tissues to bony scaffolds," *Biomaterials*, vol. 31, no. 8, pp. 2252–2259, Mar. 2010, doi: 10.1016/j.biomaterials.2009.11.110.

[89] W. E. Brown, B. J. Huang, J. C. Hu, and K. A. Athanasiou, "Engineering large, anatomically shaped osteochondral constructs with robust interfacial shear properties," *Npj Regen. Med.*, vol. 6, no. 1, p. 42, Aug. 2021, doi: 10.1038/s41536-021-00152-0.

[90] D. J. Hamilton, C. A. Séguin, J. Wang, R. M. Pilliar, and R. A. Kandel, "Formation of a nucleus pulposus-cartilage endplate construct in vitro," *Biomaterials*, vol. 27, no. 3, pp. 397–405, Jan. 2006, doi: 10.1016/j.biomaterials.2005.07.007.

[91] K. S. Allan, R. M. Pilliar, J. Wang, M. D. Grynpas, and R. A. Kandel, "Formation of biphasic constructs containing cartilage with a calcified zone interface," *Tissue Eng.*, vol. 13, no. 1, pp. 167–177, Jan. 2007, doi: 10.1089/ten.2006.0081.

[92] L. Wang, L. Zhao, and M. S. Detamore, "Human umbilical cord mesenchymal stromal cells in a sandwich approach for osteochondral tissue engineering," *J. Tissue Eng. Regen. Med.*, vol. 5, no. 9, pp. 712–721, Oct. 2011, doi: 10.1002/term.370.

[93] E. S. Reindel, A. M. Ayroso, A. C. Chen, D. M. Chun, R. M. Schinagl, and R. L. Sah, "Integrative repair of articular cartilage *in vitro* : Adhesive strength of the interface

region," *J. Orthop. Res.*, vol. 13, no. 5, pp. 751–760, Sep. 1995, doi: 10.1002/jor.1100130515.

[94] L. Romito and G. A. Ameer, "Mechanical interlocking of engineered cartilage to an underlying polymeric substrate: towards a biohybrid tissue equivalent," *Ann. Biomed. Eng.*, vol. 34, no. 5, pp. 737–747, May 2006, doi: 10.1007/s10439-006-9089-5.

[95] E. G. Lima *et al.*, "The effect of devitalized trabecular bone on the formation of osteochondral tissue-engineered constructs," *Biomaterials*, vol. 29, no. 32, pp. 4292–4299, Nov. 2008, doi: 10.1016/j.biomaterials.2008.07.018.

[96] E. G. Lima *et al.*, "The effect of devitalized trabecular bone on the formation of osteochondral tissue-engineered constructs," *Biomaterials*, vol. 29, no. 32, pp. 4292–4299, Nov. 2008, doi: 10.1016/j.biomaterials.2008.07.018.

[97] A. B. Nover *et al.*, "Porous titanium bases for osteochondral tissue engineering," *Acta Biomater.*, vol. 27, pp. 286–293, Nov. 2015, doi: 10.1016/j.actbio.2015.08.045.

[98] C. Li *et al.*, "Integrated and bifunctional bilayer 3d printing scaffold for osteochondral defect repair," *Adv. Funct. Mater.*, vol. 33, no. 20, p. 2214158, May 2023, doi: 10.1002/adfm.202214158.

[99] L. Yu, S. Cavelier, B. Hannon, and M. Wei, "Recent development in multizonal scaffolds for osteochondral regeneration," *Bioact. Mater.*, vol. 25, pp. 122–159, Jul. 2023, doi: 10.1016/j.bioactmat.2023.01.012.

[100] J. Xu *et al.*, "3d printing for bone-cartilage interface regeneration," *Front. Bioeng. Biotechnol.*, vol. 10, p. 828921, Feb. 2022, doi: 10.3389/fbioe.2022.828921.

[101] H. Lv *et al.*, "A novel 3D-printed device for localization and extraction of trabeculae from human femoral heads: a comparison with traditional visual extraction," *Osteoporos. Int.*, vol. 26, no. 6, pp. 1791–1799, Jun. 2015, doi: 10.1007/s00198-015-3058-5.

[102] S. Wang, S. Zhao, J. Yu, Z. Gu, and Y. Zhang, "Advances in translational 3d printing for cartilage, bone, and osteochondral tissue engineering," *Small*, vol. 18, no. 36, p. 2201869, Sep. 2022, doi: 10.1002/smll.202201869.

[103] F. X. Koeck, J. Beckmann, C. Luring, B. Rath, J. Grifka, and E. Basad, "Evaluation of implant position and knee alignment after patient-specific unicompartmental knee arthroplasty," *The Knee*, vol. 18, no. 5, pp. 294–299, Oct. 2011, doi: 10.1016/j.knee.2010.06.008.

[104] C. R. Alcala-Orozco, X. Cui, G. J. Hooper, K. S. Lim, and T. B. F. Woodfield, "Converging functionality: Strategies for 3D hybrid-construct biofabrication and the role of composite biomaterials for skeletal regeneration," *Acta Biomater.*, vol. 132, pp. 188–216, Sep. 2021, doi: 10.1016/j.actbio.2021.03.008.

[105] N. A. Sears, D. R. Seshadri, P. S. Dhavalikar, and E. Cosgriff-Hernandez, "A review of three-dimensional printing in tissue engineering," *Tissue Eng. Part B Rev.*, vol. 22, no. 4, pp. 298–310, Aug. 2016, doi: 10.1089/ten.teb.2015.0464.

[106] N. Arifin, I. Sudin, N. H. A. Ngadiman, and M. S. A. Ishak, "A comprehensive review of biopolymer fabrication in additive manufacturing processing for 3d-tissue-engineering scaffolds," *Polymers*, vol. 14, no. 10, p. 2119, May 2022, doi: 10.3390/polym14102119.

[107] R. Choe *et al.*, "Computational investigation of interface printing patterns within 3D printed multilayered scaffolds for osteochondral tissue engineering," *Biofabrication*, vol. 14, no. 2, p. 025015, Apr. 2022, doi: 10.1088/1758-5090/ac5220.

[108] P. Diloksumpan *et al.*, "Combining multi-scale 3D printing technologies to engineer reinforced hydrogel-ceramic interfaces," *Biofabrication*, vol. 12, no. 2, p. 025014, Apr. 2020, doi: 10.1088/1758-5090/ab69d9.

[109] Y. Shanjani, C. C. Pan, L. Elomaa, and Y. Yang, "A novel bioprinting method and system for forming hybrid tissue engineering constructs," *Biofabrication*, vol. 7, no. 4, 2015, doi: 10.1088/1758-5090/7/4/045008.

[110] B. Holmes, W. Zhu, J. Li, J. D. Lee, and L. G. Zhang, "Development of novel three-dimensional printed scaffolds for osteochondral regeneration," *Tissue Eng. - Part A*, vol. 21, no. 1–2, pp. 403–415, 2015, doi: 10.1089/ten.tea.2014.0138.

[111] D. Schaefer *et al.*, "Tissue-engineered composites for the repair of large osteochondral defects," *Arthritis Rheum.*, vol. 46, no. 9, pp. 2524–2534, Sep. 2002, doi: 10.1002/art.10493.

[112] I. Khan, S. Gilbert, S. Singhrao, V. Duance, and C. Archer, "Evaluation of the reasons for failure of integration during cartilage repair. A review," *Eur. Cell. Mater.*, vol. 16, pp. 26–39, Sep. 2008, doi: 10.22203/eCM.v016a04.

[113] D. H. Ballard, P. Mills, R. Duszak, J. A. Weisman, F. J. Rybicki, and P. K. Woodard, "Medical 3d printing cost-savings in orthopedic and maxillofacial surgery: cost analysis of operating room time saved with 3d printed anatomic models and surgical guides," *Acad. Radiol.*, vol. 27, no. 8, pp. 1103–1113, Aug. 2020, doi: 10.1016/j.acra.2019.08.011.

[114] N. Bizzotto *et al.*, "3D Printed replica of articular fractures for surgical planning and patient consent: a two years multi-centric experience," *3D Print. Med.*, vol. 2, no. 1, p. 2, Dec. 2016, doi: 10.1186/s41205-016-0006-8.

[115] S.-J. Yoo *et al.*, "3D printing in medicine of congenital heart diseases," *3D Print. Med.*, vol. 2, no. 1, p. 3, Dec. 2016, doi: 10.1186/s41205-016-0004-x.

[116] S. Rhee, J. L. Puetzer, B. N. Mason, C. A. Reinhart-King, and L. J. Bonassar, "3d bioprinting of spatially heterogeneous collagen constructs for cartilage tissue engineering," *ACS Biomater. Sci. Eng.*, vol. 2, no. 10, pp. 1800–1805, 2016, doi: 10.1021/acsbiomaterials.6b00288.

[117] L. Roseti *et al.*, "Scaffolds for Bone Tissue Engineering: State of the art and new perspectives," *Mater. Sci. Eng. C*, vol. 78, pp. 1246–1262, Sep. 2017, doi: 10.1016/j.msec.2017.05.017.

[118] F. Wang, Y. Sun, D. He, and L. Wang, "Effect of concentrated growth factors on the repair of the goat temporomandibular joint," *J. Oral Maxillofac. Surg.*, vol. 75, no. 3, pp. 498–507, Mar. 2017, doi: 10.1016/j.joms.2016.09.006.

[119] L. Zhou *et al.*, "Engineering ear constructs with a composite scaffold to maintain dimensions," *Tissue Eng. Part A*, vol. 17, no. 11–12, pp. 1573–1581, Jun. 2011, doi: 10.1089/ten.tea.2010.0627.

[120] T. Mesallati, E. Sheehy, T. Vinardell, C. Buckley, and D. Kelly, "Tissue engineering scaled-up, anatomically shaped osteochondral constructs for joint resurfacing," *Eur. Cell. Mater.*, vol. 30, pp. 163–186, Sep. 2015, doi: 10.22203/eCM.v030a12.

[121] S. Scheurer, "3D Bioprinting of anatomically accurate Implants for Meniscus Tissue Engineering," Trinity College Dublin, 2020.

[122] C. Ding *et al.*, "Regeneration of a goat femoral head using a tissue-specific, biphasic scaffold fabricated with CAD/CAM technology," *Biomaterials*, vol. 34, no. 28, pp. 6706–6716, Sep. 2013, doi: 10.1016/j.biomaterials.2013.05.038.

[123] G. Haghiashtiani *et al.*, "3D printed patient-specific aortic root models with internal sensors for minimally invasive applications," *Sci. Adv.*, vol. 6, no. 35, pp. 4641–4653, Aug. 2020, doi: 10.1126/sciadv.abb4641.

[124] F. Wang, Y. Hu, D. He, G. Zhou, X. Yang, and E. Ellis, "Regeneration of subcutaneous tissue-engineered mandibular condyle in nude mice," *J. Cranio-Maxillofac. Surg.*, vol. 45, no. 6, pp. 855–861, Jun. 2017, doi: 10.1016/j.jcms.2017.03.017.

[125] J.-H. Shim, J.-S. Lee, J. Y. Kim, and D.-W. Cho, "Bioprinting of a mechanically enhanced three-dimensional dual cell-laden construct for osteochondral tissue engineering using a multi-head tissue/organ building system," *J. Micromechanics Microengineering*, vol. 22, no. 8, p. 085014, Aug. 2012, doi: 10.1088/0960-1317/22/8/085014.

[126] A. C. Daly and D. J. Kelly, "Biofabrication of spatially organised tissues by directing the growth of cellular spheroids within 3D printed polymeric microchambers," *Biomaterials*, vol. 197, pp. 194–206, Mar. 2019, doi: 10.1016/j.biomaterials.2018.12.028.

[127] J. Visser *et al.*, "Biofabrication of multi-material anatomically shaped tissue constructs," *Biofabrication*, vol. 5, no. 3, pp. 035007–035016, 2013, doi: 10.1088/1758-5082/5/3/035007.

[128] C. H. Lee, N. W. Marion, S. Hollister, and J. J. Mao, "Tissue formation and vascularization in anatomically shaped human joint condyle ectopically *in vivo*," *Tissue Eng. Part A*, vol. 15, no. 12, pp. 3923–3930, Dec. 2009, doi: 10.1089/ten.tea.2008.0653.

[129] F. Rengier *et al.*, "3D printing based on imaging data: review of medical applications," *Int. J. Comput. Assist. Radiol. Surg.*, vol. 5, no. 4, pp. 335–341, Jul. 2010, doi: 10.1007/s11548-010-0476-x.

[130] D. Ege and V. Hasirci, "Is 3d printing promising for osteochondral tissue regeneration?," *ACS Appl. Bio Mater.*, vol. 6, no. 4, pp. 1431–1444, Apr. 2023, doi: 10.1021/acsabm.3c00093.

[131] W. H. Douglas, "Clinical status of dentine bonding agents," *J. Dent.*, vol. 17, no. 5, pp. 209–215, Oct. 1989, doi: 10.1016/0300-5712(89)90166-8.

[132] Y. Li *et al.*, "Fatigue failure of dentin–composite disks subjected to cyclic diametral compression," *Dent. Mater.*, vol. 31, no. 7, pp. 778–788, Jul. 2015, doi: 10.1016/j.dental.2015.03.014.

[133] F. L. Esteban Florez *et al.*, "Antibacterial dental adhesive resins containing nitrogen-doped titanium dioxide nanoparticles," *Mater. Sci. Eng. C*, vol. 93, pp. 931–943, Dec. 2018, doi: 10.1016/j.msec.2018.08.060.

[134] B. T. Schneider, M. A. Baumann, L. G. Watanabe, and G. W. Marshall, "Dentin shear bond strength of compomers and composites," *Dent. Mater.*, vol. 16, no. 1, pp. 15–19, Jan. 2000, doi: 10.1016/S0109-5641(99)00078-0.

[135] W. Liang *et al.*, "Recent advances in 3D printing of biodegradable metals for orthopaedic applications," *J. Biol. Eng.*, vol. 17, no. 1, p. 56, Aug. 2023, doi: 10.1186/s13036-023-00371-7.

[136] K. C. Wong, "3D-printed patient-specific applications in orthopedics," *Orthop. Res. Rev.*, vol. Volume 8, pp. 57–66, Oct. 2016, doi: 10.2147/ORR.S99614.

[137] S. Trainor, J. Collins, H. Mulvey, and W. Fitz, "Total knee replacement sizing: shoe size is a better predictor for implant size than body height," . *NUMBER*, vol. 6, no. 2, 2018.

[138] S. A. Schoonraad *et al.*, "Biomimetic and mechanically supportive 3D printed scaffolds for cartilage and osteochondral tissue engineering using photopolymers and digital light processing," *Biofabrication*, vol. 13, no. 4, p. 044106, Oct. 2021, doi: 10.1088/1758-5090/ac23ab.

[139] J. A. Brown *et al.*, "Patient–specific immersed finite element–difference model of transcatheter aortic valve replacement," *Ann. Biomed. Eng.*, vol. 51, no. 1, pp. 103–116, Jan. 2023, doi: 10.1007/s10439-022-03047-3.

[140] R. J. Morrison *et al.*, "Regulatory considerations in the design and manufacturing of implantable 3d-printed medical devices," *Clin. Transl. Sci.*, vol. 8, no. 5, pp. 594–600, Oct. 2015, doi: 10.1111/cts.12315.

[141] O. of the Commissioner, "Strategic plan for regulatory science," *FDA*, Dec. 2020, Accessed: May 10, 2024. [Online]. Available: https://www.fda.gov/science-research/advancing-regulatory-science/strategic-plan-regulatory-science

[142] "Recognized Consensus Standards: Medical Devices." Accessed: May 16, 2024. [Online]. Available: https://www.accessdata.fda.gov/scripts/cdrh/cfdocs/cfstandards/detail.cfm?standard__identification_no=40777

[143] C. W. Imhauser *et al.*, "Reproducibility in modeling and simulation of the knee: Academic, industry, and regulatory perspectives," *J. Orthop. Res.*, vol. 41, no. 12, pp. 2569–2578, 2023, doi: 10.1002/jor.25652.

[144] S. M. Giannitelli, D. Accoto, M. Trombetta, and A. Rainer, "Current trends in the design of scaffolds for computer-aided tissue engineering," *Acta Biomater.*, vol. 10, no. 2, pp. 580–594, Feb. 2014, doi: 10.1016/j.actbio.2013.10.024.

[145] S. P. Väänänen *et al.*, "Automated segmentation of cortical and trabecular bone to generate finite element models for femoral bone mechanics," *Med. Eng. Phys.*, vol. 70, pp. 19–28, Aug. 2019, doi: 10.1016/j.medengphy.2019.06.015.

[146] T. Oláh *et al.*, "Quantifying the human subchondral trabecular bone microstructure in osteoarthritis with clinical ct," *Adv. Sci.*, vol. 9, no. 23, p. 2201692, Aug. 2022, doi: 10.1002/advs.202201692.

[147] J. Hsieh and T. Flohr, "Computed tomography recent history and future perspectives," *J. Med. Imaging*, vol. 8, no. 05, Aug. 2021.

[148] D. Liu *et al.*, "The use of a 3D-printed individualized navigation template to assist in the anatomical reconstruction surgery of the anterior cruciate ligament," *Ann. Transl. Med.*, vol. 8, no. 24, pp. 1656–1656, Dec. 2020, doi: 10.21037/atm-20-7515.

[149] J. P. Van Den Bergh, P. Szulc, A. M. Cheung, M. Bouxsein, K. Engelke, and R. Chapurlat, "The clinical application of high-resolution peripheral computed tomography (HR-pQCT) in adults: state of the art and future directions,"

Osteoporos. Int., vol. 32, no. 8, pp. 1465–1485, Aug. 2021, doi: 10.1007/s00198-021-05999-z.

[150] T. Oláh *et al.*, "Quantifying the human subchondral trabecular bone microstructure in osteoarthritis with clinical ct," *Adv. Sci.*, vol. 9, no. 23, p. 2201692, Aug. 2022, doi: 10.1002/advs.202201692.

[151] J. M. Patel, B. C. Wise, E. D. Bonnevie, and R. L. Mauck, "A systematic review and guide to mechanical testing for articular cartilage tissue engineering," *Tissue Eng. Part C Methods*, vol. 25, no. 10, pp. 593–608, Oct. 2019, doi: 10.1089/ten.tec.2019.0116.

[152] A. T. Collins *et al.*, "Obesity alters the in vivo mechanical response and biochemical properties of cartilage as measured by MRI," *Arthritis Res. Ther.*, vol. 20, no. 1, p. 232, Dec. 2018, doi: 10.1186/s13075-018-1727-4.

[153] R. Long and C.-Y. Hui, "Fracture toughness of hydrogels: measurement and interpretation," *Soft Matter*, vol. 12, no. 39, pp. 8069–8086, 2016, doi: 10.1039/C6SM01694D.

[154] Y. Xiao, E. A. Friis, S. H. Gehrke, and M. S. Detamore, "Mechanical testing of hydrogels in cartilage tissue engineering: beyond the compressive modulus," *Tissue Eng. Part B Rev.*, vol. 19, no. 5, pp. 403–412, Oct. 2013, doi: 10.1089/ten.teb.2012.0461.

[155] M. T. J. J. M. Punter, B. E. Vos, B. M. Mulder, and G. H. Koenderink, "Poroelasticity of (bio)polymer networks during compression: theory and experiment," *Soft Matter*, vol. 16, no. 5, pp. 1298–1305, 2020, doi: 10.1039/C9SM01973A.

[156] G. Saccomandi, L. Vergori, and E. M. Zanetti, "Linear, weakly nonlinear and fully nonlinear models for soft tissues: which ones provide the most reliable estimations of the stiffness?," *Philos. Trans. R. Soc. Math. Phys. Eng. Sci.*, vol. 380, no. 2234, p. 20210321, Oct. 2022, doi: 10.1098/rsta.2021.0321.

[157] F. J. Vernerey, E. C. Greenwald, and S. J. Bryant, "Triphasic mixture model of cell-mediated enzymatic degradation of hydrogels," *Comput. Methods Biomech. Biomed. Engin.*, vol. 15, no. 11, pp. 1197–1210, Nov. 2012, doi: 10.1080/10255842.2011.585973.

[158] A. Weizel *et al.*, "Hyperelastic parameter identification of human articular cartilage and substitute materials," *J. Mech. Behav. Biomed. Mater.*, vol. 133, p. 105292, Sep. 2022, doi: 10.1016/j.jmbbm.2022.105292.

[159] R. W. Ogden, "Large deformation isotropic elasticity - on the correlation of theory and experiment for incompressible rubberlike solids," *Proc. R. Soc. Lond. A*, vol. 326, pp. 565–584, 1972.

[160] M. Destrade, L. Dorfmann, and G. Saccomandi, "The Ogden model of rubber mechanics: 50 years of impact on nonlinear elasticity," *Philos. Trans. R. Soc. Math. Phys. Eng. Sci.*, vol. 380, no. 2234, p. 20210332, Oct. 2022, doi: 10.1098/rsta.2021.0332.

[161] S. Budday, T. C. Ovaert, G. A. Holzapfel, P. Steinmann, and E. Kuhl, "Fifty shades of brain: a review on the mechanical testing and modeling of brain tissue," *Arch. Comput. Methods Eng.*, vol. 27, no. 4, pp. 1187–1230, Sep. 2020, doi: 10.1007/s11831-019-09352-w.

[162] S. Budday *et al.*, "Mechanical characterization of human brain tissue," *Acta Biomater.*, vol. 48, pp. 319–340, Jan. 2017, doi: 10.1016/j.actbio.2016.10.036.

[163] J. M. Townsend, M. E. Sanders, E. A. Kiyotake, and M. S. Detamore, "Independent control of molecular weight, concentration, and stiffness of hyaluronic acid hydrogels," *Biomed. Mater.*, vol. 17, no. 6, p. 065005, Nov. 2022, doi: 10.1088/1748-605X/ac8e41.

[164] M. D. Godesky and D. I. Shreiber, "Hyaluronic acid-based hydrogels with independently tunable mechanical and bioactive signaling features," *Biointerphases*, vol. 14, no. 6, p. 061005, Nov. 2019, doi: 10.1063/1.5126493.

[165] E. C. Beck *et al.*, "Chondroinduction from naturally derived cartilage matrix: a comparison between devitalized and decellularized cartilage encapsulated in hydrogel pastes," *Tissue Eng. Part A*, vol. 22, no. 7–8, pp. 665–679, Apr. 2016, doi: 10.1089/ten.tea.2015.0546.

[166] E. A. Kiyotake, A. W. Douglas, E. E. Thomas, S. L. Nimmo, and M. S. Detamore, "Development and quantitative characterization of the precursor rheology of hyaluronic acid hydrogels for bioprinting," *Acta Biomater.*, vol. 95, pp. 176–187, Sep. 2019, doi: 10.1016/j.actbio.2019.01.041.

[167] E. A. Kiyotake, M. E. Cheng, E. E. Thomas, and M. S. Detamore, "The rheology and printability of cartilage matrix-only biomaterials," *Biomolecules*, vol. 12, no. 6, p. 846, Jun. 2022, doi: 10.3390/biom12060846.

[168] K. J. Livak and T. D. Schmittgen, "Analysis of relative gene expression data using real-time quantitative PCR and the 2−ΔΔCT method," *Methods*, vol. 25, no. 4, pp. 402–408, Dec. 2001, doi: 10.1006/meth.2001.1262.

[169] R. W. Ogden, "Non-linear elastic deformations," in *Non-linear Elastic Deformations*, Mathematics and its Applications., West Sussex, England: Ellis Horwood Limited, 1984, p. 221.

[170] R. W. Ogden, G. Saccomandi, and I. Sgura, "Fitting hyperelastic models to experimental data," *Comput. Mech.*, vol. 34, no. 6, pp. 484–502, Nov. 2004, doi: 10.1007/s00466-004-0593-y.

[171] C. O. Horgan and J. G. Murphy, "Exponents of the one-term Ogden model: insights from simple shear," *Philos. Trans. R. Soc. Math. Phys. Eng. Sci.*, vol. 380, no. 2234, p. 20210328, Oct. 2022, doi: 10.1098/rsta.2021.0328.

[172] M. Mooney, "A theory of large elastic deformation," *J. Appl. Phys.*, vol. 11, no. 9, pp. 582–592, Sep. 1940, doi: 10.1063/1.1712836.

[173] A. E. Ehret, "On a molecular statistical basis for Ogden's model of rubber elasticity," *J. Mech. Phys. Solids*, vol. 78, pp. 249–268, May 2015, doi: 10.1016/j.jmps.2015.02.006.

[174] H. J. Motulsky and R. E. Brown, "Detecting outliers when fitting data with nonlinear regression – a new method based on robust nonlinear regression and the false discovery rate," *BMC Bioinformatics*, vol. 7, no. 1, p. 123, Dec. 2006, doi: 10.1186/1471-2105-7-123.

[175] M. J. Lohr, G. P. Sugerman, S. Kakaletsis, E. Lejeune, and M. K. Rausch, "An introduction to the Ogden model in biomechanics: benefits, implementation tools and limitations," *Philos. Trans. R. Soc. Math. Phys. Eng. Sci.*, vol. 380, no. 2234, p. 20210365, Oct. 2022, doi: 10.1098/rsta.2021.0365.

[176] B. J. DeKosky *et al.*, "Hierarchically designed agarose and poly(ethylene glycol) interpenetrating network hydrogels for cartilage tissue engineering," *Tissue Eng. Part C Methods*, vol. 16, no. 6, pp. 1533–1542, Dec. 2010, doi: 10.1089/ten.tec.2009.0761.

[177] D. A. Rennerfeldt, A. N. Renth, Z. Talata, S. H. Gehrke, and M. S. Detamore, "Tuning mechanical performance of poly(ethylene glycol) and agarose interpenetrating network hydrogels for cartilage tissue engineering," *Biomaterials*, vol. 34, no. 33, pp. 8241–8257, Nov. 2013, doi: 10.1016/j.biomaterials.2013.07.052.

[178] P. Baei, H. Daemi, F. Mostafaei, F. Azam Sayahpour, H. Baharvand, and M. Baghaban Eslaminejad, "A tough polysaccharide-based cell-laden double-network hydrogel promotes articular cartilage tissue regeneration in rabbits," *Chem. Eng. J.*, vol. 418, p. 129277, Aug. 2021, doi: 10.1016/j.cej.2021.129277.

[179] P. Wang, M. Wu, R. Li, Z. Cai, and H. Zhang, "Fabrication of a double-network hydrogel based on carboxymethylated curdlan/polyacrylamide with highly mechanical performance for cartilage repair," *ACS Appl. Polym. Mater.*, vol. 3, no. 11, pp. 5857–5869, Nov. 2021, doi: 10.1021/acsapm.1c01094.

[180] S. Rathan, L. Dejob, R. Schipani, B. Haffner, M. E. Möbius, and D. J. Kelly, "Fiber reinforced cartilage ecm functionalized bioinks for functional cartilage tissue engineering," *Adv. Healthc. Mater.*, vol. 8, no. 7, p. 1801501, Apr. 2019, doi: 10.1002/adhm.201801501.

[181] V. Morel and T. M. Quinn, "Cartilage injury by ramp compression near the gel diffusion rate," *J. Orthop. Res.*, vol. 22, no. 1, pp. 145–151, Jan. 2004, doi: 10.1016/S0736-0266(03)00164-5.

[182] A. E. Ehret and A. Stracuzzi, "Variations on Ogden's model: close and distant relatives," *Philos. Trans. R. Soc. Math. Phys. Eng. Sci.*, vol. 380, no. 2234, p. 20210322, Oct. 2022, doi: 10.1098/rsta.2021.0322.

[183] V. C. Mow, M. H. Holmes, and W. Michael Lai, "Fluid transport and mechanical properties of articular cartilage: A review," *J. Biomech.*, vol. 17, no. 5, pp. 377–394, Jan. 1984, doi: 10.1016/0021-9290(84)90031-9.

[184] M. A. Soltz and G. A. Ateshian, "A conewise linear elasticity mixture model for the analysis of tension-compression nonlinearity in articular cartilage," *J. Biomech. Eng.*, vol. 122, no. 6, pp. 576–586, Dec. 2000, doi: 10.1115/1.1324669.

[185] N. De Meurechy, A. Braem, and M. Y. Mommaerts, "Biomaterials in temporomandibular joint replacement: current status and future perspectives—a narrative review," *Int. J. Oral Maxillofac. Surg.*, vol. 47, no. 4, pp. 518–533, Apr. 2018, doi: 10.1016/j.ijom.2017.10.001.

[186] A. J. Sidebottom, "Current thinking in temporomandibular joint management," *Br. J. Oral Maxillofac. Surg.*, vol. 47, no. 2, pp. 91–94, Mar. 2009, doi: 10.1016/j.bjoms.2008.08.012.

[187] L. Mercuri, *Temporomandibular joint total joint replacement – tmj tjr*. Springer Cham, 2016. [Online]. Available: https://doi.org/10.1007/978-3-319-21389-7

[188] Louis G. Mercuri, Marco S. Caicedo, "Material hypersensitivity and alloplastic temporomandibular joint replacement," *J. Oral Maxillofac. Surg.*, vol. 77, no. 7, pp. 1371–1376, 2019, doi: https://doi.org/10.1016/j.joms.2019.01.042.

[189] L. G. Mercuri, "Costochondral graft versus total alloplastic joint for temporomandibular joint reconstruction," *Oral Maxillofac. Surg. Clin. N. Am.*, vol. 30, no. 3, pp. 335–342, Aug. 2018, doi: 10.1016/j.coms.2018.05.003.

[190] M. S. Detamore, K. A. Athanasiou, and J. Mao, "A call to action for bioengineers and dental professionals: directives for the future of tmj bioengineering," *Ann. Biomed. Eng.*, vol. 35, no. 8, pp. 1301–1311, Jul. 2007, doi: 10.1007/s10439-007-9298-6.

[191] R. Elledge, L. G. Mercuri, A. Attard, J. Green, and B. Speculand, "Review of emerging temporomandibular joint total joint replacement systems," *Br. J. Oral Maxillofac. Surg.*, vol. 57, no. 8, pp. 722–728, Oct. 2019, doi: 10.1016/j.bjoms.2019.08.009.

[192] L. Wang and M. S. Detamore, "Tissue engineering the mandibular condyle," *Tissue Eng.*, vol. 13, no. 8, pp. 1955–1971, Aug. 2007, doi: 10.1089/ten.2006.0152.

[193] A. J. Almarza *et al.*, "Preclinical animal models for temporomandibular joint tissue engineering," *Tissue Eng. Part B Rev.*, vol. 24, no. 3, pp. 171–178, Jun. 2018, doi: 10.1089/ten.teb.2017.0341.

[194] E. Helgeland, S. Shanbhag, T. O. Pedersen, K. Mustafa, and A. Rosén, "Scaffold-based temporomandibular joint tissue regeneration in experimental animal models: a systematic reviewan abstract of this article was presented as a poster, at the bergen stem cell consortium (bscc), annual meeting, bergen, norway, september 3–4, 2017.," *Tissue Eng. Part B Rev.*, vol. 24, no. 4, pp. 300–316, Aug. 2018, doi: 10.1089/ten.teb.2017.0429.

[195] Chen, David *et al.*, "Tissue engineered autologous cartilage-bone grafts for temporomandibular joint regeneration," *Sci. Transl. Med.*, vol. 12, no. 565, pp. 1–16, 2020.

[196] C. Bifano, G. Hubbard, and W. Ehler, "A comparison of the form and function of the human, monkey, and goat temporomandibular joint," *J. Oral Maxillofac. Surg.*, vol. 52, no. 3, pp. 272–275, Mar. 1994, doi: 10.1016/0278-2391(94)90298-4.

[197] S. Zhu, J. Hu, N. Li, H. Zhou, and E. Luo, "Autogenous coronoid process as a new donor source for reconstruction of mandibular condyle: An experimental study on goats," *Oral Surg. Oral Med. Oral Pathol. Oral Radiol. Endodontology*, vol. 101, no. 5, pp. 572–580, May 2006, doi: 10.1016/j.tripleo.2005.08.023.

[198] C. K. Hagandora, T. W. Chase, and A. J. Almarza, "A comparison of the mechanical properties of the goat temporomandibular joint disc to the mandibular condylar cartilage in unconfined compression," *J. Dent. Biomech.*, vol. 2, no. 1, Dec. 2011, doi: 10.4061/2011/212385.

[199] N. H. Dormer, K. Busaidy, C. J. Berkland, and M. S. Detamore, "Osteochondral interface regeneration of rabbit mandibular condyle with bioactive signal gradients," *J. Oral Maxillofac. Surg.*, vol. 69, no. 6, pp. e50–e57, Jun. 2011, doi: 10.1016/j.joms.2010.12.049.

[200] Y. Weng, Y. Cao, C. Arevalo, M. P. Vacanti, and C. A. Vacanti, "Tissue-engineered composites of bone and cartilage for mandible condylar reconstruction," *J. Oral Maxillofac. Surg.*, vol. 59, no. 2, pp. 185–190, Feb. 2001, doi: 10.1053/joms.2001.20491.

[201] M. P. J. van den Borne *et al.*, "International Cartilage Repair Society (ICRS) and Oswestry macroscopic cartilage evaluation scores validated for use in Autologous Chondrocyte Implantation (ACI) and microfracture," *Osteoarthritis Cartilage*, vol. 15, no. 12, pp. 1397–1402, Dec. 2007, doi: 10.1016/j.joca.2007.05.005.

[202] N. Vapniarsky *et al.*, "Histological, immunological, and genetic analysis of feline chronic gingivostomatitis," *Front. Vet. Sci.*, vol. 7, p. 310, Jun. 2020, doi: 10.3389/fvets.2020.00310.

[203] J. Ma *et al.*, "Modification of 3D printed PCL scaffolds by PVAc and HA to enhance cytocompatibility and osteogenesis," *RSC Adv.*, vol. 9, no. 10, pp. 5338–5346, 2019, doi: 10.1039/C8RA06652C.

[204] C. Cao, P. Huang, A. Prasopthum, A. J. Parsons, F. Ai, and J. Yang, "Characterisation of bone regeneration in 3D printed ductile PCL/PEG/hydroxyapatite scaffolds with high ceramic microparticle concentrations," *Biomater. Sci.*, vol. 10, no. 1, pp. 138–152, 2022, doi: 10.1039/D1BM01645H.

[205] Z. Ebrahimi, S. Irani, A. Ardeshirylajimi, and E. Seyedjafari, "Enhanced osteogenic differentiation of stem cells by 3D printed PCL scaffolds coated with collagen and hydroxyapatite," *Sci. Rep.*, vol. 12, no. 1, p. 12359, Jul. 2022, doi: 10.1038/s41598-022-15602-y.

[206] F. Greco, L. Leonetti, A. Pranno, and S. Rudykh, "Mechanical behavior of bio-inspired nacre-like composites: A hybrid multiscale modeling approach," *Compos. Struct.*, vol. 233, p. 111625, Feb. 2020, doi: 10.1016/j.compstruct.2019.111625.

[207] A. Erkliğ, M. Alsaadi, and M. Bulut, "A comparative study on industrial waste fillers affecting mechanical properties of polymer-matrix composites," *Mater. Res. Express*, vol. 3, no. 10, p. 105302, Oct. 2016, doi: 10.1088/2053-1591/3/10/105302.

[208] M. C. Saldívar, E. L. Doubrovski, M. J. Mirzaali, and A. A. Zadpoor, "Nonlinear coarse-graining models for 3D printed multi-material biomimetic composites," *Addit. Manuf.*, vol. 58, p. 103062, Oct. 2022, doi: 10.1016/j.addma.2022.103062.

[209] J. C. Nickel, L. R. Iwasaki, Y. M. Gonzalez, L. M. Gallo, and H. Yao, "Mechanobehavior and ontogenesis of the temporomandibular joint," *J. Dent. Res.*, vol. 97, no. 11, pp. 1185–1192, Oct. 2018, doi: 10.1177/0022034518786469.

[210] R. L. Boyd, C. H. Gibbs, P. E. Mahan, A. F. Richmond, and J. L. Laskin, "Temporomandibular joint forces measured at the condyle of Macaca arctoides," *Am. J. Orthod. Dentofacial Orthop.*, vol. 97, no. 6, pp. 472–479, Jun. 1990, doi: 10.1016/S0889-5406(05)80027-7.

[211] D. R. Sumner, "Long-term implant fixation and stress-shielding in total hip replacement," *J. Biomech.*, vol. 48, no. 5, pp. 797–800, Mar. 2015, doi: 10.1016/j.jbiomech.2014.12.021.

[212] A. Ramos and M. Mesnard, "A new condyle implant design concept for an alloplastic temporomandibular joint in bone resorption cases," *J. Cranio-Maxillofac. Surg.*, vol. 44, no. 10, pp. 1670–1677, Oct. 2016, doi: 10.1016/j.jcms.2016.07.024.

[213] C.-C. Ko *et al.*, "An intra-oral hydraulic system for controlled loading of dental implants," *J. Biomech.*, vol. 35, no. 6, pp. 863–869, Jun. 2002, doi: 10.1016/S0021-9290(02)00004-0.

[214] S. Szmukler-Moncler, H. Salama, Y. Reingewirtz, and J. H. Dubruille, "Timing of loading and effect of micromotion on bone-dental implant interface: Review of experimental literature," *J. Biomed. Mater. Res.*, vol. 43, no. 2, pp. 192–203, 1998, doi: 10.1002/(SICI)1097-4636(199822)43:2<192::AID-JBM14>3.0.CO;2-K.

[215] L. M. Wolford, L. G. Mercuri, E. D. Schneiderman, R. Movahed, and W. Allen, "Twenty-year follow-up study on a patient-fitted temporomandibular joint prosthesis: the techmedica/tmj concepts device," *J. Oral Maxillofac. Surg.*, vol. 73, no. 5, pp. 952–960, May 2015, doi: 10.1016/j.joms.2014.10.032.

[216] E. J. Granquist *et al.*, "Outcomes and survivorship of biomet microfixation total joint replacement system: results from an fda postmarket study," *J. Oral Maxillofac. Surg.*, vol. 78, no. 9, pp. 1499–1508, Sep. 2020, doi: 10.1016/j.joms.2020.04.021.

[217] E. K. Paluch *et al.*, "Mechanotransduction: use the force(s)," *BMC Biol.*, vol. 13, no. 1, p. 47, Dec. 2015, doi: 10.1186/s12915-015-0150-4.

[218] Q. A. Meslier and S. J. Shefelbine, "Using finite element modeling in bone mechanoadaptation," *Curr. Osteoporos. Rep.*, vol. 21, no. 2, pp. 105–116, Apr. 2023, doi: 10.1007/s11914-023-00776-9.

[219] S. J. Shefelbine and D. R. Carter, "Mechanobiological predictions of growth front morphology in developmental hip dysplasia," *J. Orthop. Res.*, vol. 22, no. 2, pp. 346–352, Mar. 2004, doi: 10.1016/j.orthres.2003.08.004.

[220] C. G. Stelea *et al.*, "Recovery of post-traumatic temporomandibular joint after mandibular fracture immobilization: a literature review," *Appl. Sci.*, vol. 11, no. 21, p. 10239, Nov. 2021, doi: 10.3390/app112110239.

[221] M. Franklin, M. M. Sperry, E. Phillips, E. J. Granquist, M. Marcolongo, and B. A. Winkelstein, "Painful temporomandibular joint overloading induces structural remodeling in the pericellular matrix of that joint's chondrocytes," *J. Orthop. Res.*, vol. 40, no. 2, pp. 348–358, Feb. 2022, doi: 10.1002/jor.25050.

[222] J. Chen, K. P. Sorensen, T. Gupta, T. Kilts, M. Young, and S. Wadhwa, "Altered functional loading causes differential effects in the subchondral bone and condylar cartilage in the temporomandibular joint from young mice," *Osteoarthritis Cartilage*, vol. 17, no. 3, pp. 354–361, Mar. 2009, doi: 10.1016/j.joca.2008.05.021.

[223] Lanza, Robert and Atala, Anthony, Eds., *Essentials of stem cell biology*, 3rd ed. 225 Wyman St. Waltham, MA 02451, USA: Elsevier, 2014. [Online]. Available: https://doi.org/10.1016/C2012-0-06957-8

[224] M. S. Detamore *et al.*, "Cell type and distribution in the porcine temporomandibular joint disc," *J. Oral Maxillofac. Surg.*, vol. 64, no. 2, pp. 243–248, Feb. 2006, doi: 10.1016/j.joms.2005.10.009.

[225] R. Bi *et al.*, "A single-cell transcriptional atlas reveals resident progenitor cell niche functions in TMJ disc development and injury," *Nat. Commun.*, vol. 14, no. 1, p. 830, Feb. 2023, doi: 10.1038/s41467-023-36406-2.

[226] N. D. Donahue, H. Acar, and S. Wilhelm, "Concepts of nanoparticle cellular uptake, intracellular trafficking, and kinetics in nanomedicine," *Adv. Drug Deliv. Rev.*, vol. 143, pp. 68–96, Mar. 2019, doi: 10.1016/j.addr.2019.04.008.

[227] A. Ruscitto, V. Scarpa, M. Morel, S. Pylawka, C. J. Shawber, and M. C. Embree, "Notch regulates fibrocartilage stem cell fate and is upregulated in inflammatory tmj

arthritis," *J. Dent. Res.*, vol. 99, no. 10, pp. 1174–1181, Sep. 2020, doi: 10.1177/0022034520924656.

[228] K. P. Simeonov *et al.*, "Single-cell lineage tracing of metastatic cancer reveals selection of hybrid EMT states," *Cancer Cell*, vol. 39, no. 8, pp. 1150-1162.e9, Aug. 2021, doi: 10.1016/j.ccell.2021.05.005.

[229] K. Nettleton, D. Luong, A. P. Kleinfehn, L. Savariau, C. Premanandan, and M. L. Becker, "Molecular mass-dependent resorption and bone regeneration of 3d printed ppf scaffolds in a critical-sized rat cranial defect model," *Adv. Healthc. Mater.*, vol. 8, no. 17, p. 1900646, Sep. 2019, doi: 10.1002/adhm.201900646.

[230] S. J. Polak, L. E. Rustom, G. M. Genin, M. Talcott, and A. J. Wagoner Johnson, "A mechanism for effective cell-seeding in rigid, microporous substrates," *Acta Biomater.*, vol. 9, no. 8, pp. 7977–7986, Aug. 2013, doi: 10.1016/j.actbio.2013.04.040.

[231] J. L. G. C. Monteiro, F. P. S. Guastaldi, M. J. Troulis, J. P. McCain, and B. C. do E. Vasconcelos, "Induction, treatment, and prevention of temporomandibular joint ankylosis—a systematic review of comparative animal studies," *J. Oral Maxillofac. Surg.*, vol. 79, no. 1, pp. 109-132.e6, Jan. 2021, doi: 10.1016/j.joms.2020.07.018.

[232] L. Ruggiero *et al.*, "Roles of the fibrous superficial zone in the mechanical behavior of tmj condylar cartilage," *Ann. Biomed. Eng.*, vol. 43, no. 11, pp. 2652–2662, Nov. 2015, doi: 10.1007/s10439-015-1320-9.

[233] K. Yang *et al.*, "Which of the fibrous layer is more important in the genesis of traumatic temporomanibular joint ankylosis: The mandibular condyle or the glenoid fossa?," *J. Stomatol. Oral Maxillofac. Surg.*, vol. 121, no. 5, pp. 517–522, Nov. 2020, doi: 10.1016/j.jormas.2019.12.014.

[234] Y.-B. Yan, J.-M. Li, E. Xiao, J.-G. An, Y.-H. Gan, and Y. Zhang, "A pilot trial on the molecular pathophysiology of traumatic temporomandibular joint bony ankylosis in a sheep model. Part II: The differential gene expression among fibrous ankylosis, bony ankylosis and condylar fracture," *J. Cranio-Maxillofac. Surg.*, vol. 42, no. 2, pp. e23–e28, Mar. 2014, doi: 10.1016/j.jcms.2013.04.008.

[235] H. Miyamoto, K. Kurita, N. Ogi, J.-I. Ishimaru, and A. N. Goss, "The role of the disk in sheep temporomandibular joint ankylosis," *Oral Surg. Oral Med. Oral Pathol. Oral Radiol. Endodontology*, vol. 88, no. 2, pp. 151–158, Aug. 1999, doi: 10.1016/S1079-2104(99)70109-5.

[236] Y. Xu and Q. Wu, "Trends and disparities in osteoarthritis prevalence among US adults, 2005–2018," *Sci. Rep.*, vol. 11, no. 1, p. 21845, Nov. 2021, doi: 10.1038/s41598-021-01339-7.

[237] A. J. Barr, T. M. Campbell, D. Hopkinson, S. R. Kingsbury, M. A. Bowes, and P. G. Conaghan, "A systematic review of the relationship between subchondral bone features, pain and structural pathology in peripheral joint osteoarthritis," *Arthritis Res. Ther.*, vol. 17, no. 1, p. 228, Dec. 2015, doi: 10.1186/s13075-015-0735-x.

[238] H. Long *et al.*, "Prevalence trends of site-specific osteoarthritis from 1990 to 2019: findings from the global burden of disease study 2019," *Arthritis Rheumatol.*, vol. 74, no. 7, pp. 1172–1183, Jul. 2022, doi: 10.1002/art.42089.

[239] X. Fan, X. Wu, R. Crawford, Y. Xiao, and I. Prasadam, "Macro, micro, and molecular. changes of the osteochondral interface in osteoarthritis development," *Front. Cell Dev. Biol.*, vol. 9, p. 659654, May 2021, doi: 10.3389/fcell.2021.659654.

[240] S. Critchley *et al.*, "3D printing of fibre-reinforced cartilaginous templates for the regeneration of osteochondral defects," *Acta Biomater.*, vol. 113, pp. 130–143, Sep. 2020, doi: 10.1016/j.actbio.2020.05.040.

[241] C. N. Kelly, A. T. Miller, S. J. Hollister, R. E. Guldberg, and K. Gall, "Design and structure–function characterization of 3d printed synthetic porous biomaterials for tissue engineering," *Adv. Healthc. Mater.*, vol. 7, no. 7, p. 1701095, Apr. 2018, doi: 10.1002/adhm.201701095.

[242] D. R. Bijukumar, C. McGeehan, and M. T. Mathew, "Regenerative medicine strategies in biomedical implants," *Curr. Osteoporos. Rep.*, vol. 16, no. 3, pp. 236–245, Jun. 2018, doi: 10.1007/s11914-018-0441-0.

[243] A. J. Sophia Fox, A. Bedi, and S. A. Rodeo, "The basic science of articular cartilage: Structure, composition, and function," *Sports Health*, vol. 1, no. 6, pp. 461–468, 2009, doi: 10.1177/1941738109350438.

[244] Z. Li *et al.*, "Engineering multifunctional hydrogel-integrated 3d printed bioactive prosthetic interfaces for osteoporotic osseointegration," *Adv. Healthc. Mater.*, vol. 11, no. 11, p. 2102535, Jun. 2022, doi: 10.1002/adhm.202102535.

[245] M. T. Frassica, C. J. Demott, E. M. Ramirez, and M. A. Grunlan, "Spatially controlled templated hydrogels for orthopedic interfacial tissue regeneration," *ACS Macro Lett.*, vol. 9, no. 12, pp. 1740–1744, Dec. 2020, doi: 10.1021/acsmacrolett.0c00712.

[246] D. Bicho, S. Pina, R. L. Reis, and J. M. Oliveira, *Commercial products for osteochondral tissue repair and regeneration*, vol. 1058. Springer, Cham, 2018. doi: 10.1007/978-3-319-76711-6_19.

[247] S. Ansari, S. Khorshidi, and A. Karkhaneh, "Engineering of gradient osteochondral tissue: From nature to lab," *Acta Biomater.*, vol. 87, pp. 41–54, 2019, doi: 10.1016/j.actbio.2019.01.071.

[248] W. E. Brown, B. J. Huang, J. C. Hu, and K. A. Athanasiou, "Engineering large, anatomically shaped osteochondral constructs with robust interfacial shear properties," *Npj Regen. Med.*, vol. 6, no. 1, pp. 18–20, 2021, doi: 10.1038/s41536-021-00152-0.

[249] L. Tayebi, Z. Cui, and H. Ye, "A tri-component knee plug for the 3rd generation of autologous chondrocyte implantation," *Sci. Rep.*, vol. 10, no. 1, p. 17048, Oct. 2020, doi: 10.1038/s41598-020-73863-x.

[250] M. A. Nowicki, N. J. Castro, M. W. Plesniak, and L. G. Zhang, "3D printing of novel osteochondral scaffolds with graded microstructure," *Nanotechnology*, vol. 27, no. 41, 2016, doi: 10.1088/0957-4484/27/41/414001.

[251] H. Seddiqi *et al.*, "Inlet flow rate of perfusion bioreactors affects fluid flow dynamics, but not oxygen concentration in 3D-printed scaffolds for bone tissue engineering: Computational analysis and experimental validation," *Comput. Biol. Med.*, vol. 124, no. February, p. 103826, 2020, doi: 10.1016/j.compbiomed.2020.103826.

[252] S. Gómez, M. D. Vlad, J. López, and E. Fernández, "Design and properties of 3D scaffolds for bone tissue engineering," *Acta Biomater.*, vol. 42, pp. 341–350, Sep. 2016, doi: 10.1016/j.actbio.2016.06.032.

[253] H. Chen *et al.*, "Design and properties of biomimetic irregular scaffolds for bone tissue engineering," *Comput. Biol. Med.*, vol. 130, p. 104241, Mar. 2021, doi: 10.1016/j.compbiomed.2021.104241.

[254] Y. Jin, S. Zou, B. Pan, G. Li, L. Shao, and J. Du, "Biomechanical properties of cylindrical and twisted triply periodic minimal surface scaffolds fabricated by laser powder bed fusion," *Addit. Manuf.*, vol. 56, p. 102899, Aug. 2022, doi: 10.1016/j.addma.2022.102899.

[255] N. Kumar *et al.*, "Mimicking high strength lightweight novel structures inspired from the trabecular bone microarchitecture," *Philos. Trans. R. Soc. Math. Phys. Eng. Sci.*, vol. 378, no. 2167, p. 20190448, Mar. 2020, doi: 10.1098/rsta.2019.0448.

[256] L. Vaiani, A. E. Uva, and A. Boccaccio, "Structural and topological design of conformal bilayered scaffolds for bone tissue engineering," *Thin-Walled Struct.*, vol. 192, p. 111209, Nov. 2023, doi: 10.1016/j.tws.2023.111209.

[257] Y. Yang *et al.*, "Gaussian curvature–driven direction of cell fate toward osteogenesis with triply periodic minimal surface scaffolds," *Proc. Natl. Acad. Sci.*, vol. 119, no. 41, p. e2206684119, Oct. 2022, doi: 10.1073/pnas.2206684119.

[258] K. M Moerman, "Gibbon: the geometry and image-based bioengineering add-on," *J. Open Source Softw.*, vol. 3, no. 22, p. 506, 2018, doi: 10.21105/joss.00506.

[259] S. A. Maas, B. J. Ellis, G. A. Ateshian, and J. A. Weiss, "Febio: finite elements for biomechanics," *J. Biomech. Eng.*, vol. 134, no. 1, p. 011005, Jan. 2012, doi: 10.1115/1.4005694.

[260] P. Diloksumpan *et al.*, "Combining multi-scale 3D printing technologies to engineer reinforced hydrogel-ceramic interfaces," *Biofabrication*, vol. 12, no. 2, p. 025014, Apr. 2020, doi: 10.1088/1758-5090/ab69d9.

[261] P. H. Warnke *et al.*, "Rapid Prototyping: Porous Titanium Alloy Scaffolds Produced by Selective Laser Melting for Bone Tissue Engineering," *Tissue Eng. Part C Methods*, vol. 15, no. 2, pp. 115–124, Jun. 2009, doi: 10.1089/ten.tec.2008.0288.

[262] M. Singh, C. P. Morris, R. J. Ellis, M. S. Detamore, and C. Berkland, "Microsphere-Based Seamless Scaffolds Containing Macroscopic Gradients of Encapsulated Factors for Tissue Engineering," *Tissue Eng. Part C Methods*, vol. 14, no. 4, pp. 299–309, Dec. 2008, doi: 10.1089/ten.tec.2008.0167.

[263] W. Zhang *et al.*, "The effect of interface microstructure on interfacial shear strength for osteochondral scaffolds based on biomimetic design and 3D printing," *Mater. Sci. Eng. C*, vol. 46, pp. 10–15, Jan. 2015, doi: 10.1016/j.msec.2014.09.042.

[264] S. Wang *et al.*, "Strength enhanced hydrogels constructed from agarose in alkali/urea aqueous solution and their application," *Chem. Eng. J.*, vol. 331, pp. 177–184, Jan. 2018, doi: 10.1016/j.cej.2017.08.118.

[265] P. Zarrintaj *et al.*, "Agarose-based biomaterials for tissue engineering," *Carbohydr. Polym.*, vol. 187, pp. 66–84, May 2018, doi: 10.1016/j.carbpol.2018.01.060.

[266] S. M. Hull, L. G. Brunel, and S. C. Heilshorn, "3d bioprinting of cell-laden hydrogels for improved biological functionality," *Adv. Mater.*, vol. 34, no. 2, p. 2103691, Jan. 2022, doi: 10.1002/adma.202103691.

[267] G. Liu and Q. Wang, "Thermoelastic asperity contacts, frictional shear, and parameter correlations," *J. Tribol.*, vol. 122, no. 1, pp. 300–307, Jan. 2000, doi: 10.1115/1.555357.

[268] J. M. Link, E. Y. Salinas, J. C. Hu, and K. A. Athanasiou, "The tribology of cartilage: Mechanisms, experimental techniques, and relevance to translational tissue engineering," *Clin. Biomech.*, vol. 79, p. 104880, Oct. 2020, doi: 10.1016/j.clinbiomech.2019.10.016.

[269] A. O'Reilly and D. J. Kelly, "A computational model of osteochondral defect repair following implantation of stem cell-laden multiphase scaffolds," *Tissue Eng. Part A*, vol. 23, no. 1–2, pp. 30–42, Jan. 2017, doi: 10.1089/ten.tea.2016.0175.

[270] K. M. Moerman, C. K. Simms, and T. Nagel, "Control of tension–compression asymmetry in Ogden hyperelasticity with application to soft tissue modelling," *J. Mech. Behav. Biomed. Mater.*, vol. 56, pp. 218–228, Mar. 2016, doi: 10.1016/j.jmbbm.2015.11.027.

[271] R. J. McCoy, C. Jungreuthmayer, and F. J. O'Brien, "Influence of flow rate and scaffold pore size on cell behavior during mechanical stimulation in a flow perfusion bioreactor," *Biotechnol. Bioeng.*, vol. 109, no. 6, pp. 1583–1594, Jun. 2012, doi: 10.1002/bit.24424.

[272] G. a. Ateshian, N. O. Chahine, I. M. Basalo, and C. T. Hung, "The correspondence between equilibrium biphasic and triphasic material properties in mixture models of articular cartilage," *J. Biomech.*, vol. 37, no. 3, pp. 391–400, 2004, doi: 10.1016/S0021-9290(03)00252-5.

[273] R. M. Wilkins, B. T. Chimenti, and R. M. Rifkin, "Percutaneous treatment of long bone nonunions: the use of autologous bone marrow and allograft bone matrix," *Orthopedics*, vol. 26, no. 5, May 2003, doi: 10.3928/0147-7447-20030502-04.

[274] J. D. Conway, "Autograft and nonunions: morbidity with intramedullary bone graft versus iliac crest bone graft," *Orthop. Clin. North Am.*, vol. 41, no. 1, pp. 75–84, Jan. 2010, doi: 10.1016/j.ocl.2009.07.006.

[275] M. L. Azi, A. Aprato, I. Santi, M. Kfuri, A. Masse, and A. Joeris, "Autologous bone graft in the treatment of post-traumatic bone defects: a systematic review and meta-analysis," *BMC Musculoskelet. Disord.*, vol. 17, no. 1, p. 465, Dec. 2016, doi: 10.1186/s12891-016-1312-4.

[276] F. Migliorini, G. La Padula, E. Torsiello, F. Spiezia, F. Oliva, and N. Maffulli, "Strategies for large bone defect reconstruction after trauma, infections or tumour excision: a comprehensive review of the literature," *Eur. J. Med. Res.*, vol. 26, no. 1, p. 118, Dec. 2021, doi: 10.1186/s40001-021-00593-9.

[277] H. D. Adkisson, J. Strauss-Schoenberger, M. Gillis, R. Wilkins, M. Jackson, and K. A. Hruska, "Rapid quantitative bioassay of osteoinduction," *J. Orthop. Res.*, vol. 18, no. 3, pp. 503–511, May 2000, doi: 10.1002/jor.1100180326.

[278] J. L. D. S. Pires *et al.*, "Repair of critical size bone defects using synthetic hydroxyapatite or xenograft with or without the bone marrow mononuclear fraction: a histomorphometric and immunohistochemical study in rat calvaria," *Materials*, vol. 14, no. 11, p. 2854, May 2021, doi: 10.3390/ma14112854.

[279] J. M. Townsend *et al.*, "Superior calvarial bone regeneration using pentenoate-functionalized hyaluronic acid hydrogels with devitalized tendon particles," *Acta Biomater.*, vol. 71, pp. 148–155, Apr. 2018, doi: 10.1016/j.actbio.2018.02.013.

[280] J. Wind *et al.*, "Twelve-month results from a prospective clinical study evaluating the efficacy and safety of cellular bone allograft in subjects undergoing lumbar spinal fusion," *Neurol. Int.*, vol. 14, no. 4, pp. 875–883, Oct. 2022, doi: 10.3390/neurolint14040070.

[281] S. C. Dennis, C. J. Berkland, L. F. Bonewald, and M. S. Detamore, "Endochondral ossification for enhancing bone regeneration: converging native extracellular matrix biomaterials and developmental engineering *in vivo*," *Tissue Eng. Part B Rev.*, vol. 21, no. 3, pp. 247–266, Jun. 2015, doi: 10.1089/ten.teb.2014.0419.

[282] J. M. Townsend *et al.*, "Comparison of a thiolated demineralized bone matrix hydrogel to a clinical product control for regeneration of large sheep cranial defects," *Materialia*, vol. 27, 2023.

[283] H. Zhang *et al.*, "Demineralized bone matrix carriers and their clinical applications: an overview," *Orthop. Surg.*, vol. 11, no. 5, pp. 725–737, Oct. 2019, doi: 10.1111/os.12509.

[284] J. E. Samorezov and E. Alsberg, "Spatial regulation of controlled bioactive factor delivery for bone tissue engineering," *Adv. Drug Deliv. Rev.*, vol. 84, pp. 45–67, Apr. 2015, doi: 10.1016/j.addr.2014.11.018.

[285] X. Yang, Y. Wang, Y. Zhou, J. Chen, and Q. Wan, "The application of polycaprolactone in three-dimensional printing scaffolds for bone tissue engineering," *Polymers*, vol. 13, no. 16, p. 2754, Aug. 2021, doi: 10.3390/polym13162754.

[286] M. Mirkhalaf, Y. Men, R. Wang, Y. No, and H. Zreiqat, "Personalized 3D printed bone scaffolds: A review," *Acta Biomater.*, vol. 156, pp. 110–124, Jan. 2023, doi: 10.1016/j.actbio.2022.04.014.

[287] J. P. Temple *et al.*, "Engineering anatomically shaped vascularized bone grafts with hASCs and 3D-printed PCL scaffolds," *J. Biomed. Mater. Res. - Part A*, vol. 102, no. 12, pp. 4317–4325, 2014, doi: 10.1002/jbm.a.35107.

[288] L. Zhang, G. Yang, B. N. Johnson, and X. Jia, "Three-dimensional (3D) printed scaffold and material selection for bone repair," *Acta Biomater.*, vol. 84, pp. 16–33, Jan. 2019, doi: 10.1016/j.actbio.2018.11.039.

[289] A. Haryńska, J. Kucinska-Lipka, A. Sulowska, I. Gubanska, M. Kostrzewa, and H. Janik, "Medical-grade pcl based polyurethane system for fdm 3d printing—characterization and fabrication," *Materials*, vol. 12, no. 6, p. 887, Mar. 2019, doi: 10.3390/ma12060887.

[290] A. Schwab, R. Levato, M. D'Este, S. Piluso, D. Eglin, and J. Malda, "Printability and shape fidelity of bioinks in 3d bioprinting," *Chem. Rev.*, vol. 120, no. 19, pp. 11028–11055, Oct. 2020, doi: 10.1021/acs.chemrev.0c00084.

[291] C. J. Culbreath, B. Gaerke, M. S. Taylor, S. D. McCullen, and O. T. Mefford, "Effect of infill on resulting mechanical properties of additive manufactured bioresorbable polymers for medical devices," *Materialia*, vol. 12, p. 100732, Aug. 2020, doi: 10.1016/j.mtla.2020.100732.

[292] M. A. Woodruff and D. W. Hutmacher, "The return of a forgotten polymer—Polycaprolactone in the 21st century," *Prog. Polym. Sci.*, vol. 35, no. 10, pp. 1217–1256, Oct. 2010, doi: 10.1016/j.progpolymsci.2010.04.002.

[293] R. Dwivedi *et al.*, "Polycaprolactone as biomaterial for bone scaffolds: Review of literature," *J. Oral Biol. Craniofacial Res.*, vol. 10, no. 1, pp. 381–388, Jan. 2020, doi: 10.1016/j.jobcr.2019.10.003.

[294] M. E. Hoque *et al.*, "Processing of polycaprolactone and polycaprolactone-based copolymers into 3d scaffolds, and their cellular responses," *Tissue Eng. Part A*, vol. 15, no. 10, pp. 3013–3024, Oct. 2009, doi: 10.1089/ten.tea.2008.0355.

[295] S. Murab, S. Herold, T. Hawk, A. Snyder, E. Espinal, and P. Whitlock, "Advances in additive manufacturing of polycaprolactone based scaffolds for bone regeneration," *J. Mater. Chem. B*, vol. 11, no. 31, pp. 7250–7279, 2023, doi: 10.1039/D2TB02052A.

[296] S.-H. Teoh, B.-T. Goh, and J. Lim, "Three-dimensional printed polycaprolactone scaffolds for bone regeneration success and future perspective," *Tissue Eng. Part A*, vol. 25, no. 13–14, pp. 931–935, Jul. 2019, doi: 10.1089/ten.tea.2019.0102.

[297] J. A. Driscoll *et al.*, "3d-printed ceramic-demineralized bone matrix hyperelastic bone composite scaffolds for spinal fusion," *Tissue Eng. - Part A*, vol. 26, no. 3–4, pp. 157–166, 2020, doi: 10.1089/ten.tea.2019.0166.

[298] A. E. Jakus *et al.*, "Hyperelastic 'bone': A highly versatile, growth factor-free, osteoregenerative, scalable, and surgically friendly biomaterial," *Sci. Transl. Med.*, vol. 8, no. 358, pp. 1–16, 2016, doi: 10.1126/scitranslmed.aaf7704.

[299] E. Nyberg, A. Rindone, A. Dorafshar, and W. L. Grayson, "Comparison of 3d-printed poly-ε-caprolactone scaffolds functionalized with tricalcium phosphate, hydroxyapatite, bio-oss, or decellularized bone matrix," *Tissue Eng. Part A*, vol. 23, no. 11–12, pp. 503–514, Jun. 2017, doi: 10.1089/ten.tea.2016.0418.

[300] B. Beig, U. Liaqat, M. F. K. Niazi, I. Douna, M. Zahoor, and M. B. K. Niazi, "Current challenges and innovative developments in hydroxyapatite-based coatings on metallic materials for bone implantation: a review," *Coatings*, vol. 10, no. 12, p. 1249, Dec. 2020, doi: 10.3390/coatings10121249.

[301] S. Awasthi, S. K. Pandey, E. Arunan, and C. Srivastava, "A review on hydroxyapatite coatings for the biomedical applications: experimental and theoretical perspectives," *J. Mater. Chem. B*, vol. 9, no. 2, pp. 228–249, 2021, doi: 10.1039/D0TB02407D.

[302] M. G. Yeo and G. H. Kim, "Preparation and characterization of 3d composite scaffolds based on rapid-prototyped pcl/β-tcp struts and electrospun pcl coated with collagen and ha for bone regeneration," *Chem. Mater.*, vol. 24, no. 5, pp. 903–913, Mar. 2012, doi: 10.1021/cm201119q.

[303] S. Safaee *et al.*, "Fabrication of bioactive glass coating on pure titanium by sol-dip method: Dental applications," *Dent. Mater. J.*, vol. 40, no. 4, pp. 949–956, Jul. 2021, doi: 10.4012/dmj.2020-323.

[304] M. Karimi Kichi, R. Torkaman, H. Mohammadi, A. Toutounchi, M. Kharaziha, and F. Alihosseini, "Electrochemical and in vitro bioactivity behavior of poly (ε-caprolactone) (PCL)-gelatin-forsterite nano coating on titanium for biomedical

application," *Mater. Today Commun.*, vol. 24, p. 101326, Sep. 2020, doi: 10.1016/j.mtcomm.2020.101326.

[305] K. Ishikawa, Y. Miyamoto, M. Nagayama, and K. Asaoka, "Blast coating method: New method of coating titanium surface with hydroxyapatite at room temperature," *J. Biomed. Mater. Res.*, vol. 38, no. 2, pp. 129–134, 1997, doi: 10.1002/(SICI)1097-4636(199722)38:2<129::AID-JBM7>3.0.CO;2-S.

[306] A. Zimmerling, Z. Yazdanpanah, D. M. L. Cooper, J. D. Johnston, and X. Chen, "3D printing PCL/nHA bone scaffolds: exploring the influence of material synthesis techniques," *Biomater. Res.*, vol. 25, no. 1, p. 3, Feb. 2021, doi: 10.1186/s40824-021-00204-y.

[307] M. Jiang, G. Chen, J. Coles-Black, J. Chuen, and A. Hardidge, "Three-dimensional printing in orthopaedic preoperative planning improves intraoperative metrics: a systematic review," *ANZ J. Surg.*, vol. 90, no. 3, pp. 243–250, Mar. 2020, doi: 10.1111/ans.15549.

[308] E. Gruskin, B. A. Doll, F. W. Futrell, J. P. Schmitz, and J. O. Hollinger, "Demineralized bone matrix in bone repair: History and use," *Adv. Drug Deliv. Rev.*, vol. 64, no. 12, pp. 1063–1077, Sep. 2012, doi: 10.1016/j.addr.2012.06.008.

[309] Y. Yang *et al.*, "Gaussian curvature–driven direction of cell fate toward osteogenesis with triply periodic minimal surface scaffolds," *Proc. Natl. Acad. Sci.*, vol. 119, no. 41, p. e2206684119, Oct. 2022, doi: 10.1073/pnas.2206684119.

[310] M. Ronnenberg, "Evaluating appearance differences of color 3d printed objects," Rochester Institute of Technology, 2020.

[311] X. Chen, C. Gao, J. Jiang, Y. Wu, P. Zhu, and G. Chen, "3D printed porous PLA/nHA composite scaffolds with enhanced osteogenesis and osteoconductivityin vivo for bone regeneration," *Biomed. Mater. Bristol*, vol. 14, no. 6, 2019, doi: 10.1088/1748-605X/ab388d.

[312] D. Liu *et al.*, "3D printed PCL/SrHA scaffold for enhanced bone regeneration," *Chem. Eng. J.*, vol. 362, pp. 269–279, Apr. 2019, doi: 10.1016/j.cej.2019.01.015.

[313] V. Guarino *et al.*, "The role of hydroxyapatite as solid signal on performance of PCL porous scaffolds for bone tissue regeneration," *J. Biomed. Mater. Res. B Appl. Biomater.*, vol. 86B, no. 2, pp. 548–557, Aug. 2008, doi: 10.1002/jbm.b.31055.

[314] M. Plantz *et al.*, "Preclinical safety of a 3d-printed hydroxyapatite-demineralized bone matrix scaffold for spinal fusion," *Spine*, vol. 47, no. 1, pp. 82–89, 2022, doi: 10.1097/BRS.0000000000004142.

[315] A. Leroux *et al.*, "Long-term hydrolytic degradation study of polycaprolactone films and fibers grafted with poly(sodium styrene sulfonate): Mechanism study and cell response," *Biointerphases*, vol. 15, no. 6, p. 061006, Nov. 2020, doi: 10.1116/6.0000429.

[316] R. Langer, "New methods of drug delivery," *Science*, vol. 249, no. 4976, pp. 1527–1533, Sep. 1990, doi: 10.1126/science.2218494.

[317] N. Ramesh, S. C. Moratti, and G. J. Dias, "Hydroxyapatite-polymer biocomposites for bone regeneration: a review of current trends: hydroxyapatite/polymer biocomposites for bone regeneration: a review," *J. Biomed. Mater. Res. B Appl. Biomater.*, vol. 106, no. 5, pp. 2046–2057, Jul. 2018, doi: 10.1002/jbm.b.33950.

[318] M. Alipour *et al.*, "In vivo evaluation of biocompatibility and immune modulation potential of poly(caprolactone)–poly(ethylene glycol)–poly(caprolactone)-gelatin hydrogels enriched with nano-hydroxyapatite in the model of mouse," *J. Biomater. Appl.*, vol. 35, no. 10, pp. 1253–1263, May 2021, doi: 10.1177/0885328221998525.

Appendix A: Figures

Chapter 1: No Figures

Chapter 2: Figures 2.1-2.2

Chapter 3: Figures 3.1-3.4

Chapter 4: Figures 4.1-4.10

Chapter 5: Figures 5.1-5.6

Chapter 6: Figures 6.1-6.5

Chapter 7: No Figures
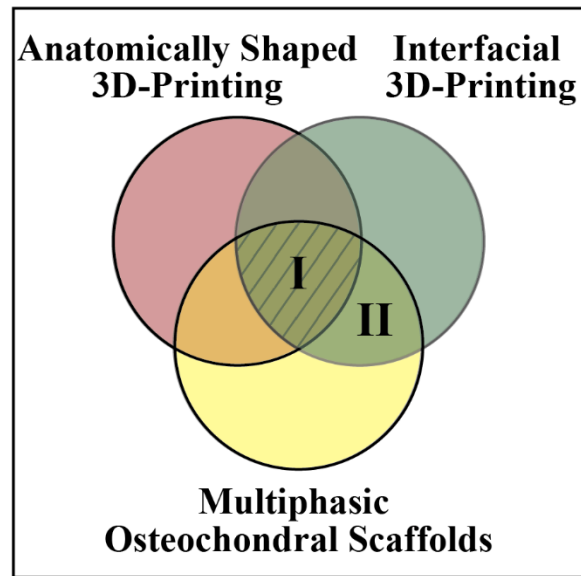
Figure 2.1: Venn diagram schematic of strategies that have leveraged stratified scaffolds and 3D-printing for biomedical applications.

The overlapping zones I and II were emphasized in the current review. The shaded region I represented advanced applications of 3D-printing that are poised to address the grand challenge for large-scale osteochondral tissue regeneration.
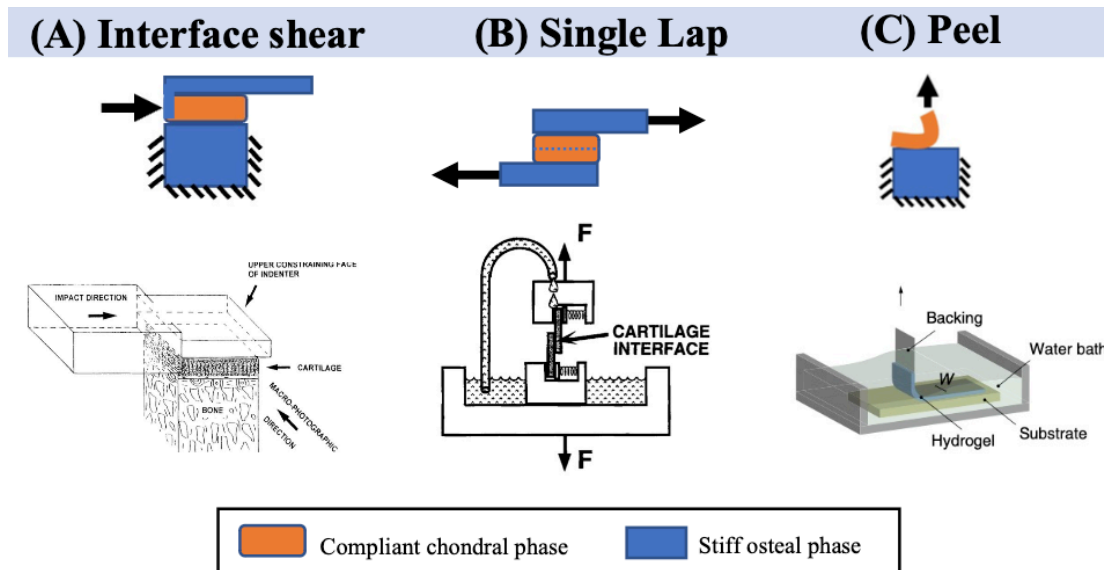
Figure 2.2: Osteochondral mechanical interface evaluation methods.

(A) Interface shear test (Broom *et al.* 1996). **(B)** Lap shear (Reindel *et al.* 1995) test. **(C)** Peel test (Liu *et al.* 2020). These methods have been used to evaluate the interface strength between compliant and stiff components of osteochondral constructs.
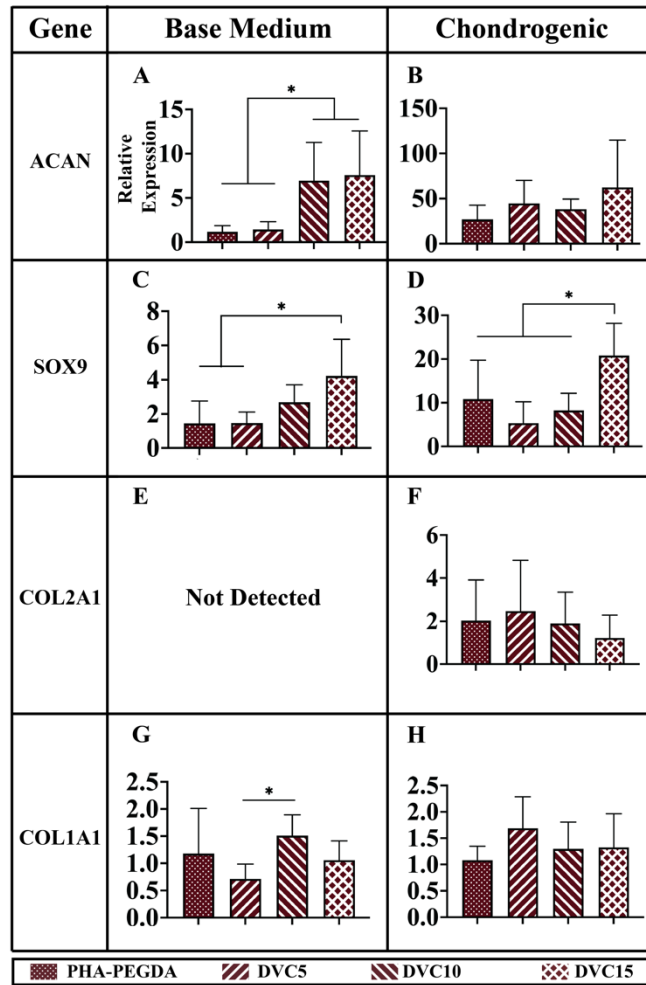
Figure 3.1: Aim 1 Gene expression of human bone mesenchymal stem cells 24 days after seeding on hydrogels.

ACAN and SOX9 genes were upregulated in hydrogel groups containing devitalized cartilage (DVC). **(A)** Relative aggrecan expression in base medium was raised in DVC10 and DVC15. **(B, D, F, H)** Chondrogenic medium with TGF-β enhanced gene expression compared to medium without TGF-β among all genes except COL1 ($p < 0.05$). **(C, D)** DVC15 groups exhibited higher SOX9 in both media. DVC15 exhibited increases in SOX9 expression relative to PHA-PEGDA in both media. **(E)** Collagen type 2 expression was not detectable in base medium. **(F)** Collagen type II was detected in chondrogenic medium, but there were no significant differences among groups. **(G, H)** Collagen type I expression was higher in DVC10 than in DVC5, but no other differences were observed among groups. Pentenoate-modified hyaluronic acid (PHA) was 4% w/v, and PEGDA was 20% w/v. n=8. *$p < 0.05$.
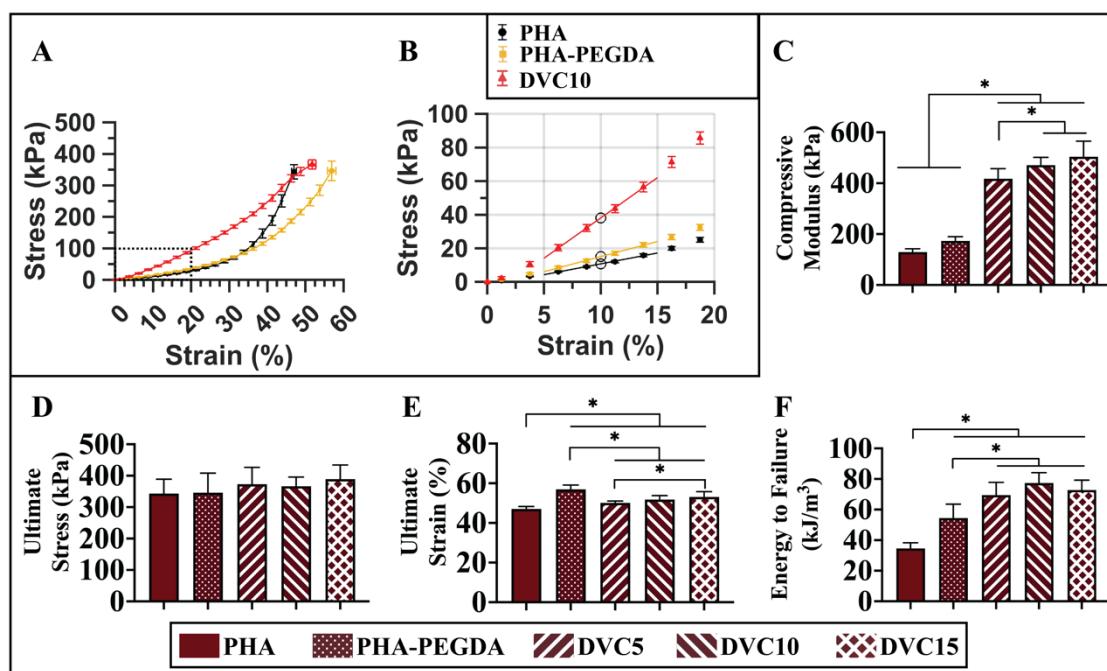
Figure 3.2: Aim 1 Compressive elastic moduli and failure properties of hydrogels. With stress and strain being negative values for compression, those values are presented here as magnitudes.

(A) Stress-strain plots for pentenoate-modified hyaluronic acid (PHA), PHA-polyethylene glycol diacrylate (PHA-PEGDA), and devitalized cartilage-10% w/v (DVC10) hydrogels. Dashed lines indicate region of panel B. **(B)** The slope of a line fit to 5-15% strain was used to determine compressive elastic moduli. **(C)** The compressive elastic moduli increased with both PEGDA and DVC. **(D)** The ultimate stresses ranged from 343 to 389 kPa with no significant differences among groups. **(E)** PHA-PEGDA exhibited a higher ultimate strain compared to all other groups. **(F)** Energy to failure increased with the addition of PEGDA and further increased with the addition of DVC. PHA was 4% w/v, and PEGDA was 20% w/v. n=6-8. *$p < 0.05$.
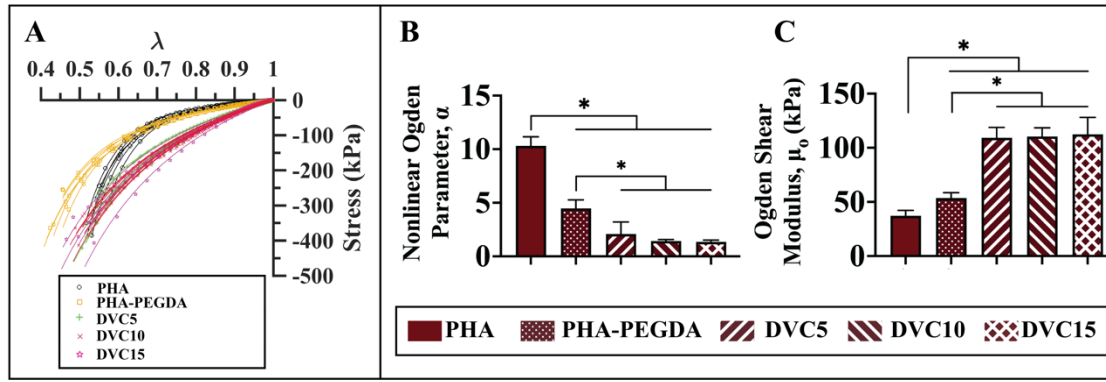
Figure 3.3: Aim 1 Ogden hyperelastic model fitted to hydrogel compression data

(A) The model exhibited a reasonably good fit ($R^2 > 0.987$ for every sample) to hydrogel compression data across the full stretch range to initial failure. **(B)** The nonlinear parameter, α, was reduced in hydrogels with DVC. **(C)** The mean shear moduli, μ_o, were lower in hydrogels without devitalized cartilage (DVC) than in hydrogels with DVC. Pentenoate-modified hyaluronic acid (PHA) was 4% w/v, and polyethylene glycol diacrylate (PEGDA) was 20% w/v. n=6-8. *p < 0.05.

154
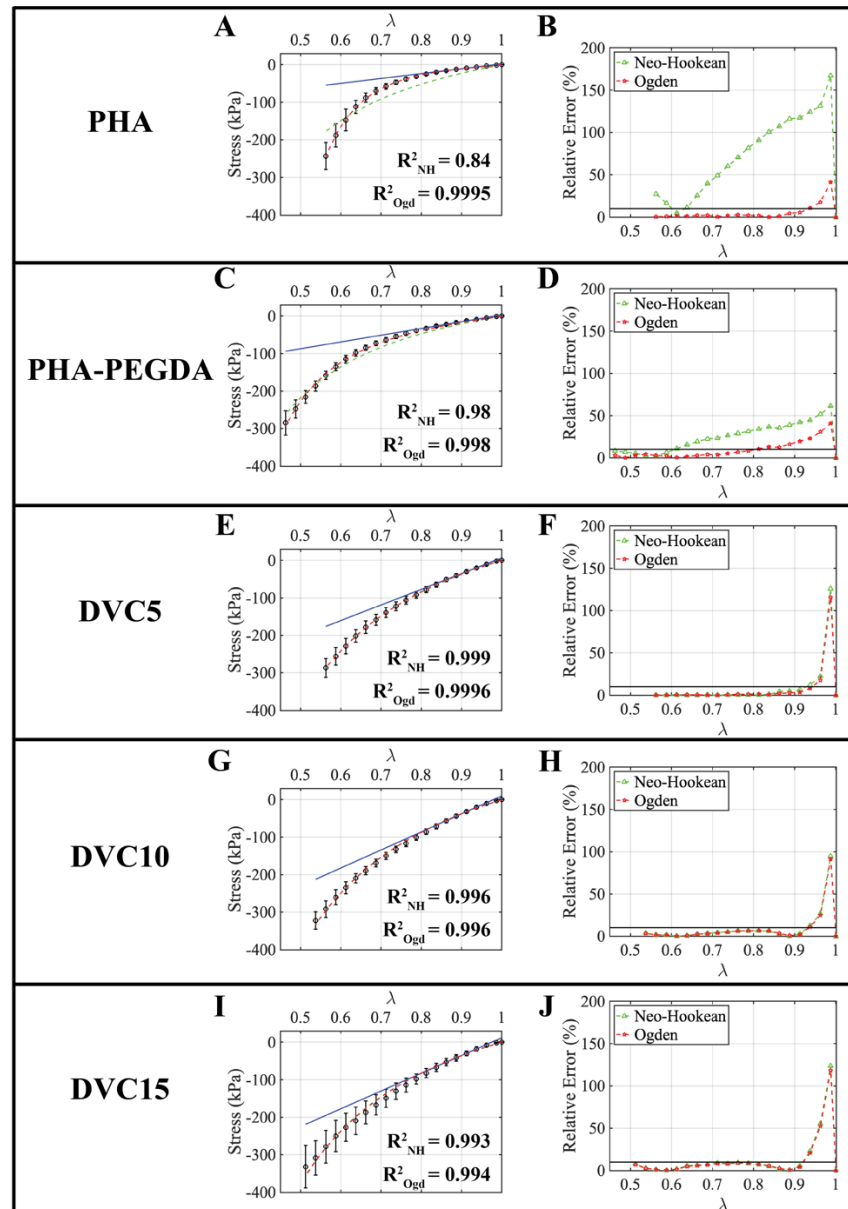
Figure 3.4: Aim 1 The Ogden model exhibited an accurate fit for all of the hydrogels.

(A, C, E, G, I) Linear regression (from $\lambda = 0.95$ to 0.85), neo-Hookean (NH) model, and one-term Ogden (Ogd) model fits to entire data. The Ogden model exhibited a more accurate fit to the full range of data than the neo-Hookean model. **(B, D)** Relative errors for the Ogden model were lower than those of the neo-Hookean model for the pentenoate-modified hyaluronic acid (PHA) and PHA-polyethylene glycol diacrylate (PHA-PEGDA) groups. **(F, H, J)** In the devitalized cartilage (DVC) hydrogel groups there was only a miniscule difference in error between the Ogden and neo-Hookean models. Relative errors of 10% were represented by a horizontal black line for reference. R^2 values were the arithmetic mean for each group. PHA was 4% w/v, and PEGDA was 20% w/v. n=6-8.
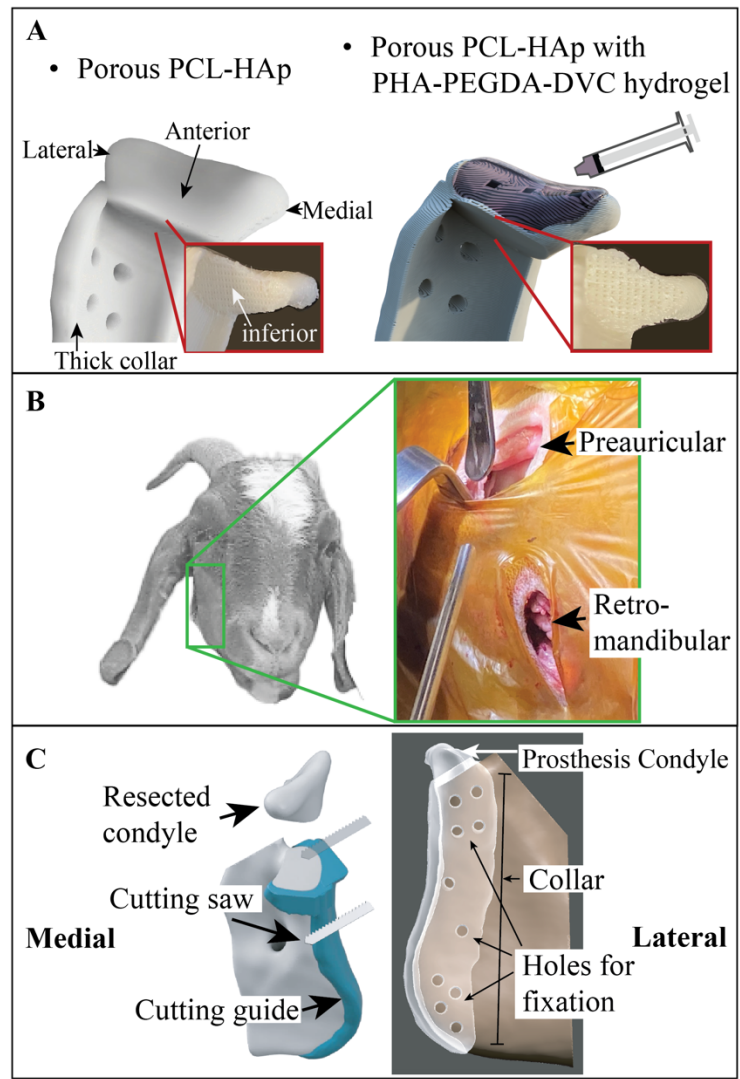
Figure 4.1: Aim 2 Schematic diagram of the prosthesis and surgical implantation.

(A) Two prosthesis designs were orthotopically implanted: (1) A smooth polycaprolactone-hydroxyapatite (PCL-HAp) prosthesis, and (2) a biphasic prosthesis with both PCL-HAp and a chondrogenic hydrogel comprised of pentenoate-modified hyaluronic acid (PHA), polyethylene glycol (PEGDA), and devitalized cartilage (DVC) was syringed onto the interlocking condyle with a recessed surface and UV-crosslinked such that the integrated hydrogel was flush with the condyle surface. Both prosthesis designs had a porous internal architecture. **(B)** Surgical implantation was performed with preauricular and retromandibular incisions. The condyle was resected through the preauricular incision, and then the prosthesis was inserted through the retromandibular incision. **(C)** To resect the condyle, a cutting guide was inserted and fixed to the mandible. Subsequently, the guide was removed, and the prosthesis was inserted and fixed into position.
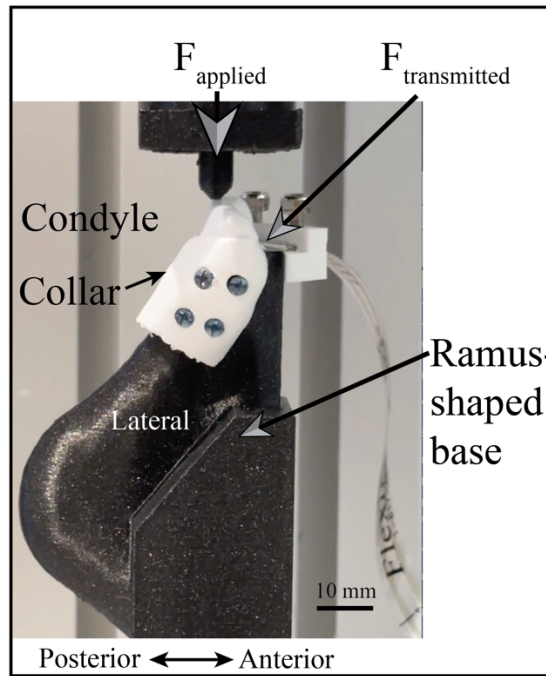
Figure 4.2: Aim 2 Illustration of the testing setup for load transmission.

The upper half of the prosthesis was fixed to a 3D printed ramus-shaped base. A 5 lb$_f$ load was applied to the condyle and the transmitted load was measured with a force sensitive resistor positioned between the condyle and the base. Following each sample, the force sensitive resistor was calibrated by repeating the test with an unconstrained condyle.
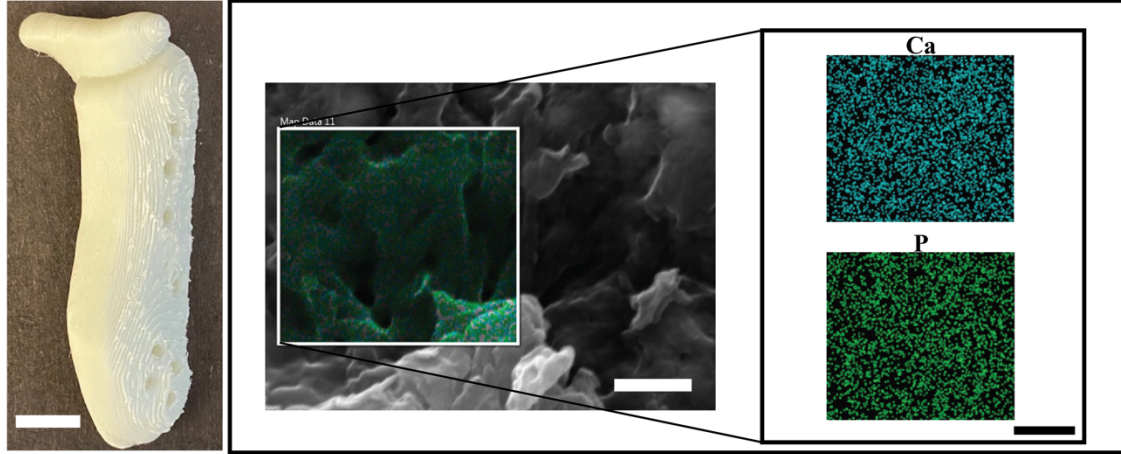
Figure 4.3: Aim 2 Calcium and phosphorous were distributed throughout the 3D-printed polycaprolactone-hydroxyapatite (PCL-HAp).

Scanning electron microscopy (SEM) of 3D-printed PCL-HAp using energy-dispersive x-ray spectroscopy exhibited homogeneously distributed calcium and phosphorous. Scale bar for lefthand image of prosthesis was 10 mm. Scale bars for SEM and EDS were 1 μm.
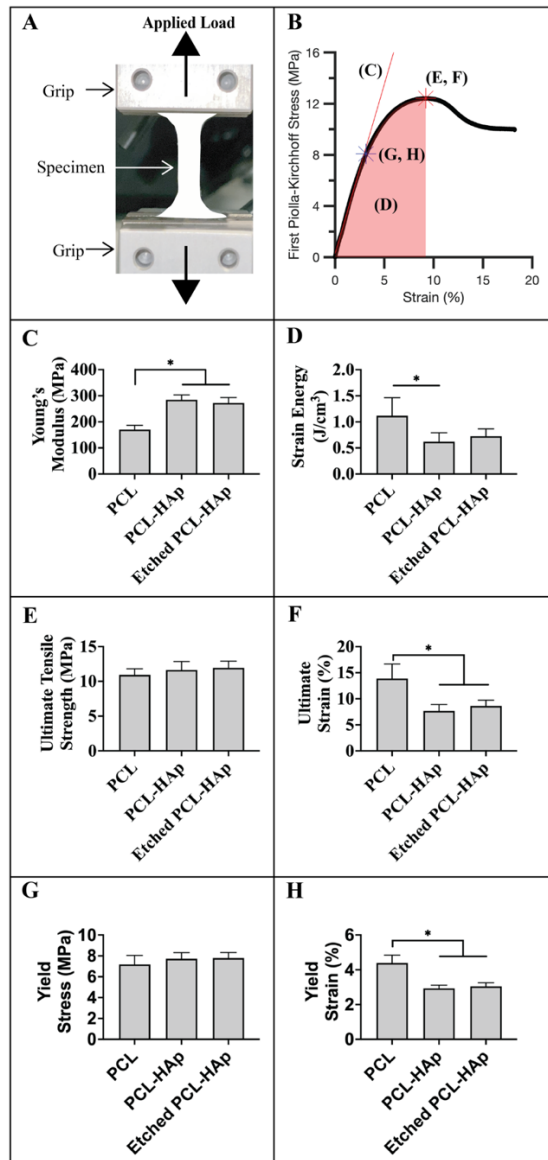
Figure 4.4: Aim 2 Uniaxial tension of 3D-printed polycaprolactone-hydroxyapatite (PCL-HAp). Adding HAp significantly enhanced PCL's mechanical performance.

(A) Illustration of test following ASTM D1708. **(B)** Representative stress/strain plot where letters C-H refer to the parameters reported in the following panels. **(C)** The addition of HAp significantly enhanced PCL stiffness, but not after NaOH etching compared to non-etched PCL-HAp. **(D)** Strain energy decreased with the addition of HAp, but not after NaOH etching compared to non-etched PCL-HAp. **(E)** The ultimate tensile strengths did not differ among groups. **(F)** Ultimate strains decreased with the addition of HAp, but not after NaOH etching compared to non-etched PCL-HAp. **(G)** Similar yield stresses were exhibited across the different groups. **(H)** The yield strain decreased with the addition of HAp to PCL, but not after NaOH etching compared to non-etched PCL-HAp. n = 5-6. *p < 0.05. All data are mean $\pm$ standard deviation. HAp was 20 wt/wt %.
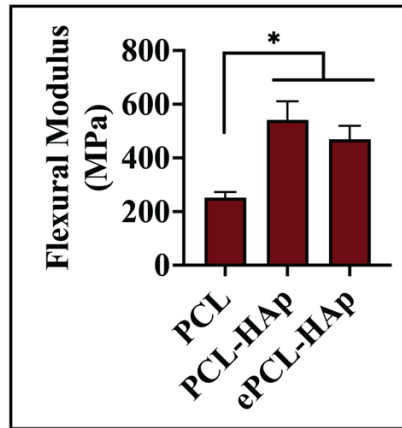
Figure 4.5. Aim 2 Three-point bend test of 3D-printed composites following ASTM D790.

The addition of hydroxyapatite (HAp) increased polycaprolactone (PCL) flexural stiffness, but the reduction in stiffness after NaOH etching (ePCL-HAp) was not different from non-etched PCL-HAp. n = 6-7. *p < 0.05. All data are mean ± standard deviation. HAp was 20 wt%.
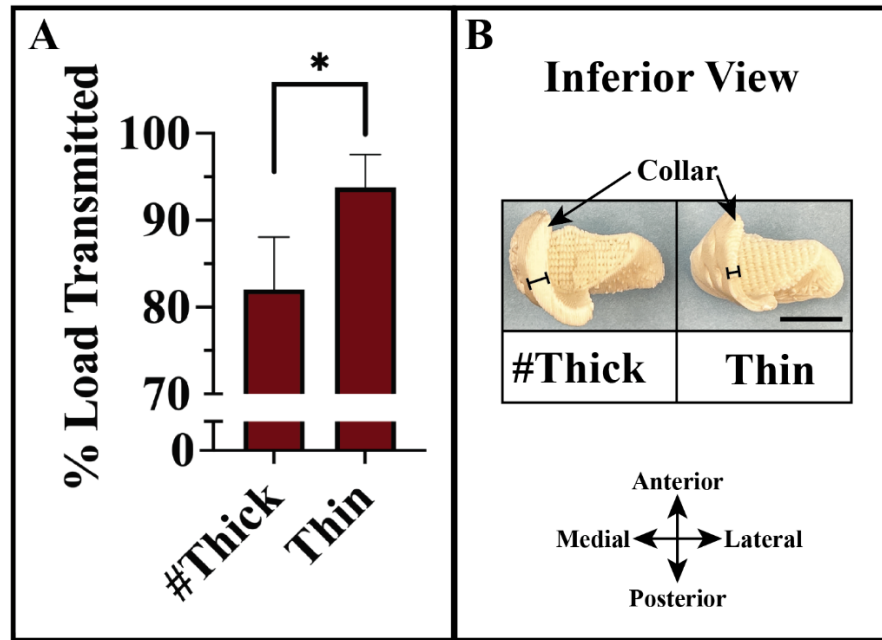
Figure 4.6: Aim 2 Evaluation of the load transmitted through the condyle to the underlying bone geometry.

(A) As the collar region of the prosthesis was reduced in thickness from approximately 5 mm (thick) to 3 mm (thin), the transmitted load increased by over 10%. **(B)** Thick collar prosthesis. **(C)** Thin collar prosthesis. %Load transmitted = $F_{transmitted}$ / $F_{applied}$ * 100%. # Thick specimen was the design parameter selected for the prostheses implanted in the pilot animal study. *$p <$ 0.05. n=4.
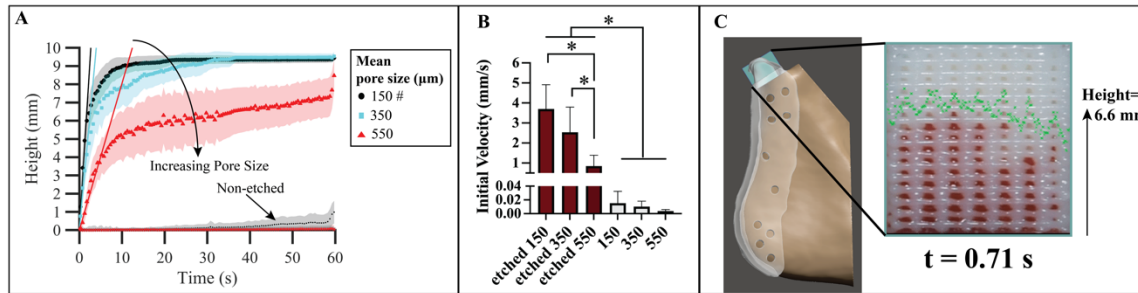
Figure 4.7: Aim 2 3D-printed polycaproloactone-hydroxyapatite (PCL-HAp) composite scaffold exhibited capillary rise of whole blood.

(A) The rates decreased as pore sizes increased (150, 350, 550 μm). Negligible capillary rise was exhibited by scaffolds that were not etched (green plot with arrow). A line was fit to the initial data points to calculate each group's initial velocities. **(B)** The etched group initial velocities decreased by 31% and 77% for 350 and 550 μm groups from 3.7 ± 1.2 mm·s^{-1} for the 150 μm group. Negligible capillary rise was detected in the non-etched groups (gray bars). Differences were exhibited among all groups except within nonetched groups (gray bars) and the etched 150 and 350 groups. **(C)** The prosthesis was designed with a 150 μm porous structure inside the condylar head. Representative specimen illustrated digital measurement of whole blood height (green "Xs"). # denotes 150 μm pore size used in the animal study. Data points are ensemble averages, bands are standard deviations. *$p < 0.05$. n=7.

Figure 4.8: Aim 2 Assessment of bone with MicroCT data prepared from each subject 6 months after implantation.
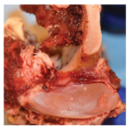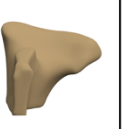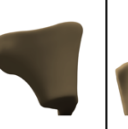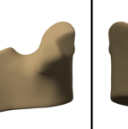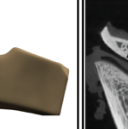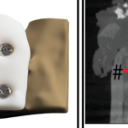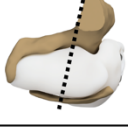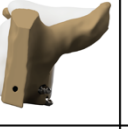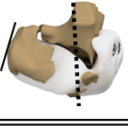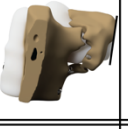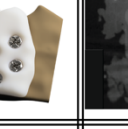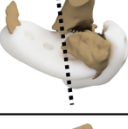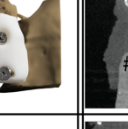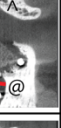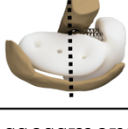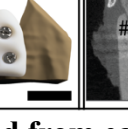
Gross images were captured from the tissue's superior viewpoint with the camera pointed from the superior perspective. Renderings for each case were displayed with the view direction listed across the top row (superior, anterior, posterior, medial, and lateral). In each case, bone growth was exhibited around the prosthesis condyle, but not inside the condyle's porous region. Bone resorption was observed in all cases with more pronounced bone loss in groups with the hydrogel (D, and E). The control group is shown as the mirror image of the left condyle from subject C to facilitate visual comparison with the experimental group

165

right condyles. In the CT images, the prosthesis and ramus bone were labeled as * and #, and displayed as white and brown, respectively, in the renderings. The approximate distance between the prosthesis collar and bone was shown with a red line superimposed on the CT sections. The approximate lengths were 6.0, 5.6, and 2.6 mm for non-hydrogel groups A, B, and C, and 7.2, 9.2 mm for groups D and E, respectively. MicroCT imaging volume was focused on the condylar region, though the prostheses extended down to the angle of the mandible. Scale bar: 10 mm.
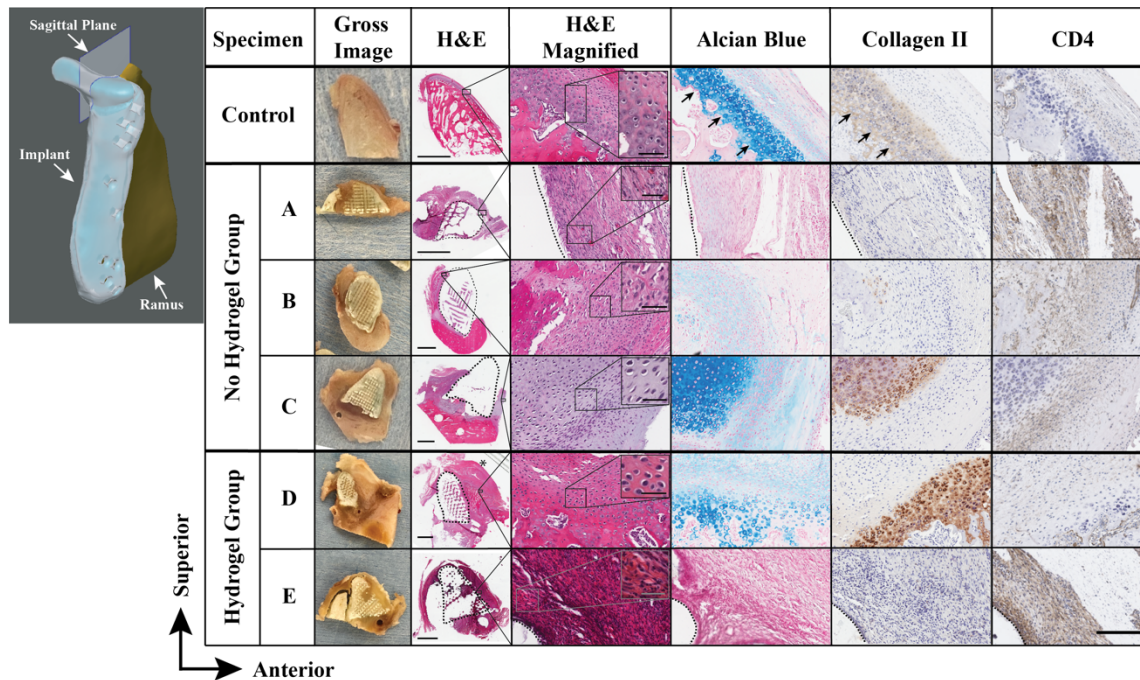
Figure 4.9: Aim 2 Assessment of neocartilage and bone formation with histology and immunohistochemistry from selected regions of sagittal condyle sections.

Note in the healthy control tissue the deeper hyaline-like cartilage layer (black arrows) below the overlying proliferative and superior fibrous zones. Cases C (without hydrogel) and D (with hydrogel) exhibited evidence of cartilage-like soft tissue regeneration. Alcian blue staining was exhibited by the control mandibular condylar cartilage's deep layer, and in subjects A, B, C, and D with the richest experimental tissue staining in C and D. Collagen II staining was exhibited by the control specimen's deep layer in addition to subjects C and D on the anterior, articulating surfaces. Subject B exhibited faint collagen II staining in the pericellular matrix. Generally, high collagen II staining was localized to the pericellular matrix. Specimens A and E exhibited darker CD4 staining for helper T cells than the other cases, suggesting a variable innate immune response. Little to no CD4 staining was exhibited by the contralateral control condyle. The disc fused to the surface of condyle D shown with *. H&E: hematoxylin and eosin. Gross images presented the tissue sections prior to slide mounting. Illustration of ramus and condylar

prosthesis (left panel) with sagittal plane was provided for orientation purposes. Dashed lines represent prosthesis border. Scale bars: 3 mm for H&E, 50 μm for insets, and 200 μm (lower right) for all other images.

Specimen		Gross Image	H&E	H&E Magnified	Alcian Blue	Overall Gross Score
Control						3.9 ± 0.3
No Hydrogel Group	**A**					1.3 ± 1.5
	B					1.3 ± 1.0
	C					4.0 ± 0.0
Hydrogel Group	**D**	No Data	No Data		No Data	No Data
	E					1.0 ± 1.7
Orientation		M ↔ L (A/P)		P ↔ A (S/I)		
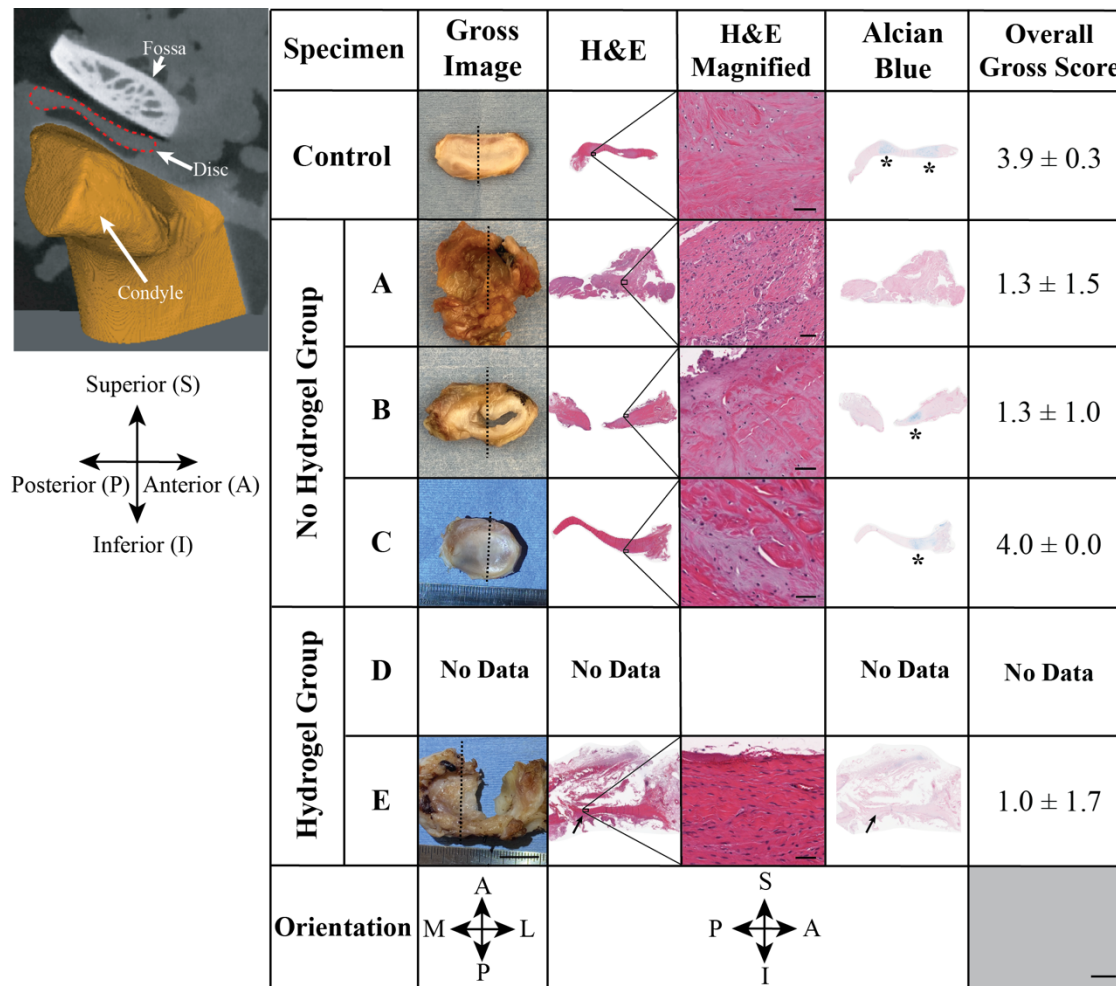
Figure 4.10: Aim 2 Assessment of TMJ disc structure with histology. Disc outcomes were variable from nearly pristine to perforated.

169

MicroCT after tissue resection illustrates approximate disc location relative to condyle and fossa. Gross images exhibit changing sizes among disc tissues. Subjects A and E exhibited granulation tissue, with some remaining discernable disc tissue in subject E (arrow). Subject C disc tissues matched the histological structure of the control, though the aspect ratio appears to have changed to a shorter medial-lateral and longer anteroposterior than control disc. In subject D, the disc fused to the condyle, hence there was no data. Alcian blue staining was positive in a distinct band in the control disc (*). Alcian blue staining persisted in B and C, though was largely absent in A and E. The overall gross morphology score was highest in subject C. Details regarding scoring information can be found in supplemental table. Orientations were medial (M), lateral (L), anterior (A), posterior (P) for the gross images; superior (S), and inferior (I) for histology images. Control displayed as mirror image for comparison with experimental data contralateral side of jaw. Dashed lines denote sectioning. Hematoxylin and eosin (H&E) staining. Scale bars are 10 mm for gross images, and 3 mm for histology.

A **Hourglass Design**

Illustration	Structure Label	d (mm)
	20°	2.4
	30°	1.7
	40°	0.8

B **Interface Shear Computer Model**

- Fixed-3
- Prescribed-1
- Fixed-1-2-3 Sliding

F_2

2 mm

F_1

Hydrogel

Hourglass tube

C **Interface Shear Experiment**

F_2

2 mm

Hydrogel

F_1

Hourglass

sample base

3
1
2

D **Scaffold Compression**

40° hourglass infill architecture

Crosshatch infill architecture

Top view

F_3
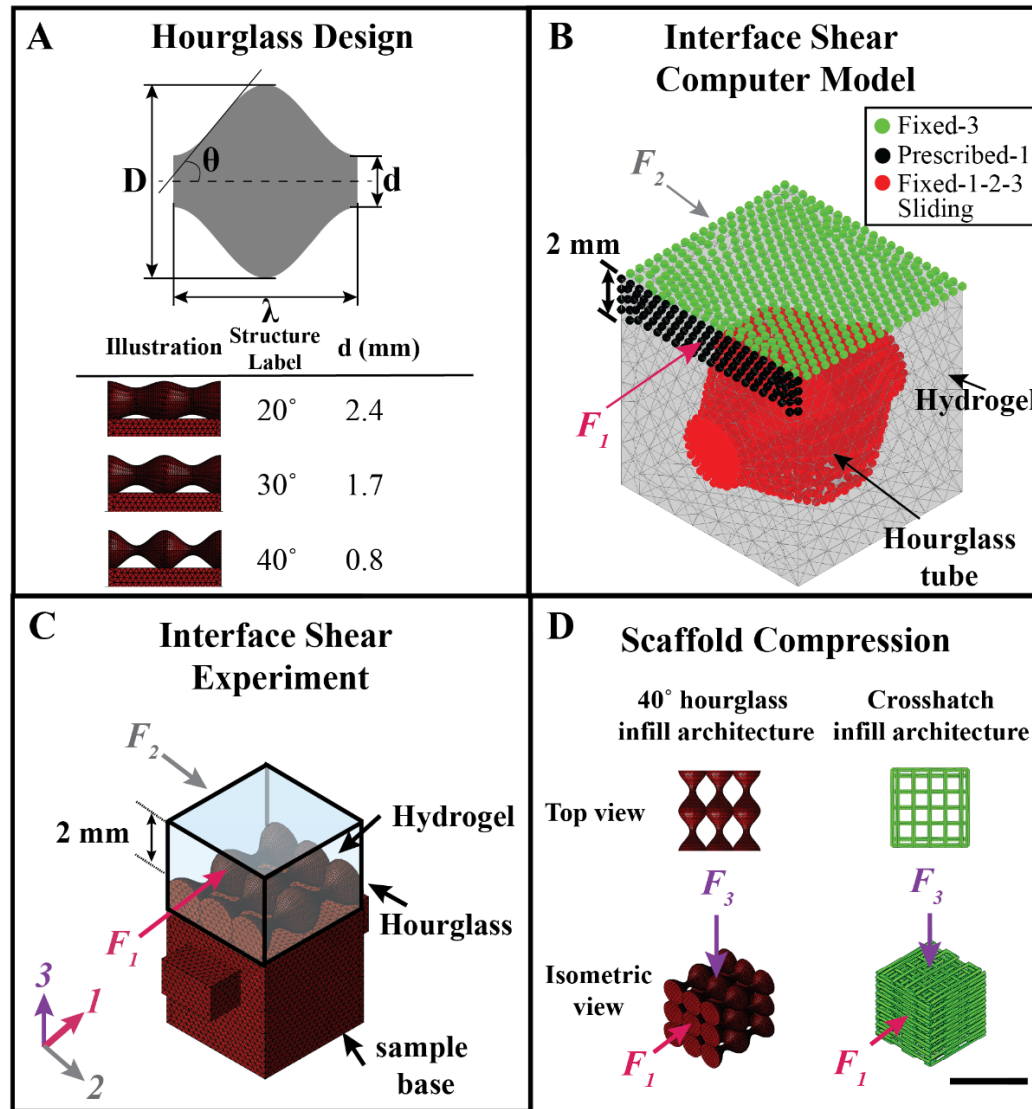
F_3

Isometric view

F_1

F_1

Figure 5.1: The transversely isotropic hourglass feature designed to enhance mechanical performance in biphasic scaffolds.

(A) The hourglass design was defined by four parameters: (1) Maximum diameter: **D**, (2) maximum angle with the longitudinal axis: θ, (3) node-node distance: λ, and (4) minimum diameter: **d**. Three specific geometries were selected to investigate interface shear stress behaviors by holding constant **D** = 3.5 mm and λ = 5 mm. The angle, θ, was varied by changing the minimum diameter. **(B)** The model's boundary conditions were defined such that the hourglass geometry was fixed in space, and a load was applied to the hydrogel in either the 1- or 2-direction to match the experimental conditions, with the upper boundary constrained from moving in the 3-direction. **(C)** Interface shear experiments were performed on the hourglass geometries by infilling a hydrogel. The hydrogel phase was laterally loaded in the 1- or 2-direction until failure. **(D)** 3D prints based on a 40° hourglass (transversely isotropic structure with identical 2- and 3-directions) and a crosshatch pattern (transversely isotropic structure with identical 1- and 2-directions) with comparable porosities, where the 1- and 3-directions were compressed as illustrated.
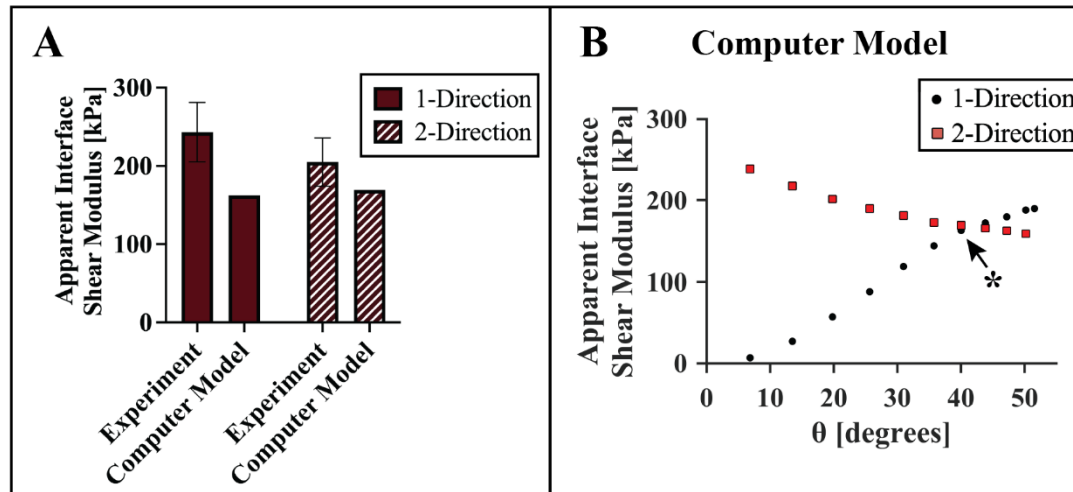
Figure 5.2: Interface shear computer model validation and design investigation.

(A) Comparison of the θ = 40° single hourglass tube computer model with the cartilage-matrix hydrogel interface shear experiment's apparent interface shear modulus. The Ogden model was fitted to the hydrogel's compressive behavior as previously described [31]. **(B)** Apparent interface shear modulus for 21 models with different θ loaded in the 1- and 2-directions. As θ increased, the apparent interface shear modulus increased in the 1-direction, but decreased in the 2-direction. *θ = 40° angle where the model predicted similar, high apparent interface shear moduli for both directions. (Experiments were n = 6; mean ± standard deviation, computer simulations were performed once for each group).
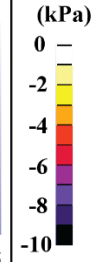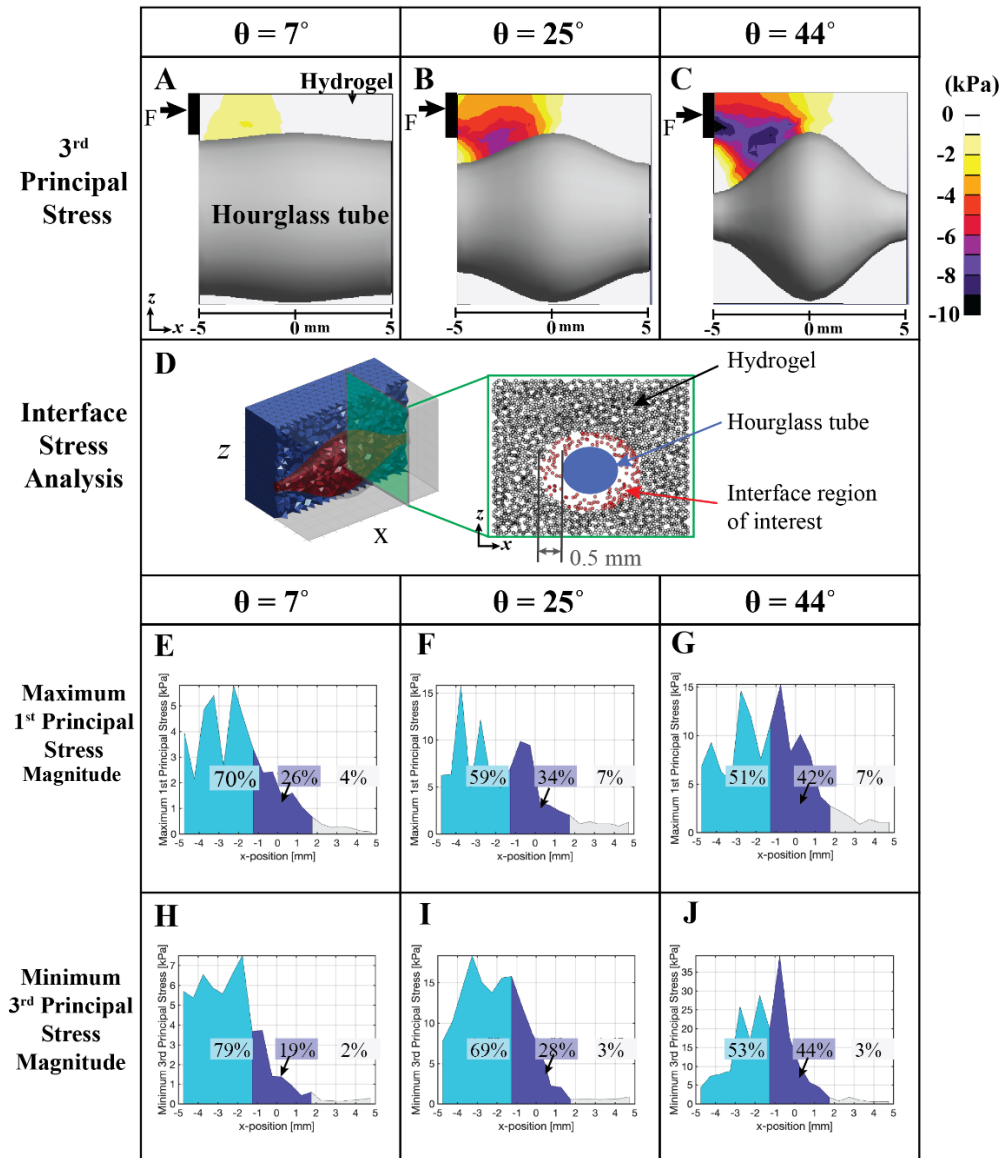
Figure 5.3: Stress analysis suggested the hourglass geometry exhibited a geometric shift in interface stress from left to center, away from the loading crosshead.

(**A-C**) 3rd principal stress (i.e., σ_3) magnitudes increased with increasing θ. (**D**) Analysis of the interface stress was performed in cross-sections from left to right along the x-direction (i.e., 1-direction) within a 0.5 mm radial region of interest surrounding the hourglass tube. (**E-G**) Within the interface region, the maximum first principal stress increased in the central region (dark blue) and decreased in the left region (light blue) with increasing θ. The maximum 1st principal stress (i.e., σ_1) did not exhibit large changes in magnitude from θ = 25˚ to 44˚. (**H-J**) The minimum 3rd principal stress magnitude redistributed to the center region with areas increasing from 19% to 44% of the total area with increasing θ. The 3rd principal stress magnitude additionally increased as θ increased from 25˚ to 44˚, in contrast with the 1st principal stress. Note: $\sigma_3 < \sigma_2 < \sigma_1$, where a negative value represents compression and a positive value represents tension (i.e., σ_3 represents the largest compressive stress magnitude).
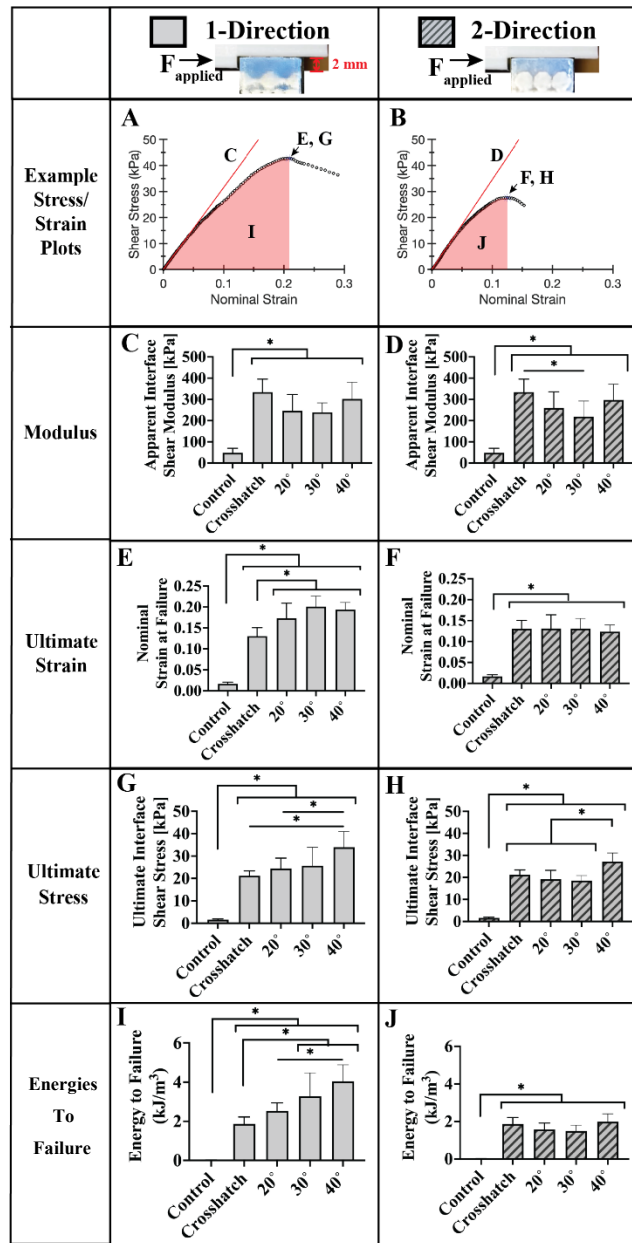
Figure 5.4: Interface shear test performed with 5% agarose hydrogel infilled into the interface.

Three hourglass tubes were aligned side-by-side on the substrate. The shear test was applied in two orthogonal directions either parallel with (i.e., 1-direction) or perpendicular to (i.e., 2-direction) the hourglass's long axis. The hourglass interface exhibited enhanced biomechanical behavior compared to smooth control and traditional crosshatch substrates. The 1- and 2-directions of the crosshatch were arbitrary due to isotropy in that plane. (**A**, **B**) Representative plots illustrated the shear stress vs. nominal strain plots with labels for the plotted features analyzed. (**C, D**) All of the scaffolds with an interface feature exhibited higher apparent interface shear moduli than the control in both 1- and 2-directions of loading. (**D**) The crosshatch pattern exhibited a stiffer behavior than the 30˚ hourglass feature in the 2-direction. (**E, F**) Strain at failure was higher in all three of the hourglass designs compared to both control and crosshatch surfaces, but only in the 1-direction. (**G, H**) The ultimate interface shear stress in 40˚ hourglass scaffolds was higher than control and crosshatch substrates for both 1- and 2-directions. (**I**) In the 1-direction, the energies to failure exhibited by 30˚ and 40˚ interface scaffolds were higher than both control and crosshatch scaffolds. (**J**) Although no energy to failure differences in the 2-direction were exhibited by the scaffolds with the interface features, all of the scaffolds exhibited higher energies to failure than the control. The substrate was 3D-printed with polylactic acid (PLA). n = 6; *p < 0.05; all data were mean ± standard deviation.
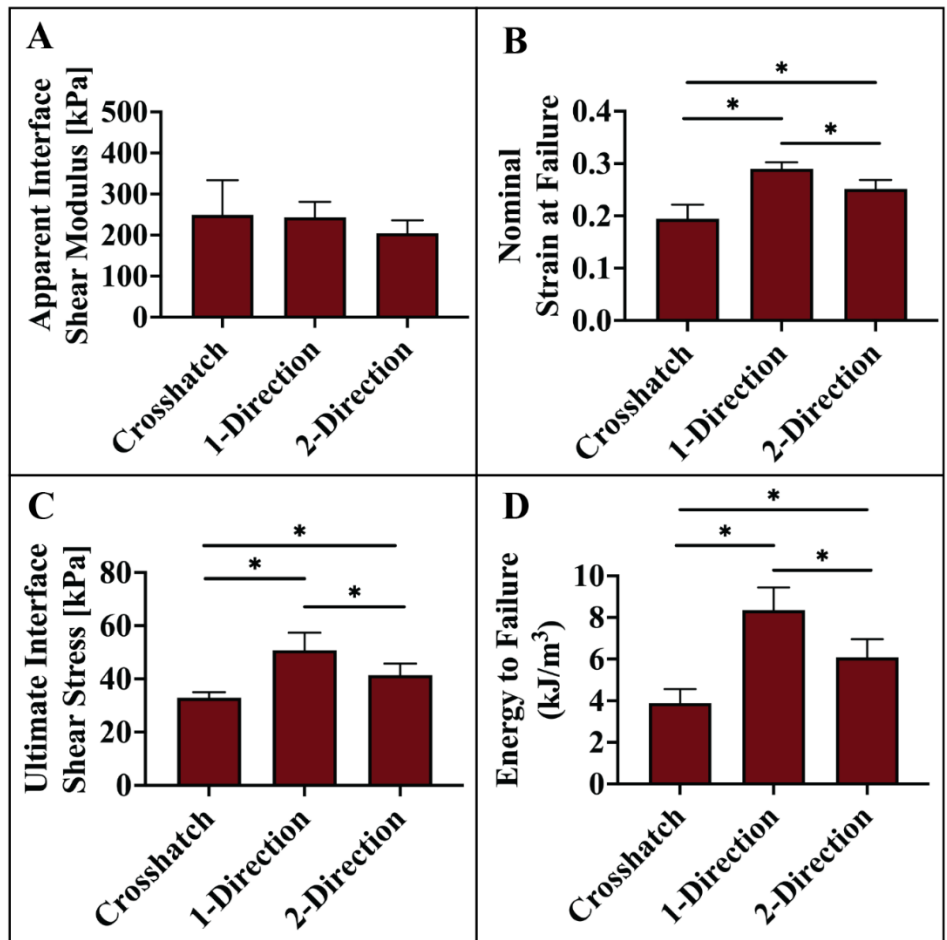
Figure 5.5: Interface shear tests with θ = 40° hourglass interface and cartilage-matrix based hydrogel infill.

(A) Although there were no differences among the apparent interface shear moduli, all three of the other parameters revealed higher values in *both* directions for the hourglass architecture compared to the crosshatch architecture, i.e., **(B)** strain at failure, **(C)** ultimate interface shear stress, and **(D)** energy to failure. The hydrogel was comprised of 4% w/v pentenoate-modified hyaluronic acid, 20% w/v polyethylene glycol, and 15% w/v devitalized cartilage. The substrate was 3D-printed with polylactic acid (PLA). n = 6; *p < 0.05; all data are mean ± standard deviation.
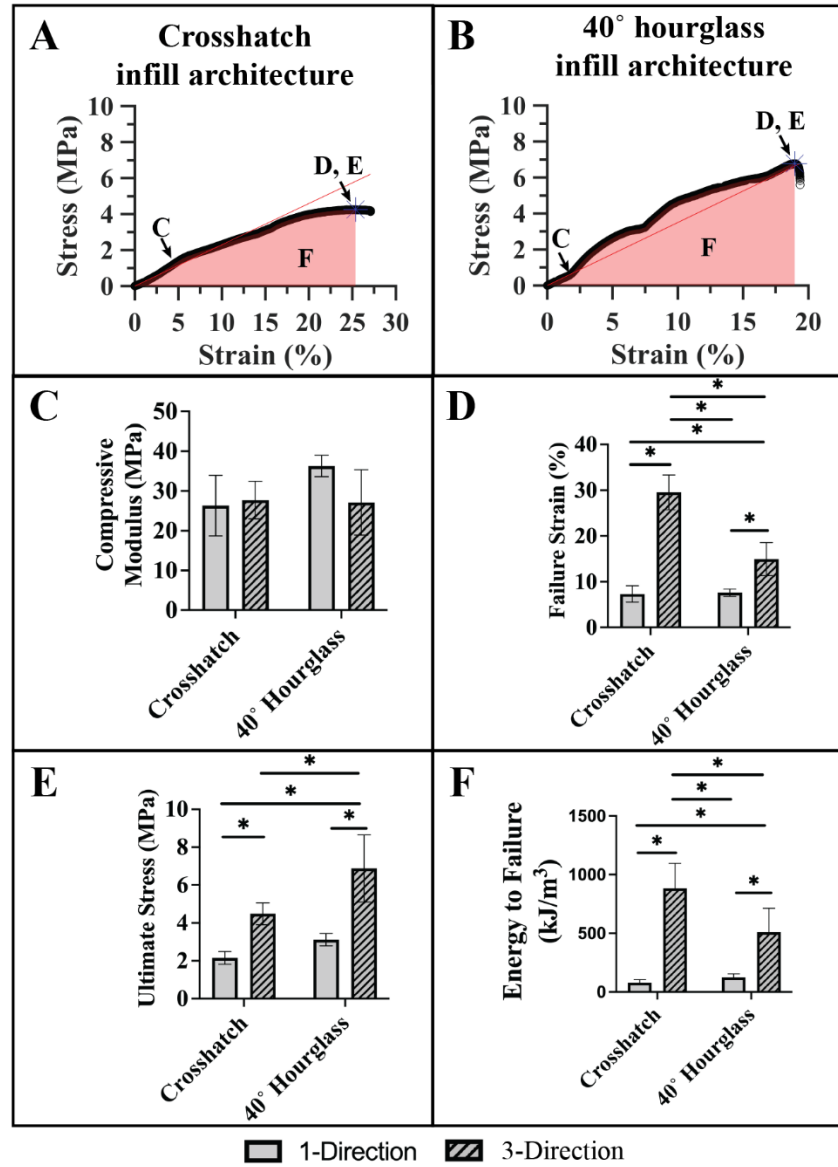
Figure 5.6: Compression testing of the hourglass architecture compared to a crosshatch architecture, controlled for porosity.

The hourglass pattern as an infill architecture exhibited higher ultimate compressive stress than the typical crosshatch infill. (**A, B**) Representative 3-direction stress vs. strain plots for the crosshatch and hourglass architectures, respectively. (**C**) There were no significant differences in compressive modulus. (**D**) Failure strains were higher in the 3-direction for both scaffolds and highest for the crosshatch print. (**E**) The ultimate stress was higher for the hourglass architecture in both 1- and 3-directions of loading. (**F**) The energy to failure was higher for the crosshatch architecture than the hourglass architecture in the 3-direction. The architecture was 3D-printed with polylactic acid (PLA). Scale bar: 10 mm; n = 6; *$p < 0.05$; data are mean $\pm$ standard deviation.
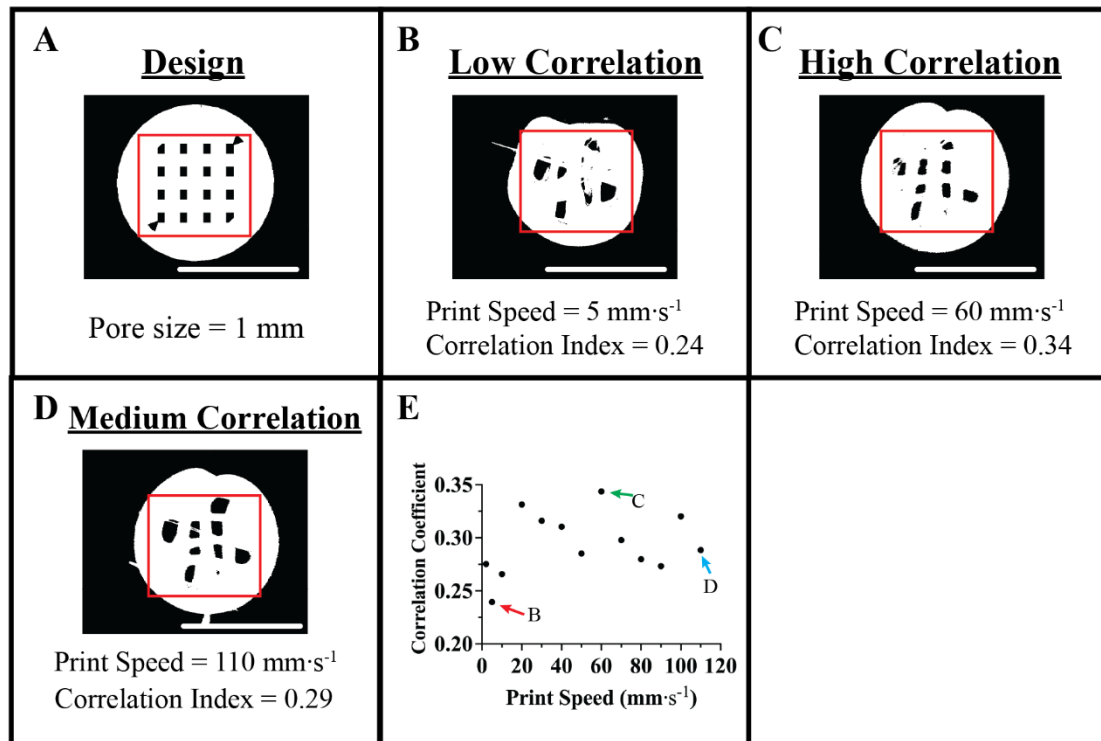
Figure 6.1: Aim 4 Porous polycaprolactone scaffold quality was evaluated with different 3D-printer print speeds.

A correlation coefficient was used to determine how well the printed scaffold correlated with the digital design. **(A)** Binary image of the computer-generated scaffold design. **(B)** Example image of a print fabricated at a low speed resulting in a low correlation coefficient. **(C)** Printed scaffold printed at a higher speed resulting in a higher correlation coefficient. **(D)** At the high speed of 110 110 mm·s⁻¹ the correlation was in the mid-range. **(E)** Plot of correlation coefficients that resulted from a range of print speeds from 2 to 110 mm·s⁻¹. Representative images in panels B, C, and D are marked with red, green, and blue arrows in panel E, respectively. (n=1, Scale bar = 5 mm)
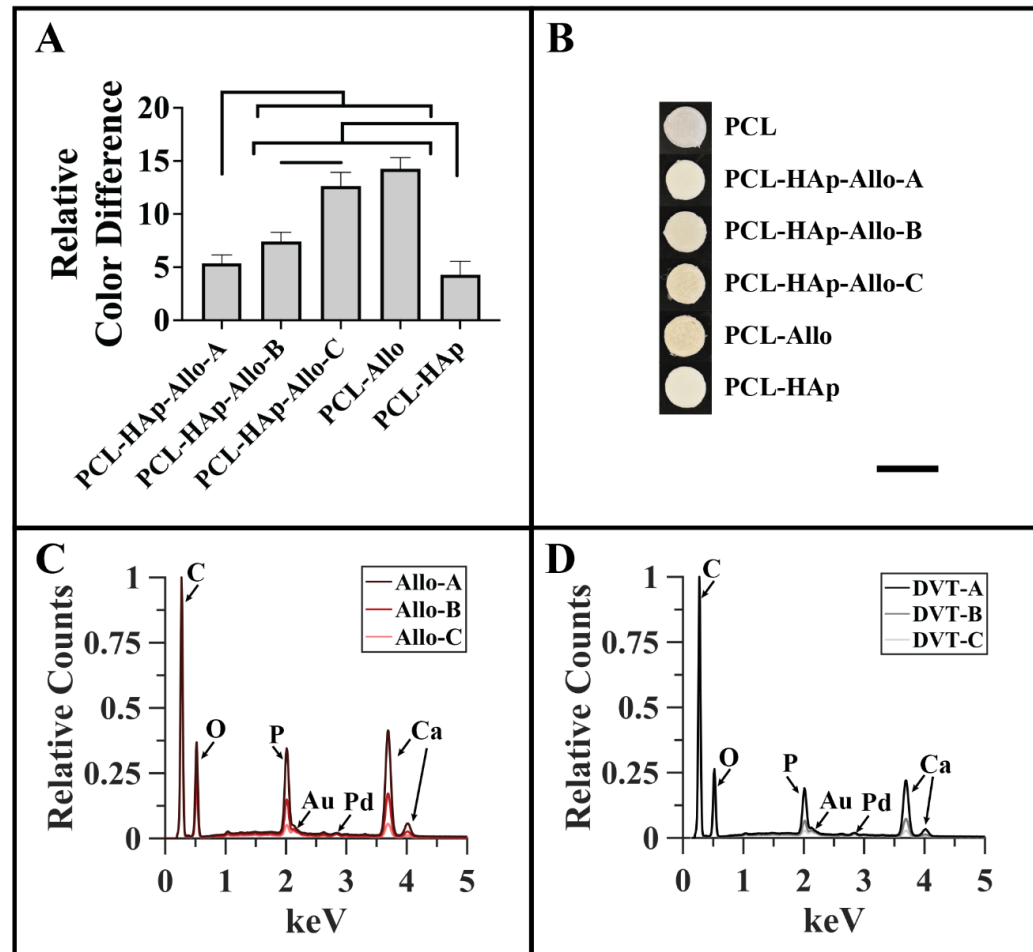
Figure 6.2: Aim 4 Characterization of 3D-printed PCL functionalized with HAp, with either Allo, or DVT material

(**A**) Color differences relative to pure PCL were heightened with additional Allo. HAp is visually similar in color (white) to PCL, whereas Allo has more of a yellowish color, so the Allogro content is more clearly visualized in PCL than HAp. (**B**) Representative images of material 3D-prints. (**C**) X-ray dispersive spectrogram exhibited high, medium, and low Ca signals

for 3D-printed Allo-A, -B, and -C, respectively. **(D)** X-ray dispersive spectrogram exhibited high, medium, and low Ca signals for 3D-printed DVT-A, -B, and -C, respectively. **PCL**: polycaprolactone; **HAp**: hydroxyapatite; **Allo:** Allogro® demineralized bone matrix; **PCL-HAp-DVT-A**: 50/37.5/12.5 w/w%; **PCL-HAp-DVT-B**: 50/25/25 w/w%; **PCL-HAp-DVT-C**: 50/12.5/37.5; **PCL-HAp-Allo-A**: 50/37.5/12.5 w/w%; **PCL-HAp-Allo-B**: 50/25/25 w/w%; **PCL-HAp-Allo-C**: 50/12.5/37.5. **PCL-HAp**: 50/50% w/w; **PCL-HAp-Coat**: 50/50% w/w with a high air pressure blast coating of additional hydroxyapatite. **C**: carbon; **O**: oxygen; **P**: phosphorus; **Au:** gold; **Pd**: palladium; **Ca**: calcium. (n=6 for (A); *p < 0.05; scale bar = 10 mm).
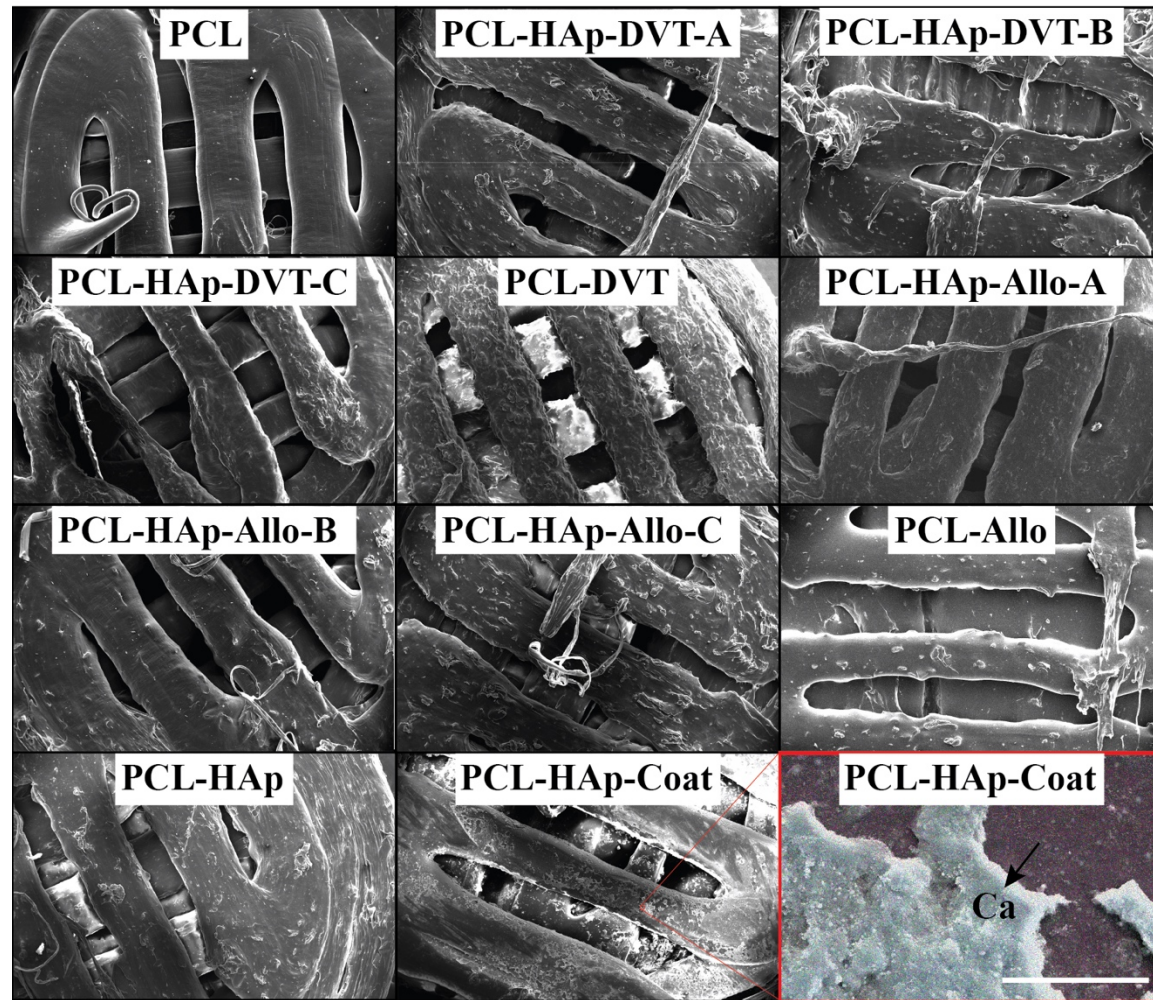
Figure 6.3: Aim 4 Scanning electron micrographs of 3D-printed polycaprolactone (PCL)-based composites.

The surface texture varied from smooth with pure PCL, to rough with PCL-DVT. PCL-HAp-Coat exhibited a layer of Ca-containing material across the surface. **PCL**: polycaprolactone; **HAp**: hydroxyapatite; **Allo:** Allogro® demineralized bone matrix; **DVT:** Devitalized tendon; **PCL-HAp-DVT-A**: 50/37.5/12.5 w/w%; **PCL-HAp-DVT-B**: 50/25/25 w/w%; **PCL-HAp-DVT-C**: 50/12.5/37.5; **PCL-HAp-Allo-A**: 50/37.5/12.5 w/w%; **PCL-HAp-Allo-B**: 50/25/25 w/w%; **PCL-HAp-Allo-C**: 50/12.5/37.5. **PCL-HAp**: 50/50% w/w; **PCL-HAp-Coat**: 50/50% w/w with a high air pressure blast coating of additional hydroxyapatite. **Ca**: calcium. White scale bar: 40 μm for zoomed in PCL-HAp-Coat; Black scale bar: 2 mm for all other panels.
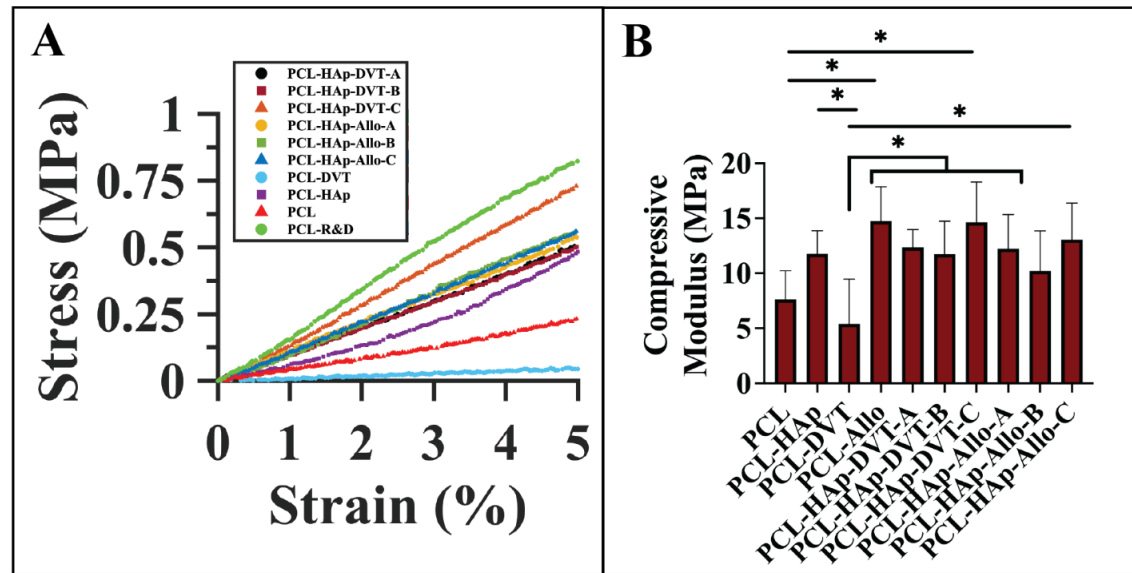
Figure 6.4: Aim 4 Compressive elastic moduli in polycaprolactone (PCL) composites comprised of hydroxyapatite (HAp) and/or Allogro® (Allo) were heightened compared to pure PCL or PCL-Devitalized Tendon (DVT).

(A) Representative stress-strain curves of each group. **(B)** Compressive moduli of 3D-printed solids. The PCL-DVT composite exhibited a more compliant compressive modulus than all HAp-containing groups except PCL-HAp-Allo-B. The PCL-Allo and PCL-HAp-DVT-C groups exhibited higher stiffness than PCL. **PCL:** polycaprolactone; **HAp**: Hydroxyapatite; **DVT:** Devitalized tendon; **Allo**: Allogro® demineralized bone matrix; PCL-Allo was made with a research and development version of Allogro®. All other Allogro®-containing composites were comprised of commercially available Allogro®. **PCL-HAp**: 50/50% w/w; **PCL-DVT:** 50/50% w/w; **PCL-Allo:** 50/50% w/w; **PCL-HAp-DVT-A**: 50/37.5/12.5% w/w; **PCL-HAp-DVT-B**: 50/25/25% w/w; **PCL-HAp-DVT-C**: 50/12.5/37.5% w/w; **PCL-HAp-Allo-A**: 50/37.5/12.5% w/w; **PCL-HAp-Allo-B**: 50/25/25% w/w; **PCL-HAp-Allo-C**: 50/12.5/37.5% w/w. (*$p < 0.05$; n=6).
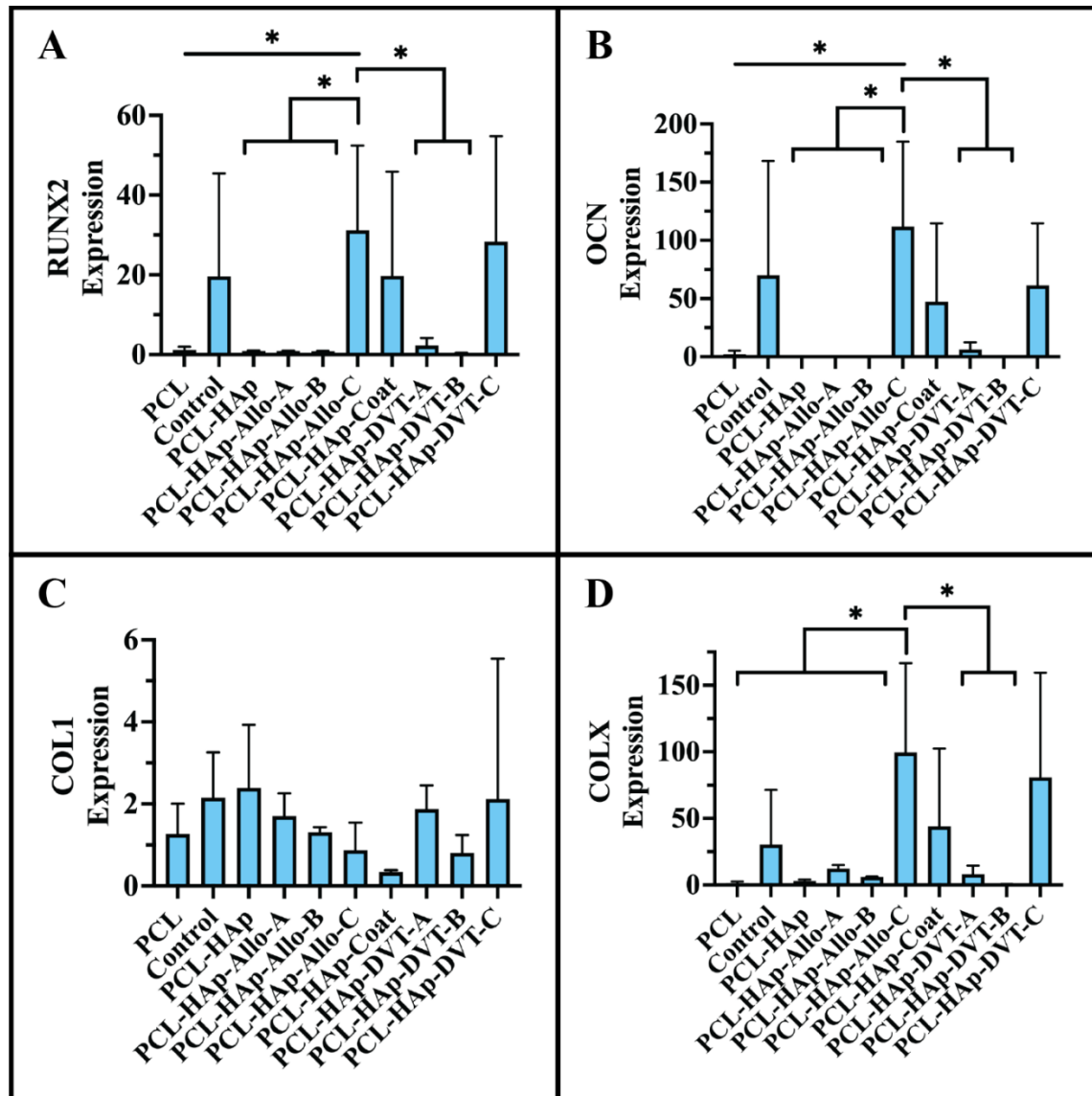
Figure 6.5: Aim 4 Reverse transcription quantitative polymerase chain reaction (RT-qPCR) for osteogenic expression of human bone marrow-derived mesenchymal stem cells (hBMSCs) seeded on porous 3D-printed polycaprolactone (PCL) composites.

Composite PCL-HAp-Allo-C (i.e., high Allo content, with HAp included) exhibited the highest expressions of RUNX2, OCN, and COLX (statistically significant, except with the 2D Control, PCL-HAp-Coat, and PCL-HAp-DVT-C groups). Expression means remained high in the PCL-HAp-DVT-C group and PCL-HAp-Coat. **RT-qPCR**: Reverse transcription quantitative polymerase chain reaction; **hBMSCs**: human bone marrow-derived mesenchymal stem cells **PCL**: polycaprolactone; **Control**: Cells cultured on tissue culture treated polystyrene; **HAp**: hydroxyapatite; **Allo**: Allogro® demineralized bone matrix; **DVT**: Devitalized tendon; **PCL-HAp-DVT-A**: 50/37.5/12.5% w/w; **PCL-HAp-DVT-B**: 50/25/25% w/w; **PCL-HAp-DVT-C**: 50/12.5/37.5% w/w; **PCL-HAp-Allo-A**: 50/37.5/12.5% w/w; **PCL-HAp-Allo-B**: 50/25/25% w/w; **PCL-HAp-Allo-C**: 50/12.5/37.5% w/w. **PCL-HAp**: 50/50% w/w; **PCL-HAp-Coat**: 50/50% w/w with a high air pressure blast coating of additional hydroxyapatite.

Appendix B: Tables

Chapter 1: No Tables

Chapter 2: Tables 2.1

Chapter 3: Table 3.1

Chapter 4: Tables 4.1-4.3

Chapter 5: No Tables

Chapter 6: No Tables

Chapter 7: No Tables

Table 2.1: Interface Integration Strategies and Interface Evaluation Methods

Reference	Fabrication Method	Interface Integration Strategy	Material	Cells	Interface Composition	Interface Evaluation	Interface Strength
Allan *et al*. 2007	Cast with gravity sintering, *in vitro* cell seeding	Tissue culture	Porous calcium polyphosphate, Neocartilage	Bovine metacarpal chondrocytes	Calcified zone	Interface shear strength, Histology	2 N
Broom *et al*. 1996	*ex vivo* tissue	Native tissue	Bovine patellar osteochondral tissue	Chondrocytes	Osteochondral tissue	Surface-constrained impact interface shear, Histology	6.4 MPa
Brown *et al*. 2021	Molded	Tissue culture, Mechanical interlocking	Hydroxyapatite Self-assembled neocartilage	Dedifferentiated juvenile ovine articular chondrocytes	Interdigitated neocartilage	Lap shear, Histology	83 kPa
Flachsmann *et al*. 1995	*ex vivo* tissue	Native tissue	Bovine patellar osteochondral explant	Chondrocytes	Osteochondral tissue	Impact interface shear, Photomicrography, Histology	19 MPa

NP: nucleus pulposus, GelMA: gelatin methacrylate, PVA: polyvinyl alcohol, PLLA: poly-L-lactic acid, PLGA: polylactic-co-glycolic acid, Col: collagen, HA: hyaluronic acid, DA: diacrylate, PBA: 3-aminophenylboronic acid

Reference	Fabrication Method	Interface Integration Strategy	Material	Cells	Interface Composition	Interface Evaluation	Interface Strength
Hamilton *et al.* 2006	Cast with gravity sintering, *in vitro* cell seeding	Tissue culture	Porous calcium polyphosphate, Neocartilage	NP Cells, Bovine metacarpal-phalangeal articular cartilage cells	Interdigitated neocartilage	Interface shear, Histology, SEM	1.8 N
Lee *et al.* 2024	Injectable spheroid-laden hydrogel	Chemical cross-linking	GelMA seeded with chondrogenically induced spheroids, GelMA seeded with osteogenically induced spheroids	Human adipose-derived stem cells	Crosslinked hydrogel bilayer and tissue culture	Lap shear, Peel test	4-6 MPa

NP: nucleus pulposus, GelMA: gelatin methacrylate, PVA: polyvinyl alcohol, PLLA: poly-L-lactic acid, PLGA: polylactic-co-glycolic acid, Col: collagen, HA: hyaluronic acid, DA: diacrylate, PBA: 3-aminophenylboronic acid

Reference	Fabrication Method	Interface Integration Strategy	Material	Cells	Interface Composition	Interface Evaluation	Interface Strength
Lima et al. 2008	Cored bone, Electron discharge machining, Infilled hydrogel construct	Tissue culture Mechanical interlocking	Porous tantalum, Bone, Cell-seeded agarose	Bovine metacarpal chondrocytes	Interdigitated neocartilage	Interface shear, Histology	1.4 N
Liu et al. 2020	Infilled	Chemical bonding	Annealed PVA	N/A	Hydrogen bonding	Peel test	1000 J•m^{-2}
Nover *et al.* 2015	Infilled	Mechanical interlocking	Porous titanium, Cell-seeded agarose	Canine articular chondrocytes	Interdigitated porous region and impermeable interface	Interface shear, Fluorescence microscopy	0.6 N
Reindel *et al.* 1995	*ex vivo* tissue	Tissue culture	Calf and adult articular cartilage explants	*in situ* chondrocytes	Cultured cartilage matrix under weight	Lap shear	27 kPa

NP: nucleus pulposus, GelMA: gelatin methacrylate, PVA: polyvinyl alcohol, PLLA: poly-L-lactic acid, PLGA: polylactic-co-glycolic acid, Col: collagen, HA: hyaluronic acid, DA: diacrylate, PBA: 3-aminophenylboronic acid

Table 2.1 Continued... Interface Integration Strategies and Interface Evaluation Methods

Reference	Fabrication Method	Interface Integration Strategy	Material	Cells	Interface Composition	Interface Evaluation	Interface Strength
Romito and Ameer. 2006	Infilled	Solvent bonding, Tissue culture	PLLA mesh, PLGA mesh, PLLA solid core	Bovine articular chondrocytes	Porous non-woven mesh	Lap shear, SEM	44 kPa
Scotti *et al.* 2009	Cored out tissue slabs and cylinders	Tissue culture	Col I/III (Chondro-Gide) scaffold, Devitalized bovine cancellous bone cylinders (Tutobone)	Human articular chondrocytes	Fibrin glue	Peel test, Photoimaging, Histology	0.6 N
Sitterle *et al.* 2008	*ex vivo* cartilage tissue	Chemical bonding	Light bonded articular cartilage	*in situ* chondrocytes	Light-cured cartilage	Lap shear	46 kPa
Wang *et al.* 2011	Infilled	Tissue culture	Non-woven PLLA meshes	hUCMSCs	Matrix from human umbilical cord mesenchymal stem cells	Histology	N/A
Yu *et al.* 2020	Injectable hydrogel	Chemical bonding	HA-furan-DA, HA-furan-PBA, Porcine cartilage	Acellular	Phenyl boronate bond	Lap shear, SEM	6 kPa

NP: nucleus pulposus, GelMA: gelatin methacrylate, PVA: polyvinyl alcohol, PLLA: poly-L-lactic acid, PLGA: polylactic-co-glycolic acid, Col: collagen, HA: hyaluronic acid, DA: diacrylate, PBA: 3-aminophenylboronic acid

Table 2.2: Interface Integration Applied to 3D-Printed Scaffolds

Reference	3D-printing Method(s)	Interface Integration Strategy	Material	Cells	Interface Composition	Interface Evaluation	Interface Strength
Choe *et al*. 2022	Extrusion 3D-printed	Mechanical interlocking	GelMA, PCL, PEGDA	Acellular	Patterned porous layer	Interface shear, FE model	63 kPa
Diloksumpan *et al.* 2020	Melt electrowriting, Extrusion 3D-printed	Mechanical interlocking	C-PCaP, NC-PCaP, GelMA, PCL	ACPCs	Melt electrowritten mesh	Interface shear, SEM	18 kPa

GelMA: gelatin methacrylate, PCL: polycaprolactone, PEGDA: polyethylene glycol diacrylate, C-PCaP: crosslinkable printable tricalcium phosphate, NC-PCaP: non-crosslinkable printable tricalcium phosphate, ACPCs: articular cartilage-derived chondroprogenitor cells

Table 2.2 Continued... Interface Integration Applied to 3D-Printed Scaffolds

Reference	3D-printing Method(s)	Interface Integration Strategy	Material	Cells	Interface Composition	Interface Evaluation	Interface Strength
Lee *et al.* 2010	Extrusion 3D-printed, Syringed	Mechanical interlocking	PCL, Hydroxyapatite, Col I	Acellular	Anatomical geometry with interconnecting microchannels	Histology, Fluorescence microscopy	N/A
Li *et al.* 2018	Extrusion 3D-printed	Solvent bonding	PLGA, β-TCP, Bovine cartilage matrix	Bovine BMSCs	Compressed calcified layer	SEM, Micro-CT, Shear (with PMMA adhesive)	110 kPa
Rhee *et al.* 2016	Extrusion 3D-printed	Collagen network self-assembly	Col I	Bovine meniscal fibrochon drocytes	Self-assembled collagen network	Confocal reflectance with fluorescent microbead markers	N/A

SEM: scanning electron microscope, Col: collagen, PLGA: polylactic-co-glycolic acid, β-TCP: β tricalcium phosphate,

Table 2.2 Continued... Interface Integration Applied to 3D-Printed Scaffolds

Reference	3D-printing Method(s)	Interface Integration Strategy	Material	Cells	Interface Composition	Interface Evaluation	Interface Strength
Shanjani *et al.* 2015	SLA 3D-printed, Extrusion 3D-printed	Mechanical interlocking	PCL, PEGDA	ATCC, HUVECs	300 μm PCL x 100 μm PEGDA layered units	Interface shear, SEM, Fluorescence Microscopy	8 kPa
Zhang *et al.* 2015	Infilled substrate, SLA 3D-printed hydrogel	Mechanical interlocking	PEGDA, β-TCP	Acellular	Interdigitating porous microstructure	Interface shear, SEM	340 kPa

GelMA: gelatin methacrylate, PCL: polycaprolactone, PEGDA: polyethylene glycol diacrylate, C-PCaP: crosslinkable printable tricalcium phosphate, NC-PCaP: non-crosslinkable printable tricalcium phosphate, ACPCs: articular cartilage-derived chondroprogenitor cells, SEM: scanning electron microscope, Col: collagen, PLGA: polylactic-co-glycolic acid, β-TCP: β tricalcium phosphate, BMSCs: bone marrow stem cells, CT: computed tomography, PMMA: polymethylmethacrylate, PVA: polyvinyl alcohol, OP-BMSCs: osteoporosis-derived bone marrow stem cells, SLA: stereolithography, ATCC: C3H10T1/2 mouse mesenchymal stem cells, HUVECs: human umbilical vein endothelial cells

Table 2.3: 3D-Printing Methodologies for Anatomically Shaped Osteochondral Scaffolds

Reference	Anatomy	Osteal Phase Material	Chondral Phase Material	Phase Assembly Method	3D-printing Method	Overall Size (mm³)
Brown *et al.* 2021	Medial Femoral Condyle	CAD/CAM milled and sintered HAp	Juvenile ovine articular chondrocyte self-assembled sheet	Phases were assembled under a 20 g weight in tissue culture	CAD/CAM subtractive manufacturing of substrate, Polyjet printed molds	31 x 14 x 10
Daly and Kelly. 2019	Tibial Plateau	PCL-reinforced GelMA seeded with MSCs derived from porcine femoral shaft	PCL-reinforced GelMA seeded with 3:1 ratio of BMSC:CC cells derived from porcine femoral articular cartilage	Phases were co-printed	Fixed deposition modeling for PCL framework, Inkjet bioprinting for cell-laden hydrogel	42 x 10 x 21

PCL: polycaprolactone, HAp: hydroxyapatite, BMSC: bone marrow mesenchymal stem cell, PGA: polyglycolic acid, PLA: polylactic acid, CC: chondrocyte, PHA: pentenoate-modified hyaluronic acid, PEGDA: polyethylene glycol diacrylate, DVC: devitalized cartilage, MSC: bone marrow-derived stromal cell, GelMA: gelatin-methacrylate, CAD: computer-aided design, CAM: computer-aided manufacturing

Table 2.3 Continued... 3D-Printing Methodologies for Anatomically Shaped Osteochondral Scaffolds

Reference	Anatomy	Osteal Phase Material	Chondral Phase Material	Phase Assembly Method	3D-printing Method	Overall Size (mm^3)
Ding *et al.* 2013	Femoral head	PCL/HAp scaffold seeded with goat tibial condyle marrow BMSCs	PGA/PLA Scaffold seeded with goat knee cartilage chondrocytes	Phases were nonspecifically assembled	Fused deposition modeling	18 x 17 x 15
Mesallati *et al.* 2015	Medial Femorotibial Condyles	Agarose seeded with BMSCs derived from porcine femoral shaft	4:1 ratio of porcine BMSC and CC cultured into a cell sheet	Phases assembled using fibrin gel	Fused deposition modeling to create mold	20 x 20 x 12

PCL: polycaprolactone, HAp: hydroxyapatite, BMSC: bone marrow mesenchymal stem cell, PGA: polyglycolic acid, PLA: polylactic acid, CC: chondrocyte, PHA: pentenoate-modified hyaluronic acid, PEGDA: polyethylene glycol diacrylate, DVC: devitalized cartilage, MSC: bone marrow-derived stromal cell, GelMA: gelatin-methacrylate, CAD: computer-aided design, CAM: computer-aided manufacturing

Table 2.3 Continued... 3D-Printing Methodologies for Anatomically Shaped Osteochondral Scaffolds

Reference	Anatomy	Osteal Phase Material	Chondral Phase Material	Phase Assembly Method	3D-printing Method	Overall Size (mm³)
Nedrelow *et al.* 2023	TMJ Condyle	PHA-PEGDA-DVC Hydrogel	PCL-HAp	Phases assembled by hydrogel infilling to an interlocking substrate and light curing	Fused deposition modeling	20 x 10 x 10
Shim *et al.* 2012	Articular joint head	Alginate seeded with MG63 osteoblasts	Alginate seeded with human nasal septum chondrocytes	Cell-laden hydrogel was co-printed with PCL framework	Fused deposition modeling, Extrusion bioprinting	25 x 25 x 2

PCL: polycaprolactone, HAp: hydroxyapatite, BMSC: bone marrow mesenchymal stem cell, PGA: polyglycolic acid, PLA: polylactic acid, CC: chondrocyte, PHA: pentenoate-modified hyaluronic acid, PEGDA: polyethylene glycol diacrylate, DVC: devitalized cartilage, MSC: bone marrow-derived stromal cell, GelMA: gelatin-methacrylate, CAD: computer-aided design, CAM: computer-aided manufacturing

Table 2.3 Continued... 3D-Printing Methodologies for Anatomically Shaped Osteochondral Scaffolds

Reference	Anatomy	Osteal Phase Material	Chondral Phase Material	Phase Assembly Method	3D-printing Method	Overall Size (mm³)
Visser *et al.* 2013	Distal Femoral Condyle	PCL-supported GelMA-gellan hydrogel	GelMA-gellan hydrogel	Phases were co-printed with a multi-tool printhead	Fixed deposition modeling, Extrusion bioprinting	40 x 35 x 32
Wang *et al.* 2017	TMJ Condyle	PCL/HAp scaffold seeded with BMSCs derived from minipig iliac crest	Cartilage cell sheet, or PGA/PLA scaffold seeded with auricular chondrocytes	Phases were co-printed. PCL stem-shape added to facilitate fixation in a joint	Fixed deposition modeling, Phases assembled with sutures	13 x 11 x 10

PCL: polycaprolactone, HAp: hydroxyapatite, BMSC: bone marrow mesenchymal stem cell, PGA: polyglycolic acid, PLA: polylactic acid, CC: chondrocyte, PHA: pentenoate-modified hyaluronic acid, PEGDA: polyethylene glycol diacrylate, DVC: devitalized cartilage, MSC: bone marrow-derived stromal cell, GelMA: gelatin-methacrylate, CAD: computer-aided design, CAM: computer-aided manufacturing

Table 3.1: Hydrogel Elastic Solid Parameters

Hydrogel	E (kPa)	μ_o (kPa)	$\frac{E}{\mu_o}$ *
PHA	129 ± 13	37 ± 5	3.5 ± 0.2
PHA-PEGDA	174 ± 17	54 ± 5	3.2 ± 0.1
PHA-PEGDA-DVC$_{5\%}$	418 ± 39	109 ± 10	3.8 ± 0.2
PHA-PEGDA-DVC$_{10\%}$	471 ± 30	111 ± 8	4.3 ± 0.1
PHA-PEGDA-DVC$_{15\%}$	504 ± 61	113 ± 16	4.5 ± 0.2

*All groups were significantly different from each other except DVC10 and DVC15. Pentenoate-modified hyaluronic acid (PHA) was 4% w/v, and PEGDA was 20% w/v. n=6-8. $p < 0.05$.

Table 4.1: Gross Morphology Grading Scale for TMJ Disc Evaluation

Group	Specimen	Degeneration	Hypertrophy	Macroscopic Appearance	Overall
Control		3.8 ± 0.6	4.0 ± 0.0	4.0 ± 0.0	3.9 ± 0.3
No Hydrogel	A	1.3 ± 1.5	1.3 ± 1.5	1.3 ± 1.5	1.3 ± 1.5
	B	0.0 ± 0.0	1.0 ± 0.8	1.8 ± 1.5	1.3 ± 1.0
	C	4.0 ± 0.0	4.0 ± 0.0	4.0 ± 0.0	4.0 ± 0.0
Hydrogel	D	No Data	No Data	No Data	No Data
	E	0.8 ± 1.5	0.5 ± 0.6	1.0 ± 1.4	1.0 ± 1.7

Appendix C: Supplementary Material – Chapter 3

The contents of this appendix were previously published as the supplemental material in the Journal of Biomechanics by Nedrelow, Townsend, and Detamore [31].

Supplemental Methods

Swelling and water absorption

Hydrogels were weighed in the following configurations: Immediately after fabrication (initial), after swelling to equilibrium overnight in PBS at 37 ˚C (swollen), and finally after freezing and drying in a lyophilizer (dry). Each weight was then used to calculate the absorption ratio: $m_{swollen}$ / $m_{initial}$, and swelling ratio: $m_{swollen}$ / m_{dry} (n=6).

Supplemental Results

Hydrogel absorption and swelling

Absorption ratios were 90 to 110% higher than PHA with the addition of PEGDA ($p < 0.05$) (**Supp. 3.1 B**). PHA hydrogels exhibited negligible absorption. The highest absorption was exhibited by the PHA-PEGDA group (2.1). Absorption ratios were reduced by 10 and 5% in the DVC10 and DVC15 groups, respectively ($p < 0.05$).

The swelling ratio of 18 for the PHA group was the highest of all hydrogels tested here (**Supp. 3.1 C**). Each of the remaining hydrogels exhibited 44, 56, 61, and 66% reduced swelling ratios with increasing solid content for the PHA-PEGDA, DVC5, DVC10, and DVC15 groups, respectively. Differences in swelling ratio were significant for each comparison except for the DVC10 group compared to the DVC15 group ($p < 0.05$).
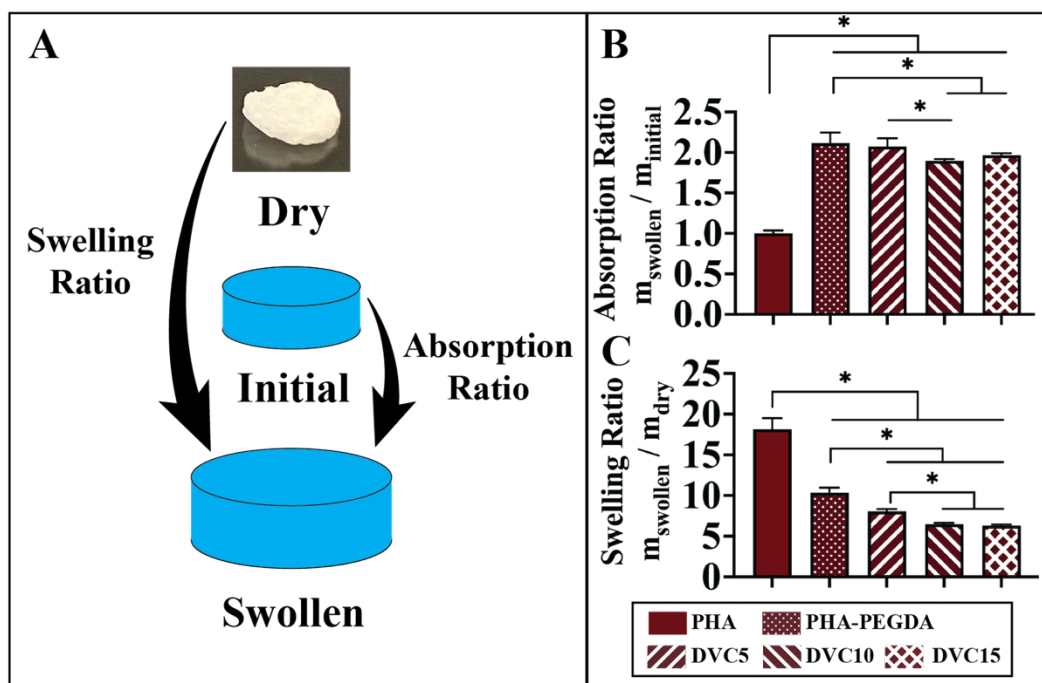
Supplemental Figure 3.1: Hydrogel absorption and swelling.

(A) Illustration of the initial and swollen configurations referenced to the dry mass to calculate absorption and swelling ratios respectively. **(B)** From initial to swollen configurations, water absorption was higher in hydrogels containing polyethylene glycol diacrylate (PEGDA) than pentenoate-modified hyaluronic acid (PHA). **(C)** The mass of fluid absorbed from dry to swollen by PHA was much higher than the other PEDGA-containing hydrogels. Swelling ratios decreased with increasing solid content. PHA was 4% w/v, and PEGDA was 20% w/v. n=6. *$p < 0.05$.

Appendix D: Supplementary Material – Chapter 4

The contents of this appendix were previously published as the supplemental material in the journal Tissue Engineering Part C by Nedrelow, Rassi, Ajeeb, Jones, Huebner, Ritto, Williams, Fung, Gildon, Townsend, and Detamore [32].

Animals. One of the hydrogel group animals was diagnosed at 4 months with caseous lymphadenitis caused by a *Corynebacterium pseudotuberculosis* infection likely contracted before boarding. This subject was removed from the study, leaving three no-hydrogel and two hydrogel group specimens. Two surgeries were performed on the eliminated subject, the first of which was aborted due to caution regarding sterility. Though the infection was contracted outside our facility, it is possible that a stress-activated immune response initiated formation of lymphadenitis.

Anesthesia was performed with topical Lidocaine/epinephrine up to 6mg/kg, and induced with propofol (2-4 mg/kg) and xylazine (0.04-0.06 mg/kg) and maintained under sedation with isoflurane (0.8-3%). Prior to CT scans, animals were sedated with Butorphanol (0.1-0.2 mg/kg), and diazepam (0.1-0.5 mg/kg).

Histological Evaluation. H&E and Alcian blue stained slides were examined by a trained pathologist who confirmed lymphocyte presence associated with CD4 staining.

TMJ disc gross morphological scoring. A gross morphology grading scale was modified[201] to assess TMJ discs after 6 months of implantation **(Supp. Table 4.1)**. The scale's categories ranged from 0 (low grade tissue) to 4 (pristine) as assigned by oral surgery clinicians.

PCL-HAp Degradation and Bone Resorption. Though bone loss bordered the PCL-HAp prosthesis, it was unlikely to have been caused by a degradation product. PCL has a long track record of safe, biocompatible use for *in vivo* implantation.[315], [316] The degradation rate and environment surrounding degraded PCL-HAp is less studied than that of PCL, but evidence from similar materials containing PCL and HAp suggested that PCL-HAp is a highly biocompatible material for implantation.[317], [318] Furthermore, CD4 staining was not consistently associated with bone loss in this pilot study.

Supplemental Table 4.1: Gross Morphology Grading Scale for TMJ Disc Evaluation

Parameter	Grade
(A) Degeneration	
Perforation in disc	0
Friable tissues	1
Thin tissue	2
Reduced area and thickness	3
Normal	4
(B) Hypertrophy	
Large increase in area and thickness	0
Large increase in area	1
Moderate increase in area	2
Slight increase in area	3
Normal size	4
(C) Macroscopic Appearance	
Granulation with highly irregular surface	0
Cratered appearance	1
Furrows in topology	2
Rough	3
Smooth	4
(D) Overall	
	0-4